UNIVERSITY OF CALIFORNIA, SAN DIEGO

High Frequency Dynamics in Magnetic Thin Film Devices

A dissertation submitted in partial satisfaction of the requirements for the degree
Doctor of Philosophy

in

Electrical Engineering (Applied Physics)

by

Richard Choi

Committee in Charge:

Professor Eric Fullerton, Chair
Professor Drew Hall
Professor Vitaliy Lomakin
Professor Shirley Meng
Professor Oleg Shpyrko

2016

The Dissertation of Richard Choi is approved, and it is acceptable in quality and form for publication on microfilm and electronically:

_____

_____

_____

_____

_____

Chair

University of California, San Diego

Epigraph

Lets measure something interesting.

Eric Fullerton

Table of Contents

List of Equations

List of Figures

List of Tables

Acknowledgements

I would like to acknowledge Professor Eric Fullerton for his guidance and mentorship throughout my work as a graduate student at UCSD. Indubitably I would not be where I am today without his guidance.

I would also like to acknowledge the help and support of Dr. Jimmy Kan, without whom my results would be nowhere close to where it is today. It is his support that helped me in ways immeasurable.

Furthermore, it was with the guidance of Professor Vitaliy Lomakin during my undergraduate work that I was introduced into this field of research. And it was not without the support and camaraderie of the entire Fullerton nanomagnetics group that I am able to complete work in my graduate career.

Chapter 2, in part, is a reprint of the material as it appears in IEEE Transactions on Magnetics 2016. R. Choi, J.A. Katine, S. Mangin, E.E. Fullerton. The dissertation author was the primary investigator and author of this paper. I would like to thank the Vitaliy Lomakin computational electromagnetics and micromagnetics group for access to the FastMag micromagnetics simulator. Majd Kuteifan, Marco Lubarda and Iana Volvach for their assistance in running the FastMag software. The research in this chapter was

supported by the Qualcomm Fellow-Mentor-Advisor (FMA) Program and the NSF award DMR #1312750. As well as ANR-NSF Project, ANR-13-IS04-0008-01 "COMAG."

Chapter 3, in part, is a reprint of the material as it appears in IEEE Transactions on Electron Devices, 2016. R. Choi, J.J. Kan, S.H. Kang, E.E. Fullerton. The dissertation author was the primary investigator and author of this paper. This research in this chapter was supported by Qualcomm Fellow-Mentor-Advisor (FMA) Program and the NSF Materials World Network Award #1312750.

Chapter 4 would not be possible without high quality devices supplied by Dr. Ken Lee as part of the Qualcomm Advanced Technology group.

Chapter 5 was in part a collaborative work with Dr. Jimmy Kan. Samples were provided by Dr. Yukiko Takahashi of the National Institute for Materials Science in Japan and by Dr. Jimmy Kan of Qualcomm Inc.

Vita

2008	Bachelor of Science in Electrical Engineering, University of California, San Diego
2009	Master of Engineering in Electrical Engineering, University of California, San Diego
2016	Doctor of Philosophy in Electrical Engineering (Applied Physics), University of California, San Diego

Publications

"Current-induced Pinwheel Oscillations in Perpendicular Magnetic Anisotropy Spin Valve Nanopillars," R. Choi, J.A. Katine, S. Mangin, E.E. Fullerton, IEEE Transactions on Magnetics, Pending

"Demonstration of a Highly-Tunable Hybrid NMOS-Magnetic-Tunnel-Junction Ring Oscillator," R.Choi, J.J. Kan, S.H. Kang, E.E. Fullerton, IEEE Transactions on Electron Devices, vol.63, no.4, pp.1-6, March 2, 2016

"Dual-layer patterned media "ledge" design for ultrahigh density magnetic recording," V. Lomakin, R. Choi, B. Livshitz, S. Li, A. Inomata and H. N. Bertram, Applied Physics Letters 92, 022502, January 14, 2008.

"Fast precessional reversal in perpendicular composite patterned media," B. Livshitz, R. Choi, A. Inomata, H. N. Bertram, and V. Lomakin, Journal of Applied Physics 103, 07C516, March 10, 2008.

Abstract of Dissertation

High Frequency Dynamics in Magnetic Thin Film Devices

By

Richard Choi

Doctor of Philosophy in Electrical Engineering (Applied Physics)

University of California, San Diego, 2016

Professor Eric Fullerton, Chair

In the field of magnetics, there are many devices that exhibit either behavior in the microwave regime or response to stimuli from microwave sources. The ultimate goal of this work is to study these devices and characterize and optimize their behaviors. In support of this goal, a myriad tasks are required including and not limited to device

fabrication, test fixture fabrication and machining, characterization and testing software programming, automated data processing, and comparison to modeling. Specialized RF equipment will be utilized to measure high-frequency signals including high-frequency fixtures, probes, RF cables, vector network analyzers, and spectrum analyzers. The results of these characterization measurements include the finding of high-frequency oscillation modes in perpendicular spin valve nanopillars, the discovery of a magnetically-tunable ring oscillators, characterization of spin torque nano oscillators based on in-plane magnetic tunnel junction devices, a study of a cross-coupled spin torque nano oscillator, and device characterization using temperature-dependent ferromagnetic resonance.

Chapter 1: Introduction to Spin Transfer in Thin Films

1.1 A Brief History

The discovery of spin-transfer torques emerged from the discovery of giant magnetoresistance (GMR) in 1988 by Fert [1] and independently by Grünberg [2] had ushered in a new renaissance in the field of solid state physics and magnetic recording, a technology with such a profound impact, it was awarded with the 2007 Nobel Prize in physics. The discovery of this technology enabled a compound growth rate of approximately 100% in areal recording density using GMR heads in hard drives, much higher than the previous 60% CGR with MR heads [3]. A progression of technology starting from GMR is also relevant for a growth in areal density using tunneling magnetoresistance (TMR) heads [4, 5]. As a technology, TMR also shows promise as a new class of memory recording devices known also as spin-transfer-torque magnetic random access memory (STT-MRAM)[6] and more generally a wide range of spintronic devices[5].

The use of giant magnetoresistance (GMR), tunneling magnetoresistance (TMR) and related spin-torque switching devices and their ability to exploit electrical control over magnetization dynamics has sparked extensive development for applications in

data recording, magnetic memory and spin torque nano-oscillators [7-10].

1.2 Spin Transfer Torque

In the work presented in this dissertation, the spin torque effect originally predicted in 1996 by Slonczewski [11] will play a prominent role in the class of devices and behaviors in magnetic thin films, mostly on the 100-nm scale or below. A simplified diagram of the classic model of a spin-torque device is presented as two thin magnetic layers separated by a non magnetic layer (Figure 1.1). The first magnetic layer has a fixed magnetic orientation and current flows through the device. When current flows through the device, the current becomes spin polarized by transmission through or upon reflection from the first magnetic layer (the reference layer) and mostly maintains this polarization as it passes through the non-magnetic spacer and enters and interacts with the second ferromagnetic layer.

If the orientation of the second layer (free layer) and reference layer are not co-linear, the spin-polarized current imparts a torque onto the magnetization of the free layer while the spin polarized current also move towards the direction of the magnetization of the free layer through conservation of angular momentum. In the reverse scenario where both layers are co-linear and the electrical configuration of

current is in the reverse direction, the spin-polarized current can also perturb the magnetization of the free layer from the reflected current at the interface between the non-magnetic layer and the reference layer.

This spin torque can oppose the intrinsic damping of the magnetic layer exciting spin waves and, for sufficient current strengths, reverse the direction of the magnetization. The spin-torque interaction between the reference layer and the free layer can lead to deterministic switching or high-frequency oscillations of the free layer.

There are additional dynamics involved and presented in this dissertation, but this is the basic model of spin transfer torque devices. This interaction also leads to a change of resistance depending on the relative orientation of the magnetic layers giving rise to GMR for metallic spacers or TMR for insulating spacers.

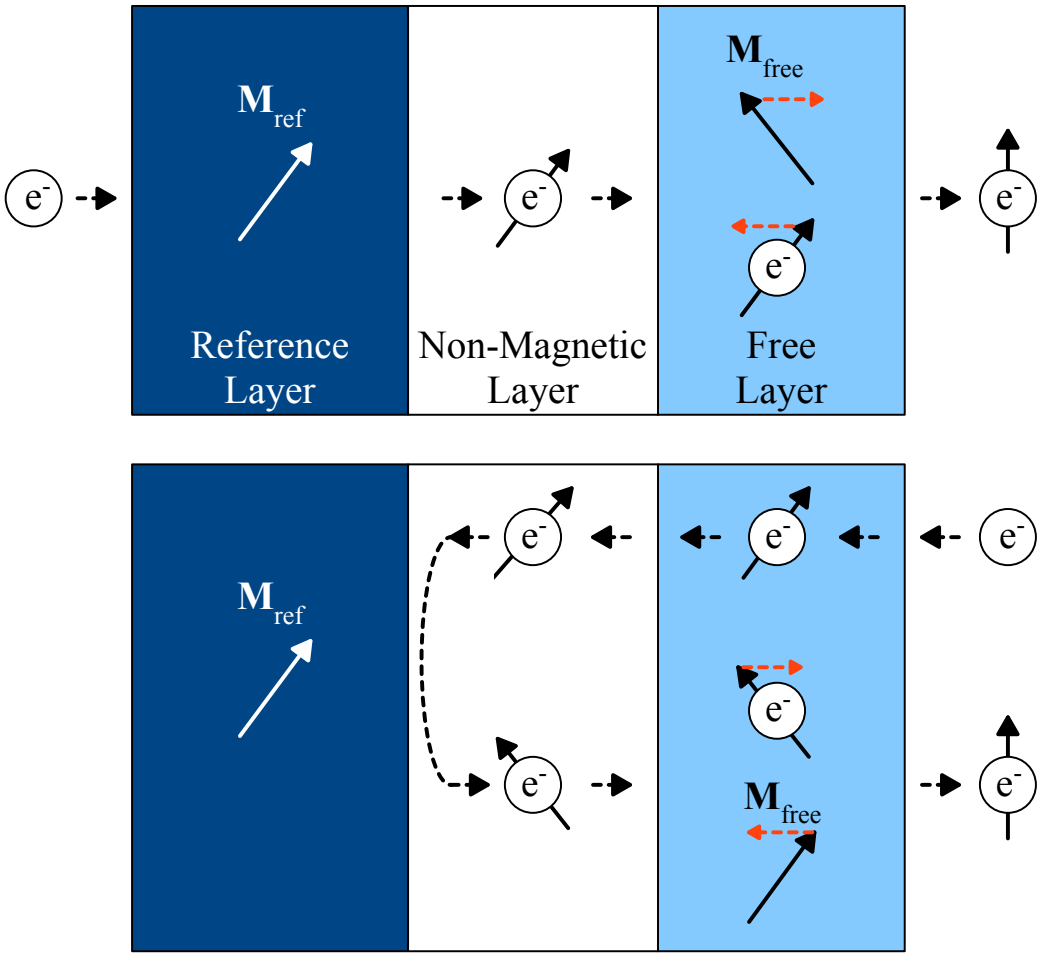

Figure 1.1 Diagram showing the basic layout of a spin-torque device. In first diagram (top) the reference layer polarizes the spins of current which passes through the spacer layer to the free layer, the spin is absorbed and torque is imparted in the free layer in a process known as spin-transfer torque. In the second diagram (bottom), the current is in reverse orientation.

Both GMR and TMR takes advantage of spin-transfer torque to create a magnetization switching behavior completely dominated by electrical sources with no external magnetic sources, the specific mechanisms and examples are further

investigated in Chapters 2 and 4.

Two equilibrium magnetic states are defined for most spin-torque switching devices. In the example of an in-plane magnetization device, the states are represented by the parallel (P state) and anti-parallel state (AP state) as shown in Figure 1.2 (a). As a quick note, it's typical for magnetic films to have a preferred magnetic orientation in the in-plane or perpendicular to plane directions [12]. Often times the use of shape anisotropy [13] is used for in-plane media or devices to induced a preferred direction.

Similarly for devices with perpendicular magnetic anisotropy, the same P/AP convention is used (Figure 1.2 (b)). The absolute orientation of either layer are generally irrelevant to defining the P state and AP state for either the in-plane or perpendicular magnetic anisotropy. It's the relative orientation of the magnetization of the free layer to the magnetization of the reference layer which defines the states, and therefore the corresponding high and low electrical resistances of the device.

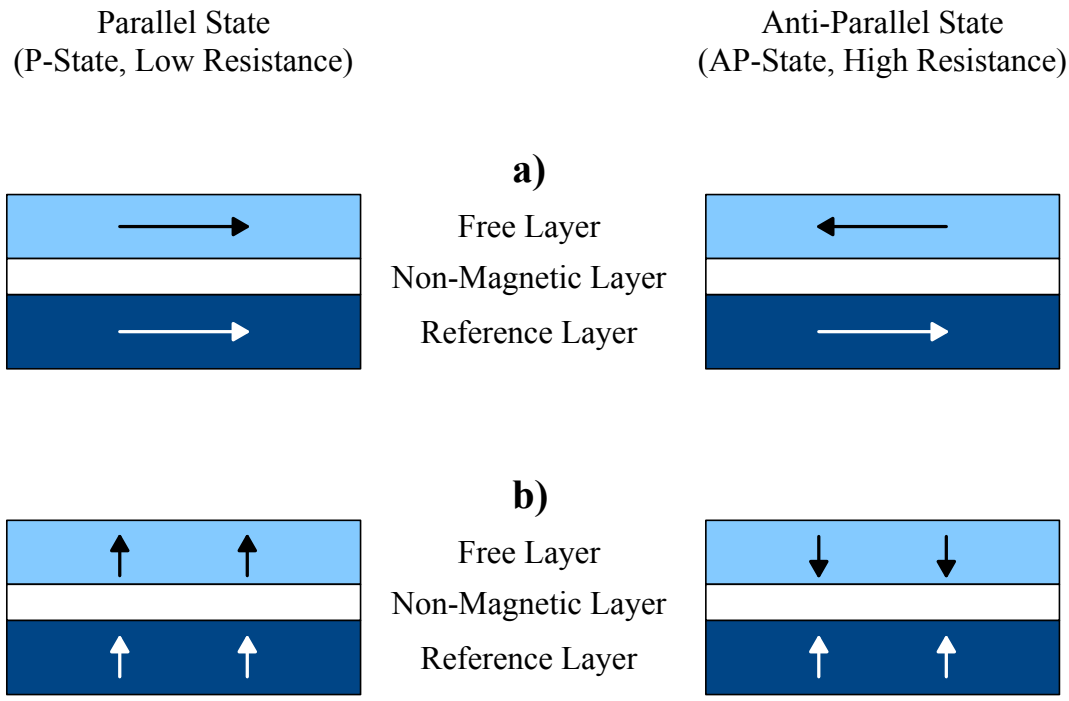

Figure 1.2 (a) Shows the convention for the P and AP states in in-plane magnetic anisotropy devices. (b) Shows the convention for P and AP states in perpendicular magnetic anisotropy devices.

Due to the magnetoresistive effect, GMR and TMR, the relative orientations of magnetization creates a resistive effect for the stack. In the P state, the device is electrically in a lower resistance relative to the AP state, which is in turn, at a high relative resistance to the P state. The spin-torque device state can be switched using field, and is designed to be stable in both states at low fields.

The devices investigated will include spin valves, any multi-layer magnetic device which has an electrical resistance that changes with the relative orientation of

magnetization of its respective layers, and magnetic tunnel junctions (MTJs) which are a class of TMR spintronic devices where the resistance of a nano-scale pillar may be tuned by magnetic fields or injected spin-polarized currents.

MTJs are the memory elements in non-volatile magnetic random access memory (MRAM), but also show promise for RF applications when configured as high-frequency oscillators [14] and are the active components in read heads for magnetic hard disk drives. An MTJ is a resistive, spintronic device which can be designed to have two discrete resistance states that can be switched by either magnetic field or electrical current. The resistance of the device is correlated to the relative orientation of the magnetization between two ferromagnetic electrodes (called reference and free layers) [15]. The parallel orientation (P state) has a low resistance, while the anti-parallel orientation (AP state) has a high resistance [16], characterized by the magnitude of the previously mentioned TMR, defined as

$$GMR\ ,TMR\ = \frac{R_{AP} - R_P}{R_P}$$

Equation 1.1

Where R_{AP} is the resistance in the AP state and R_P is the resistance in the P state. In Equation 1.1, TMR is interchangeable with GMR as both are measured identically.

1.3 Switching Conditions

The field switching behavior is similar to many other magnetic thin film device as shown for a TMR device with in-plane anisotropy switching it's free layer using field while measuring the resistance of the device in Figure 1.3. There is a strong jump in resistance at the coercive fields, shown here to be approximately 250 Oe.

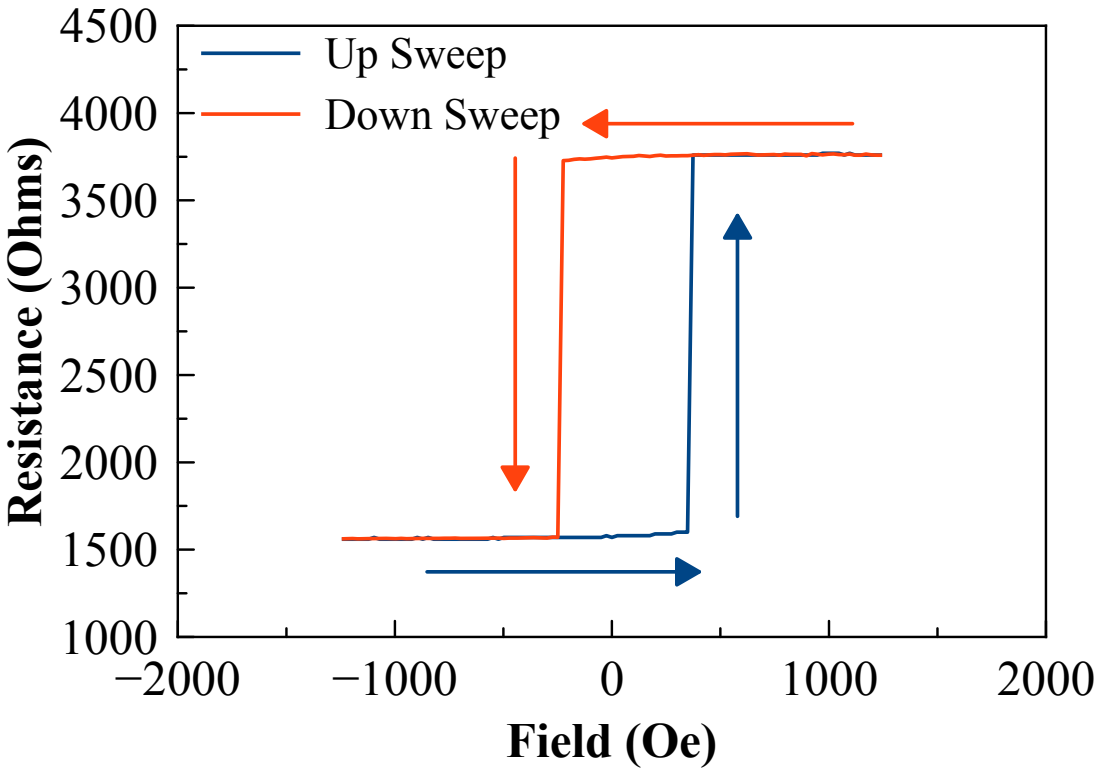

Figure 1.3 Hysteretic switching using field of a spin torque device. A small current (<10uA) is used to measure the electrical resistance of the device as the field is swept.

In addition to field switching, the device also exhibits hysteretic switching using

current - by changing the sign of current, the device can be switched to either state deterministically. Again, the free layer switching is shown in Figure 1.4, however this time using spin-torque, the electrical resistance is measured using the same current used to switch the device. The plot clearly shows the hysteretic behavior, in addition we can see a clear jump in resistance as the device changes from P to AP state and vice-versa.

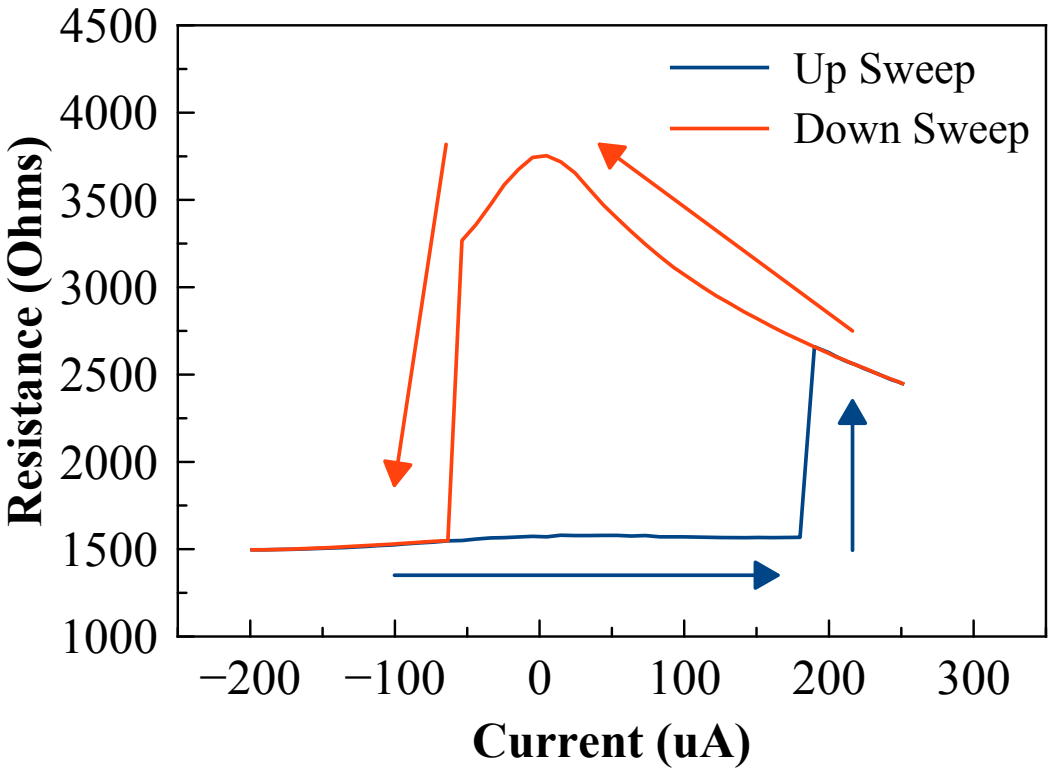

Figure 1.4 Hysteretic switching of a spin torque device using current. The device resistance is measuring using the same current used to switch the device. Switching in both directions using current is made possible due to the properties of spin transfer

torque.

The switching behavior, critical switching current and switching dynamics are explained in further details section 2.6 and section 4.2, but to provide an introduction to the switching mechanics, we can examine the Landau Lifshitz Gilbert (LLG) equation from with the Slonczewski term for spin torque,

$$\frac{dm}{dt} = \gamma_0 H \times m + \alpha\left(m \times \frac{dm}{dt}\right) + \frac{IP_i g \mu_B}{eM_S t}\left(m \times \left(m \times p\right)\right)$$

Equation 1.2

Where γ is the gyromagnetic ratio, m is the magnetization, H is the effective field, α is the damping parameter, I is the current density, P_i is Slonczewski's expression and is represented as a scalar function, g is the g-factor, μ_B is the Bohr magneton, e is the elementary charge, Ms is the saturation magnetization, t is the thickness of the free layer, and p is the unit vector of magnetization for the reference layer.

We see three main terms in Equation 1.2, the first describes the precessional torque, the second describes the damping torque and the third term represents spin torque, the various terms are illustrated in Figure 1.4.

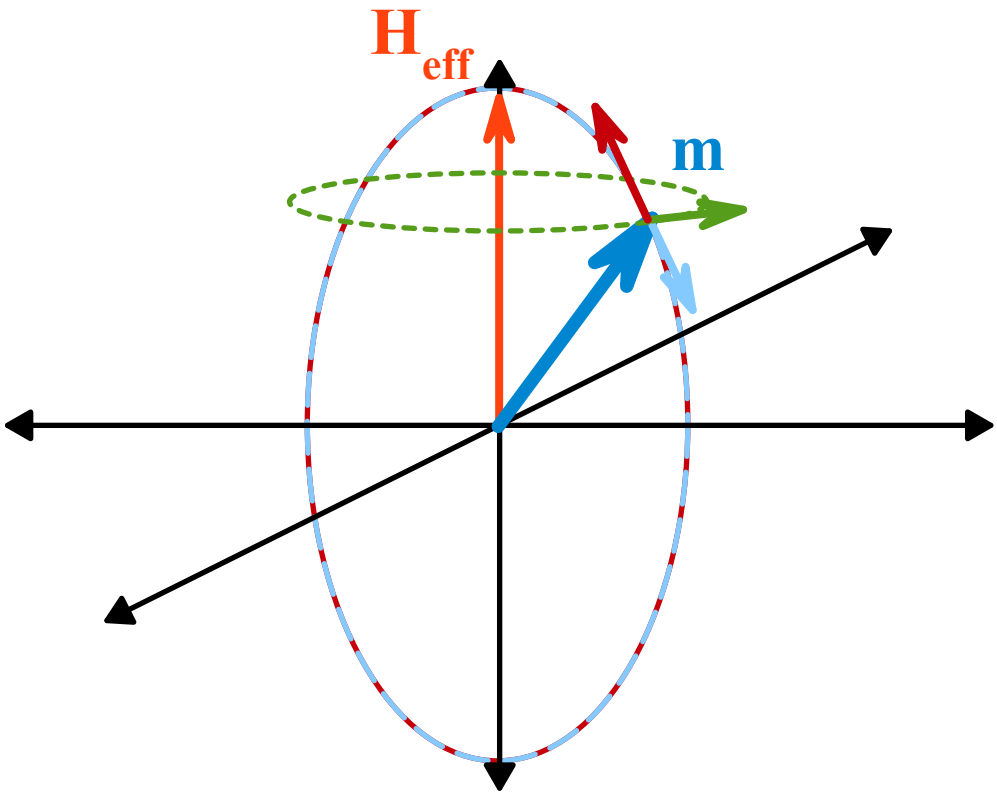

Figure 1.5 A diagram showing the various forces on magnetization as described by the Landau Lifshitz Gilbert Slonczewski equation. The green vector shows indicates the precessional or field torque component, the dark red vector indicates the damping torque and the light blue vector indicates the spin torque component from corresponding spin polarized current.

The general condition for switching to occur requires the spin torque term to counter the damping term, the critical current for switching at zero temperature assuming the P state is described as

$$I_{C0} \approx \frac{\alpha M_S V}{g(\theta) p}\left(H_{Keff} - H\right)$$

Equation 1.3

where α is the damping, M_s is the saturation magnetization, V the volume of the magnetic elements, $g(\theta)$ is expression for the angular variation in spin torque, p is the spin polarization of current and ($H_{Keff} - H$) is the effective magnetic field acting on the magnetic layer where H_{Keff} is the effective anisotropy field (including the demagnetization fields) of either the free and fixed layers and H is the external magnetic field that includes the dipolar fields originating from the adjacent magnetic layer.

These spin torque devices are hysteretic and switchable using both field and current, without any input they remain in either the P or AP state which electrically represent different resistance states that can be measured simply by using a small amount of current (below the switching current for the device). This behavior is well suited to memory applications [17], however we can also exploit the spin torque dynamics to create pinwheel oscillators [18], spin torque oscillators [19], magnetically tunable ring oscillators [20], field detection [21], and RF detection sensors [22], many of which will be presented in this dissertation.

Chapter 2: Pinwheel Oscillations in PMA Spin Valve Nanopillars

2.1 Introduction

Nanopillar spin valve devices are typically comprised of two thin ferromagnetic layers: a reference layer and a free layer whose magnetic orientation can be changed by both an external magnetic field and through the introduction of spin-polarized electric current. The reason a thin film nanopillar device was chosen is that there is a decay in spin polarization [23] past the ferromagnetic interface and the thinner cross-sectional area of a nanopillar allows for a higher current density. Here we report the continuous repeated switching behavior of both the reference and free layers of a perpendicular spin valve made of Co/Pd and Co/Ni multilayers that arises for sufficiently large DC currents. This periodic switching of the two layers produces an oscillating signal in the MHz regime but is only observed for one sign of the applied current. The observed behavior agrees well with micromagnetic simulations.

2.2 Reversal Dynamics

In most devices such as STT-MRAM [14] the reference layer is designed to be stable in response to spin-torque interactions so that the switching behavior of the

device depends solely on the action on the free layer. However, for sufficiently high currents the interactions with the free layer can destabilize the reference layer [24]. More generally one expects that the mutual interaction between the layers should cause the two layer to rotate in the same direction in a pinwheel-like motion as originally predicted in [11] and discussed for layers with in-plane magnetic anisotropy [25]. A similar behavior may be expected for spin valve devices with perpendicular magnetic anisotropy (PMA) [26] as shown schematically in Figure 2.1 where we consider for simplicity each magnetic layer as a macrospin. Assuming that you start with a parallel alignment as shown in Figure 2.1 (a) and positive DC currents (negative electron flow) the spin torque interactions will stabilize the reference layer and destabilize the free layer (as a result of the back flow of down spin electrons reflected from the reference layer) causing the free layer to switch to the configuration shown in Figure 2.1 (b). This is the standard operation of a memory cell where current is used to set the direction of the free layer. In this configuration the spin-torque interaction now stabilizes the free layer but will tend to destabilize the reference layer which, for sufficiently high currents, should then switch to Figure 2.1 (c). In memory cell applications the operational current is below that needed to perturb the reference layer or the reference layer is stabilized by an exchange bias layer [17]. In the configuration of Figure 2.1 (c) the spin-torque interaction will again destabilize the free layer causing

it to switch to the configuration in Figure 2.1 (d). Finally the spin-torque interaction will cause the reference layer to again switch to Figure 2.1 (e) which is the starting configuration Figure 2.1 (a) and the process is expected to repeat.

As the layers reverse the system oscillates between the parallel and antiparallel configurations causing a periodic change in the resistance. This behavior should be, in principle, independent of the current flow direction. In the present study we observe, for the first time, the pinwheel motion in magnetic spin valves with PMA as shown schematically in Figure 2.1 [9], [10] where the resistance oscillates in a periodic fashion. For typical spin torque nano oscillators the oscillations result from precessional motion of the magnetic layer giving oscillation frequencies in the GHz range [27]. However, pinwheel motion requires periodic reversal of the direction of the magnetic layers which is typically on the nanosecond or longer time scales [28]. Thus the expected oscillation frequencies are in the MHz range.

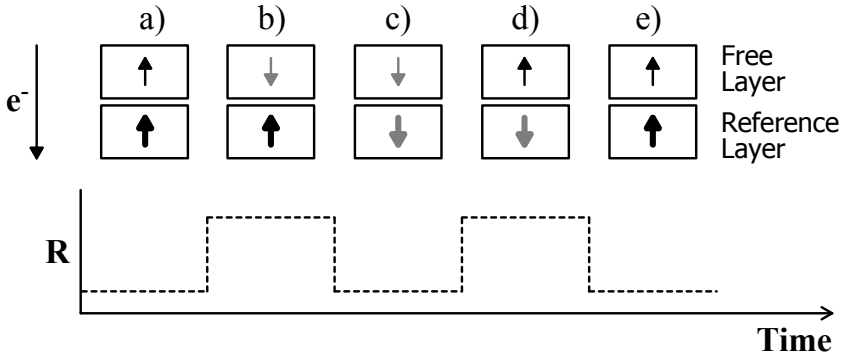

Figure 2.1 (a)-(e) Schematic of expected magnetic configuration and device resistance versus time for large positive DC current (negative electron flow as shown in Figure). The top layer is the lower anisotropy free layer and the bottom layer is the higher anisotropy reference layer, the arrows represent macrospin orientations.

2.3 Nanopillar

The experimentally studied devices are identical in structure to those in Ref. [24], [Co(0.3nm)/Pd(0.7nm)]x2, [Co(0.15nm)/Ni(0.6nm)]x2, Co(0.3nm), Cu(4nm), [Co(0.15nm)/Ni(0.6nm)]x2, [Co(0.3nm)/Pd(0.7nm)]. Both reference and free layers have PMA due to the Co-Ni and Co-Pd multilayer structure [12]. The reference layer has higher anisotropy and is magnetically harder due to the additional repeats of the Co-Pd multilayer. The films were grown by dc magnetron sputtering onto Si(100) wafers coated with a 200-nm thermal oxide. The nanopillars were patterned by e-beam lithography into various geometries, as shown as a piece of a cut wafer seen in Figure 2.2. In this study we focused on 120-nm diameter circular nanopillars.

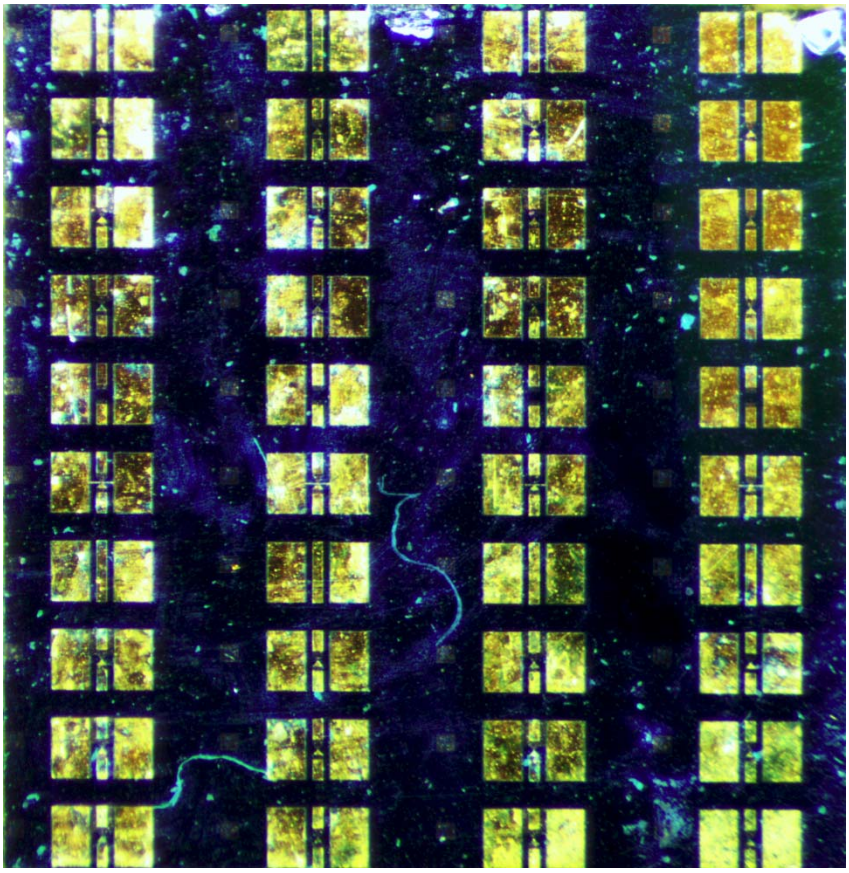

Figure 2.2 A photo of an array of devices on a single piece of cut wafer. The two large pads are connected to the ground plane. On some devices the ground plane is floating, while other devices have the ground plane connected to the bottom lead. The triangular feature points towards the bottom lead.

2.4 Switching Conditions

The switching conditions for both the free layer and the reference layer in these devices were characterized to understand the coercive fields and the critical switching currents to cause reversal in these layers. Primarily, field and current applied to the

device needs to be such that in all states mentioned in Figure 2.1 are attainable and without changing either field or current, reversal conditions are met.

In addition to the free layer, we determined the minimum current to perturb the reference layer direction by using the approached outlined in Ref. [24] where both layers are set to the P state, we apply a large current for 1 s and then measure the response of the nanopillar at low fields to see if there was a change in the reference layer. From these measurements the *I-H* switching boundaries of the reference layers for the nanopillar can be determined. Comparing these results to previous measurements allow us to understand that the critical current for free layer switching is much lower than for the reference layer [26].

The efficiency of spin transfer torque concerning the ratio of the energy barrier to the critical current is asymmetrical [29] with respect to the orientation of current in metallic systems. Due to this change in efficiency with respect to direction of current, one current direction has greater efficiency in switching the reference layer as shown in Figure 2.3. For electrons flowing from the free layer to the reference layer we see a higher efficiency (as reflected in the increased slope in of *I-H* boundary) in reference layer switching than for electrons flowing in the opposite direction. In contrast to the conventional operation of a spin valve, current from the free layer is switching the

reference layer state, this is an essential condition for oscillation to occur in these devices.

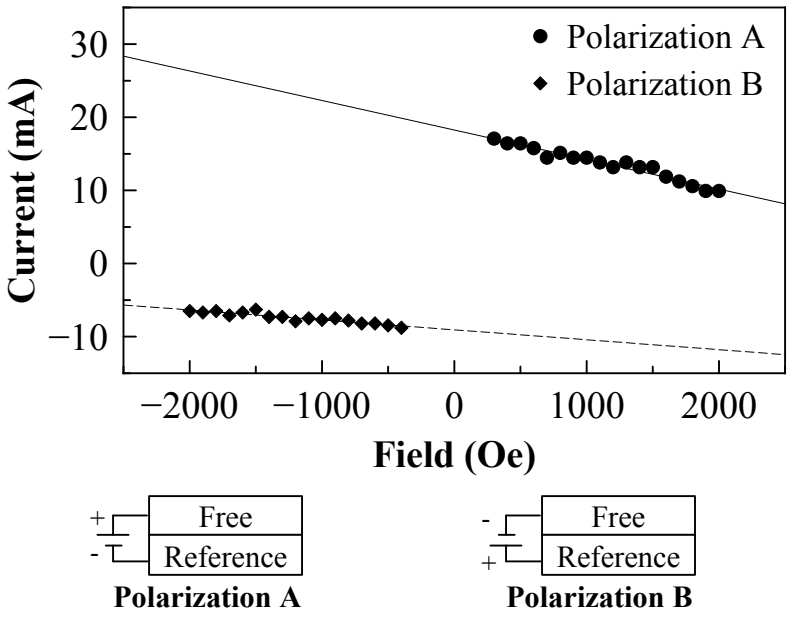

Figure 2.3 The switching boundary and switching efficiency of the reference layer with respect to the direction of current. Polarization A represents the current direction where the free layer is positively biased, polarization B represents the current direction where the reference layer is positively biased.

Knowing the switching state diagram of the free layer, coupled with the room temperature switching current of the reference layer gives us a cursory idea of the switching conditions necessary to achieve oscillation, namely depending on the electrical polarization, we will mainly need a sufficient amount of current to drive these devices into a regime of oscillation.

2.5 Measurements

The electrical characterization was carried out using an AC lock-in amplifier with the current flowing perpendicular to the plane. All devices were wire bonded with a gold wire ball bonder. We also applied an external magnetic field normal to the layers. In a 4-wire measurement, these devices exhibited a GMR ratio ranging from 0.5%-1.1%. The coercive fields were ~250 Oe and ~3000 Oe for the free and reference layers, respectively as shown in Figure 2.4 (a) and the effective dipolar field acting on the free layer from the reference layer is 180 Oe as reflected in the shift of the minor loop in Figure 2.4 (b).

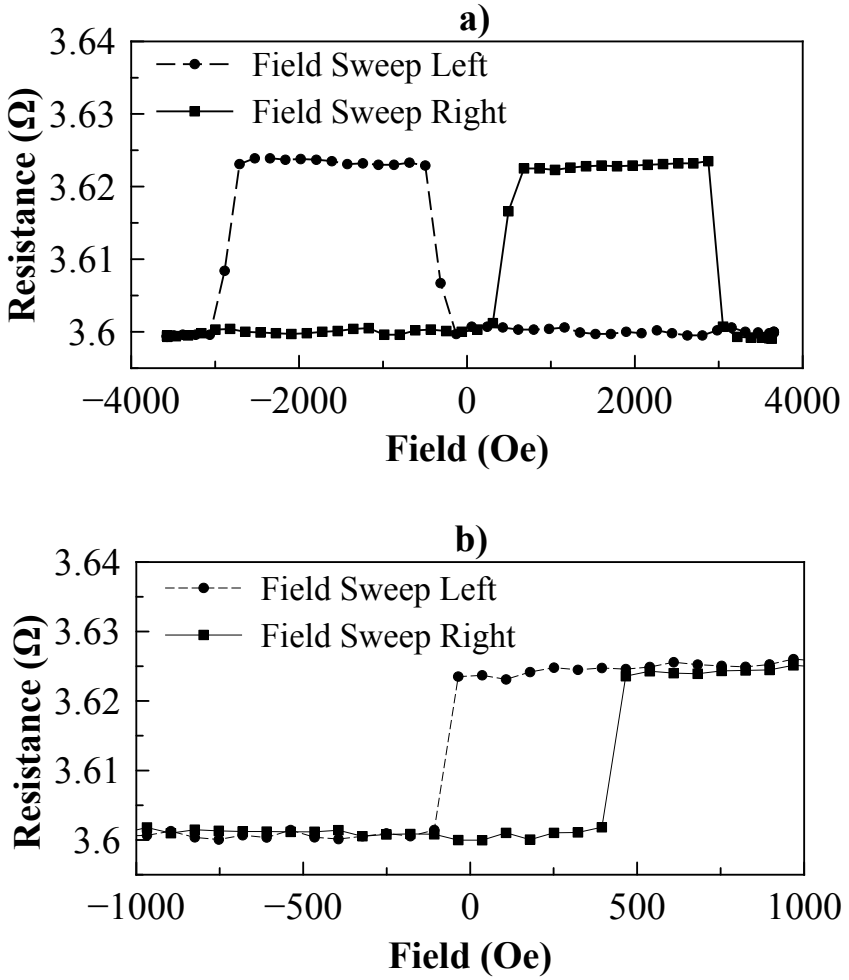

Figure 2.4 (a) The field-dependent switching characteristics of the 120-nm circular nanopillars. The reference layer exhibits a coercive field of 3000 Oe, while the free layer (b) exhibits a coercive field of 250 Oe with an effective dipolar field of 180 Oe and GMR of approximately 0.62%.

High frequency measurements were performed by applying a DC current of 10-30 mA corresponding to a current density on the order of 1x10^8 A/cm^2 and a magnetic field perpendicular to the plane of the sample. The device was contacted using ground-signal RF probes. While the current remains constant, the rapidly

changing magnetic state produces a high-frequency output which we record using a spectrum analyzer through a bias-tee.

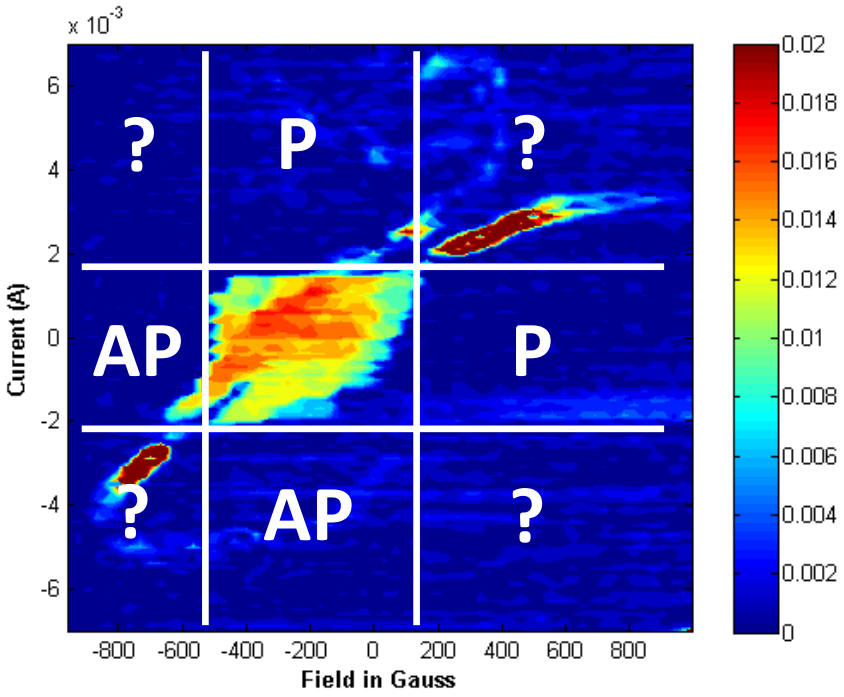

Figure 2.5 Switching state diagram for the free layer in these nanopillars. The regions in red indicate a bistable region, depending on the conditions the device can be stable in either a P or AP state. The regions in blue indicate a single state stable region (either P or AP). For this particular device configuration, the device is in the P state in the blue region to the right and above the red block and in the AP state in the region to the left and below the red block. The stable regions are applicable to the range shown. The scale is in $\Delta\Omega$.

Running a device characterization but over both a range of field and current, we assemble the characterization data into a switching state diagram (SSD) in Figure 2.5. These SSD are assembled by subtracting the difference between the hysteresis loops

like those pictured in Figure 2.4. By examining a vertical slice, one would quickly be able to ascertain the critical switching currents at a specific magnetic field in these particular plots. By examining a horizontal slice, one would also be able to ascertain the coercive fields for a particular current level.

The bright central region is a bistable region where the exact state (P or AP) is unknown given just current and field. The blue regions directly adjacent to the bistable region represents a stable state, either P or AP and is marked as such. However regions in the corner represent a grey area where the state cannot be absolutely known, especially for higher magnitudes of field and current. It is in these regions that we can expect pinwheel switching to occur.

2.6 Results

The oscillation can only occur when the current is above the threshold value necessary to switch the reference layer (Figure 2.3). High frequency activity can be observed for applied current up to the Joule heating limit of the nanopillar device. The characteristics and behaviors are similar among devices of identical geometry and show a demonstrable and repeatable tunability in peak frequency with respect to current (Figure 2.6) where the characteristic frequency shifts to higher frequency with

increasing current. While the peaks shift linearly, there is a widening of the bandwidth at higher currents due to less uniformity in the reversal behavior (as described below in the modeling).

These devices have peak oscillating behavior when powered with approximately 18 mA, the most coherent oscillation occurs at this current levels. There is the previously mentioned loss in oscillation uniformity at both higher current levels and at the lower 16 mA level. Simulation tends to agree with the trend at current over 18 mA, however in the device we see an unexpected loss in power (approximately 1.4 dB or 70% of the output power) for 16 mA compared to 18 mA. While the expected peak power of 16mA compared to 18mA is approximately 80%, the 16 mA power density has a slightly wider bandwidth than the 18 mA power density, so it has less overall peak power than expected.

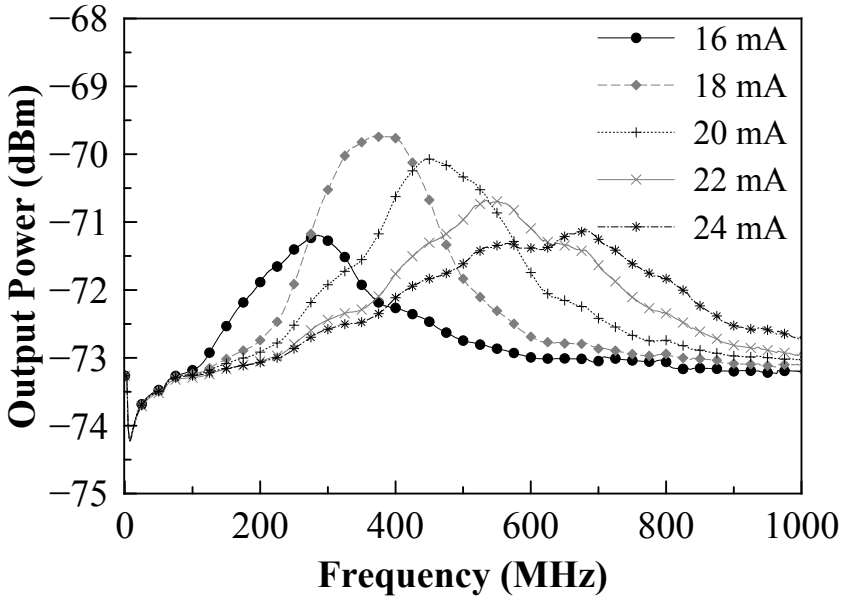

Figure 2.6 Measured frequency output from oscillating nanopillar devices with a 1111 Oe bias field. Only DC current sources were used.

Unlike with current, the switching frequency of the nanopillar is not strongly affected by the magnitude of the applied magnetic field as shown in Figure 2.7. Because each magnetic layer switches both direction as seen in Figure 2.1 the applied field will speed up the switching into the field direction and slow the switching in the direction opposing the applied field yielding a frequency that is relatively insensitive to the applied field. The magnitude of the signal, however, increases with increasing magnetic field. As will be detailed in the modeling below the presence of a magnetic field increases the magnitude of the output signal by stabilizing the free layer in the field direction to increase the disparity in magnetization with respect to the reference

layer, thereby increasing the change in resistance.

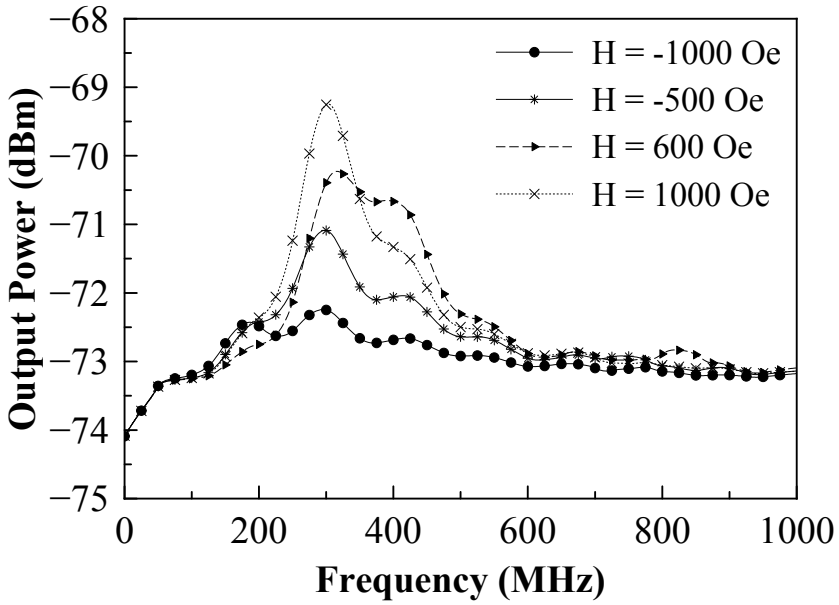

Figure 2.7 Changing the field does little to alter the frequency at which oscillations occur, however higher field intensity can effectively help pin the free layer so larger GMR signals are produced, resulting in higher output power. A 17 mA DC current was applied to the device.

Unlike in simple model in Figure 2.1 the oscillation behavior depends strongly on the direction of the applied current. We only observe oscillations when current polarized by the free layer flows towards the reference layer, polarization B as shown in Figure 2.3. This may be expected as the reference layer is the harder layer to switch and the spin-torque efficiency for switching the reference layer is highest for polarization B (Figure 2.3). The oscillations are limited by the switching of the harder layers. There is a higher spin-torque efficiency for hard layer reversal for one sign of applied current

than the other. While modeling has suggested that if we continue to increase current for the non-oscillating polarity, we can eventually achieve oscillation. We further see evidence of domain states in simulations for lower efficient current directions that may limit our observations. We will further discuss that stable domains states are also observed in modeling that suppress the oscillatory behavior for one current direction.

We can estimate the expected oscillatory frequency from Refs. [30] and [31] where we know that the switching time τ of the magnetic layers follow the form

$$\frac{1}{\tau} = A\left(I - I_{c0}\right)$$

Equation 2.1

where A is the dynamic parameter which governs the switching rate, I is current and I_{c0} is the zero temperature critical current. Equation 2.1 has been shown experimentally to describe the reversal of spin-torque devices with PMA layers [31]. The value of I_{c0} can be estimated for both the free and reference layers

$$I_{C0} \approx \frac{\alpha M_S V}{g(\theta)\, p}\left(H_{Keff} - H\right)$$

Equation 2.2

where α is the damping, M_s is the saturation magnetization, V the volume of the magnetic elements, $g(\theta)$ is expression for the angular variation in spin torque, p is the

spin polarization of current and (H_{Keff} – H) is the effective magnetic field acting magnetic layer where H_{Keff} is the effective anisotropy field (including the demagnetization fields) of either the free and fixed layers and H is the external magnetic field that includes the dipolar fields originating from the adjacent magnetic layer.

The critical current for switching of both the reference and free layers in Figure 2.3 follows a linear I vs. H behavior as expected from Equation 2.2 and has been seen before [26]. Extrapolating the measured results in Figure 2.8 (b) to zero frequency give an estimated measure for I_{c0} = 9.8 mA which agrees with the measured critical current results in Figure 2.3 for the reference layers. However, because the measurements are at room temperature, the results in Figure 2.3 slightly underestimate I_{c0} because thermal energy will assist switching resulting in a measured critical current lower than predicted by Equation 2.2 for longer times [28].

Since I_{c0} for the reference layer is much larger than the free layer, the switching dynamics of the reference layer have a greater influence on the speed at which the system oscillates. With the frequency inversely proportional to the time constant τ, Equation 2.1 predicts the linear relationship between current and frequency we see in measurements.

While the applied bias field may affect signal intensity and noise, the effect does not significantly change the fundamental speed at which the device switches as shown in Figure 2.7. Notably, I_{c0} in Equation 2.2 changes as the applied field changes, causing τ to change, while we may initially expect this to significantly impact the frequency of oscillation, we have in fact four switching events, the P-AP and AP-P switching for both reference and free layer $\tau_{f\_p\text{-}ap}$, $\tau_{f\_ap\text{-}p}$, $\tau_{rp\text{-}ap}$, $\tau_{r\_ap\text{-}p}$. For varying low values of field, as the P-AP switching time increases, the AP-P time decreases and vice versa resulting in very little change in the fundamental oscillating frequency when $H \ll H_{K\text{eff}}$.

2.7 Simulation Data

To further understand the pinwheel oscillations we have performed detailed micromagnetic simulations using parameters derived from characterization of these films. A 120-nm circular disc nanopillar was simulated with the FastMag simulation software [32] as well as the LLG micromagnetic simulator using the parameters presented in Table 2.1. A 1000-Oe field is applied along the direction perpendicular to the film plane. The AC response is presented in Figure 2.8 (a) and the transient response in Figure 2.9 (a)-(b).

Table 2.1 Nanopillar Simulation Parameters

	Reference Layer	Free Layer
K_s (erg/cm^3)	3.0e6	2.1e6
M_s (emu/cm^3)	600	600
Aex (erg/cm)	1.05e-6	1.05e-6
α	0.03	0.03
Polarization	0.35	0.35
Magnetoresistance	0.01	0.01

A list of simulation parameters used for the FastMag micromagnetic simulation software. It's important to note that while most of these parameters are derived from characterization, there is some estimation (eg. polarization, α), some rounding and there is always device-to-device variation.

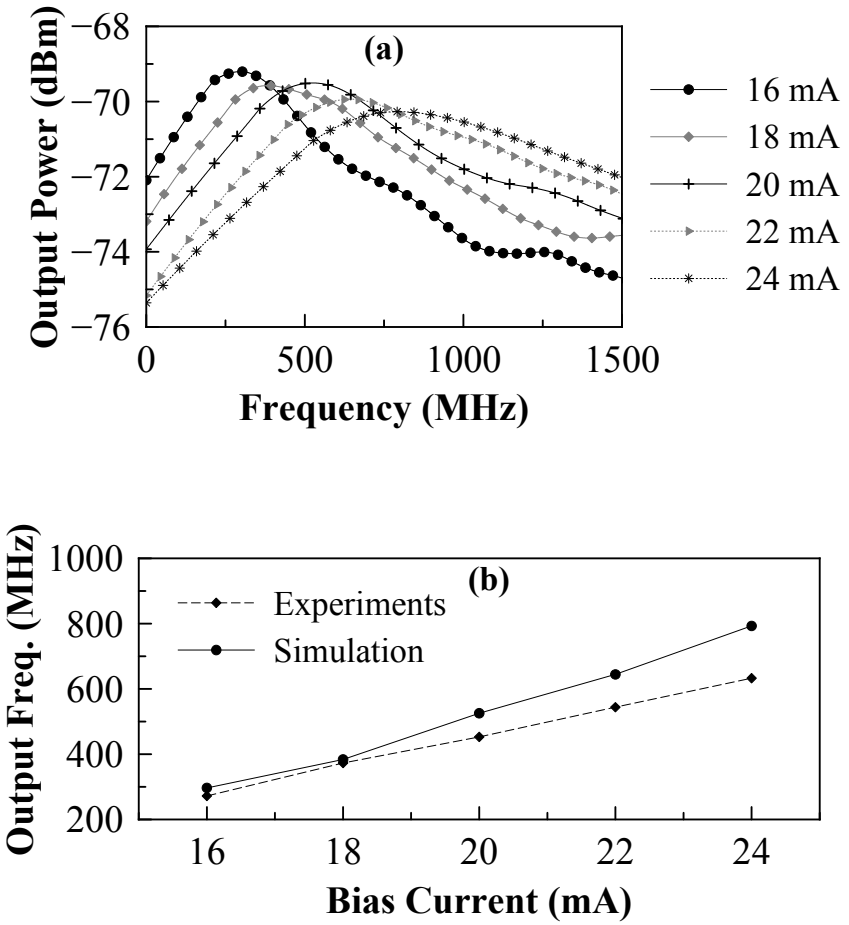

Figure 2.8 (a) The simulated output spectrum for a 120nm nanopillar disc with 1000 Oe bias field and variable DC current. (b) The output frequency of the nanopillar versus input bias current, the behavior from the model closely resembles the characteristics of physical nanopillar.

Simulation results show behavior that closely matches the response of the measured devices as shown in Figure 2.8 (b). We speculate that the slight deviation between the experimental and simulated oscillation frequencies are likely from deviations between input parameters and actual device characteristics. Additionally, these are zero temperature simulations where Joule heating is also not calculated. The

transient analysis in Figure 2.9 (a)-(d) portrays the output characteristics from the interactive switching behavior between the free and reference layer. The switching behavior is characterized by inhomogeneous magnetic configurations in each of the layers. This inhomogeneous switching in PMA devices has been well established from the presence of domain state in the free layer [33, 34] and direct imaging of the nonuniform reversal by time-resolved x-ray microscopy [35]. Domain states have also been observed in reversal of the reference layers by spin-torque switching [24]. We similarly observe non-universal reversal of both the free and reference layers in our simulations.

In the model the layers begins to switch when the opposite layer reaches a sufficient magnetization in the opposite orientation. Because of this we never observe the full uniform states shown schematically in Figure 2.1. Both layers are able to begin switching before either layer is fully saturated, resulting in only a percentage of the device magnetoresistance contributing to the RF signal, Figure 2.9 (b),(c). In Figure 2.10 we show snapshots of specific magnetic configurations. The application of an external applied field helps to achieve a uniform state, particularly in the free layer, increasing the output voltage. This non-uniform response results in the broad frequency response at a given current and relatively low Q. Thus the schematic shown in Figure 2.1 is an oversimplification.

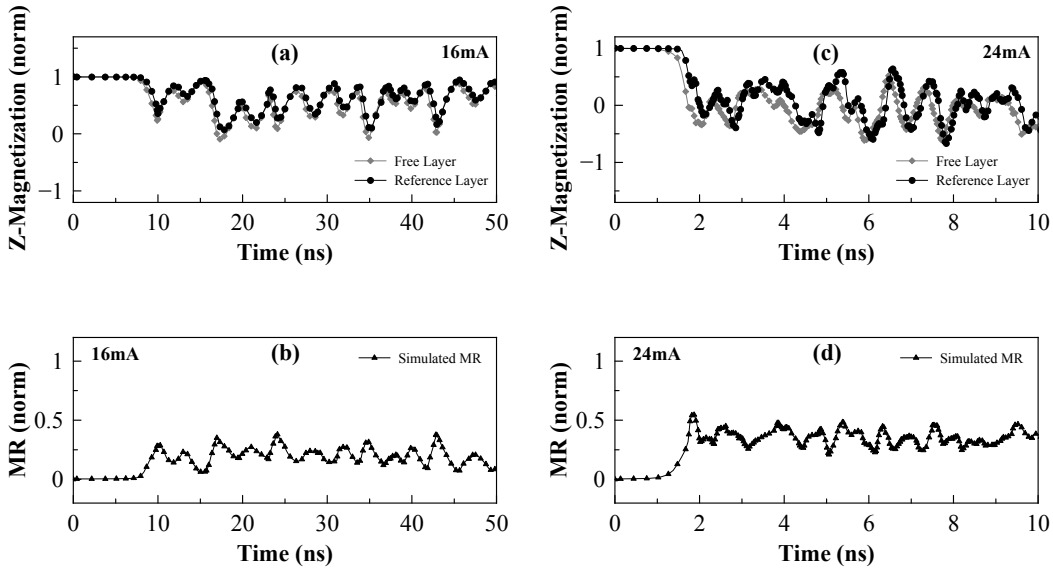

Figure 2.9 The simulated behavior of the layers during oscillation with 16mA and 24 mA. (a) The transient response of both reference and free layers with 16 mA current. Oscillation frequency is more heavily determined by the switching characteristics of the reference layer, as the lower coercivity free layer mainly follows the reference layer as it switches. (b) The normalized spin resistance of the nanopillar with 16 mA as a function of time. As expected from the observation of the individual layers, only a fraction of the full GMR signal is reached. (c) As I increases, there is less difference between the relative switching time between the free and reference layers as seen with 24 mA of current. (d) The MR response at 24 mA illustrates the behavior where there is less coherence in the oscillation.

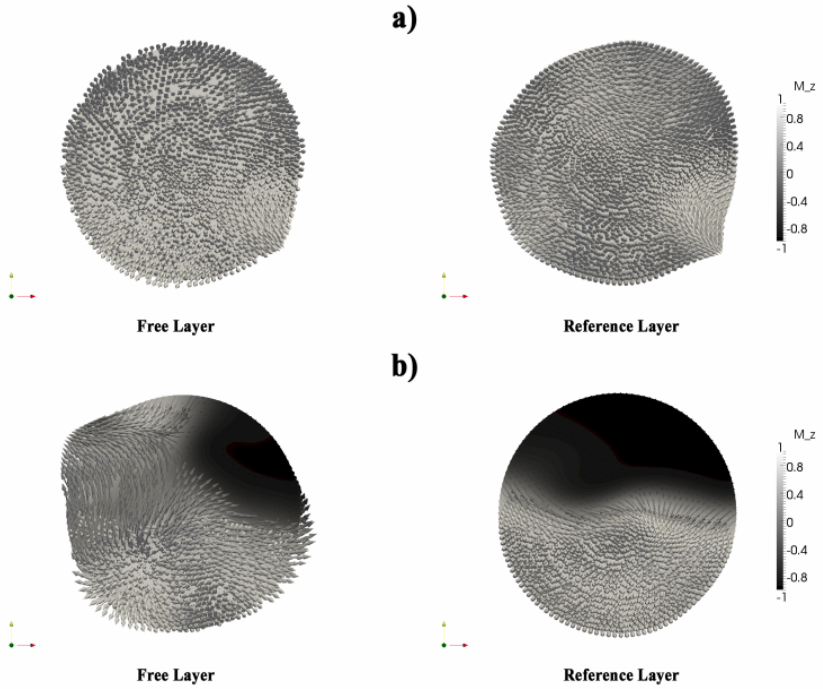

Figure 2.10 Simulation data visualized in both relative P and AP states with identical axis orientation on both layers. This visualization illustrates the nature of the magnetic configuration during oscillation. Neither layer is able to have its moment fully polarized within the layers, thus these are not absolute P or AP state as shown in Figure 2.1, but rather (a) relative P and (b) relative AP states.

2.8 Single and Multi-Domain State

One curious behavior this type of system can exhibit is the formation of a non-oscillating domain state. The tendency of the device is to oscillate with the potential oriented as polarization B as shown in Figure 2.3. Generally the device will not oscillate in the opposite polarization, and the simulations further show that the system can lock into a stable, non-oscillating state. This was observed with the current applied

in the opposite polarization as Figure 2.9 but for otherwise identical conditions. This state has a parallel alignment of the magnetization between the free and reference layers.

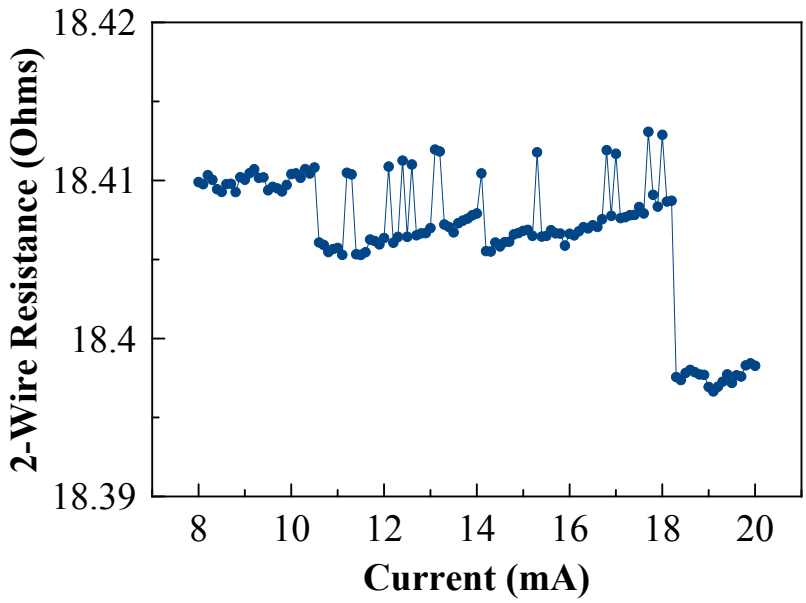

Figure 2.11 Two-Wire resistance of nanopillar to measure a change in the reference layer using the method in Ref. [24]. The intermediate region indicates a multi-domain state.

This stable state may explain why no oscillation signal is observed for this current direction in physical devices. However the simulations do suggest with sufficient current, the device may oscillate even in this current direction, although it exceeds the Joule heating limit of the devices. Another phenomena that was observed in simulation and measurement was the multi-domain state of the device with current

driven in this same polarization. Figure 2.11 shows an intermediate state with the current excitation between 10mA and 18mA. The device resistance was measured using the same method Ref. [24] with 1000 Oe bias field. Since the device is measured with the free layer in a known state, the results indicate that the reference layer did not completely reverse with the current excitation between 10mA and 18mA, and rather is in a multi-domain state. This type of stable multi-domain behavior is especially common in an elongated aspect ratio device like the one pictured in Figure 2.12. With the current in the reverse polarization than that in oscillation, the device does not enter a single domain state, but rather stabilizes into a two-domain state.

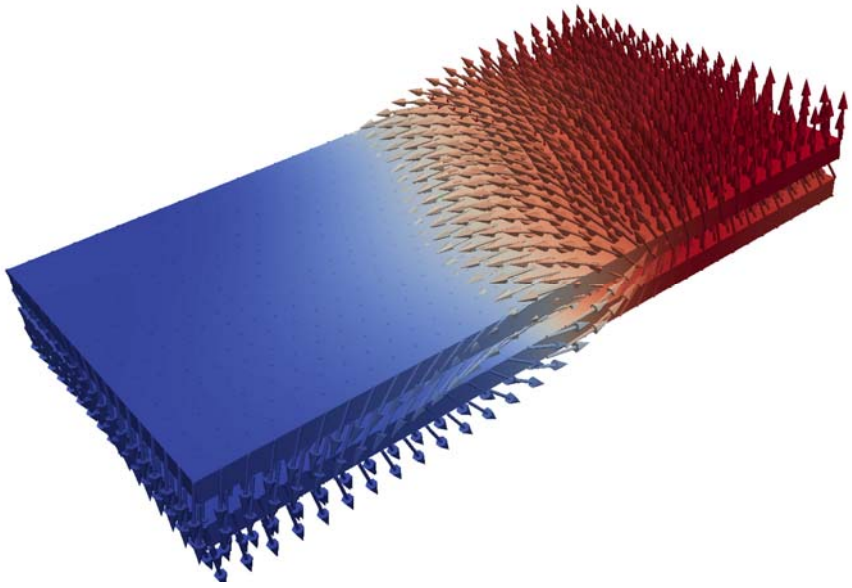

Figure 2.12 Simulation data visualized for a 2:1 aspect ratio rectangular nanopillar. With certain magnitudes of current in a certain polarization, the nanopillar will stabilize into this type of two-domain state.

2.9 Summary

We demonstrated the first experimental observation of pinwheel oscillations in PMA nanopillar spin valves which exhibit tunable oscillations from repeated and high speed switching of both free and reference layers. These devices are able to switch at a frequency in the microwave regime using only DC sources, and the overall switching behavior is dominated by the characteristics of the reference layer. For current in the reverse direction these devices tend to lock into a stable state, and depending on the geometry of the device it may tend to lock into a single domain or multi-domain state.

Chapter 2, in part, is a reprint of the material as it appears in IEEE Transactions on Magnetics 2016. R. Choi, J.A. Katine, S. Mangin, E.E. Fullerton. The dissertation author was the primary investigator and author of this paper. I would like to thank the Vitaliy Lomakin computational electromagnetics and micromagnetics group for access to the FastMag micromagnetics simulator. Majd Kuteifan, Marco Lubarda and Iana Volvach for their assistance in running the FastMag software. The research in this chapter was supported by the Qualcomm Fellow-Mentor-Advisor (FMA) Program and the NSF award DMR #1312750. As well as ANR-NSF Project, ANR-13-IS04-0008-01 "COMAG."

Chapter 3: Tunable NMOS-Magnetic-Tunnel-Junction Ring Oscillators

3.1 Introduction

One of the most common and prominent integrated circuits in modern very large scale integration (VLSI) designs is the ring oscillator (RO). The standard implementation of the RO is simply an odd number of identical CMOS inverters assembled in a closed loop. This forms an unstable negative feedback loop that produces an oscillating voltage when powered.

This important RO circuit serves a multitude of different purposes from process monitoring of CMOS components [36] to clock generation as a voltage controlled oscillator [37]. However, the design of a CMOS RO involves several engineering trade-offs such as power, speed, area, and noise (*i.e.* jitter and phase noise).

As part of this work, we've introduced a new RO scheme incorporating MTJs into the inverter structure as a hybrid spintronic CMOS device [38]. With this method we've created highly-tunable MTJ-RO which exhibit voltage controlled oscillator gain of 300-500 MHz/V, tunable with both voltage and magnetic fields, with the possibility of tuning the output with magnetic field we enable an additional degree of freedom in

RO design.

3.2 Ring Oscillators

Conventional CMOS ROs use an odd-numbered chain of CMOS inverters with feedback. This circuit returns an inverted input from the last inverter stage to the first inverter stage to the input to create a stable oscillating output.

A standard inverter stage (Figure 3.1) consists of an NMOS and PMOS transistor with their gate and drain connected to provide an input and output respectively.

Each inverter contributes a signal delay [39] to the overall chain given by

$$\tau_d = \eta \frac{v_{DD}}{i_d} C_{TOT}$$

Equation 3.1

where i_d = current flowing in each stage, v_{DD} = voltage applied across each inverter stage, η = proportionality constant, and C_{TOT} is the load capacitance in each stage from the NMOS devices. The frequency of an RO is determined by,

$$f_o = \frac{1}{2N\tau_d}$$

Equation 3.2

where N is the number of inverter stages.

One advantage of CMOS ROs is that they have a smaller silicon footprint and consume less power than other oscillator configurations [40]. PMOS transistors are typically larger than their NMOS counterparts due to poorer carrier mobility in P-type materials [41]. In an effort to further reduce device size, lower power consumption, and demonstrate a uniquely unique design that will allow us to tune the circuit by using both magnetic field and current, we have fabricated ROs by replacing the PMOS transistors in the inverter with MTJ devices (as represented in Figure 3.2). Two types of MTJ ROs were fabricated using a TSMC 40-nm logic process, consisting of either 21 or 31 stages of MTJ-CMOS inverters.

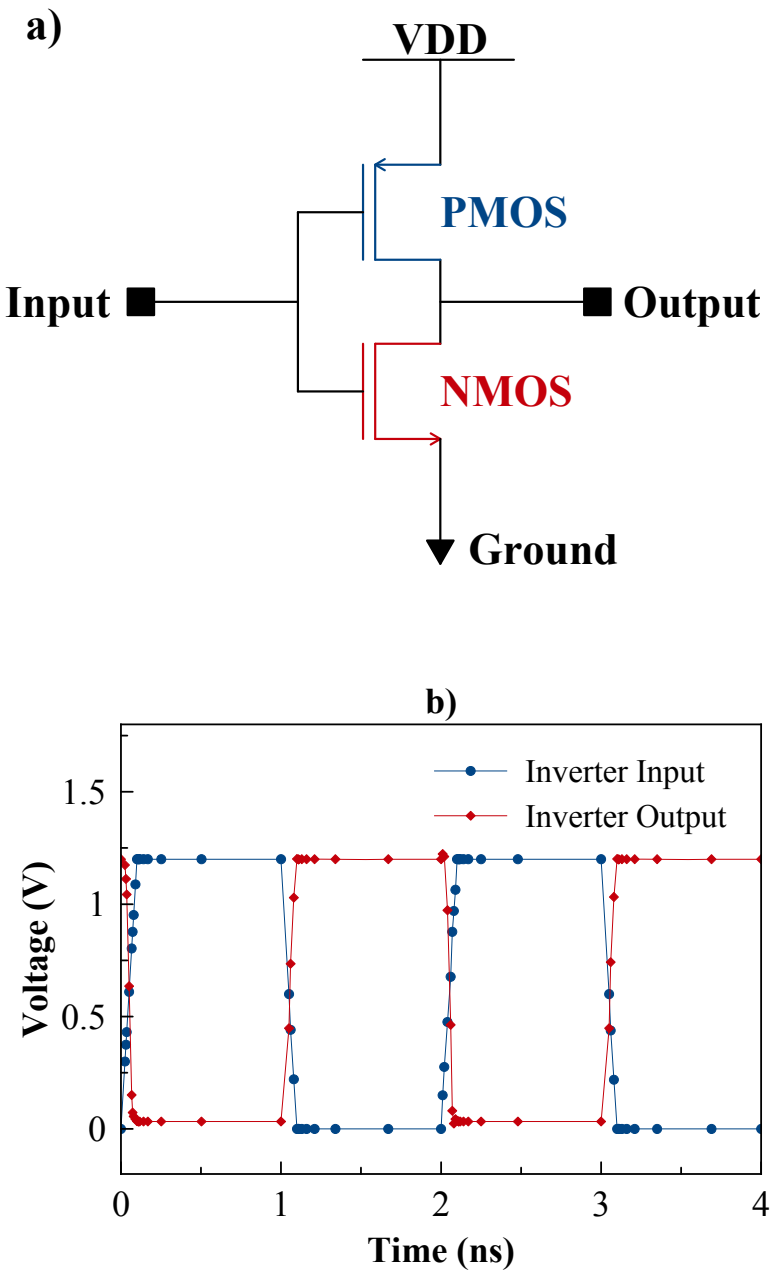

Figure 3.1 (a) A representative schematic of a CMOS inverter. (b) Typical input output characteristics from an inverter.

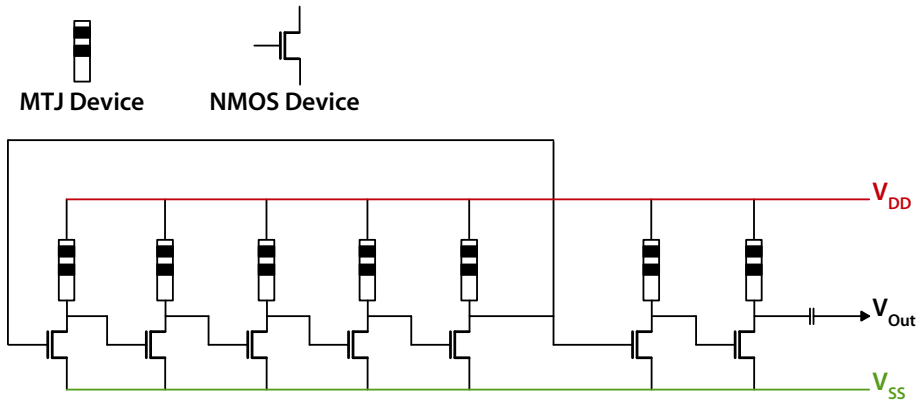

Figure 3.2 Representative schematic of a 5 stage MTJ ring oscillator.

When designing the MTJ-RO, we need to take into consideration the same design methodology as with a standard CMOS RO. We start by inserting an MTJ SPICE model into a single inverter to replace the PMOS device and running a study of the inverter transfer characteristics. The device needs to be designed such that current that flows through is balanced between the MTJ and the NMOS transistor, this is a difficult task since the MTJ changes resistance depending on the magnetic configuration of the layers thus changing the current, so we run a parametric sweep for NMOS sizing to balance against the average resistance of the device.

These voltage transfer characteristic (VTC) curves in Figure 3.3 show us what sizing for the NMOS transistor provides the most balanced responses. We chose a sizing of 2.13 μm for these TSMC 40nm NMOS SPICE models. Once we settled on the NMOS sizing, we simulated the VTC results (ignoring switching events) with the MTJ

in either the P or AP state Figure 3.3 (b).

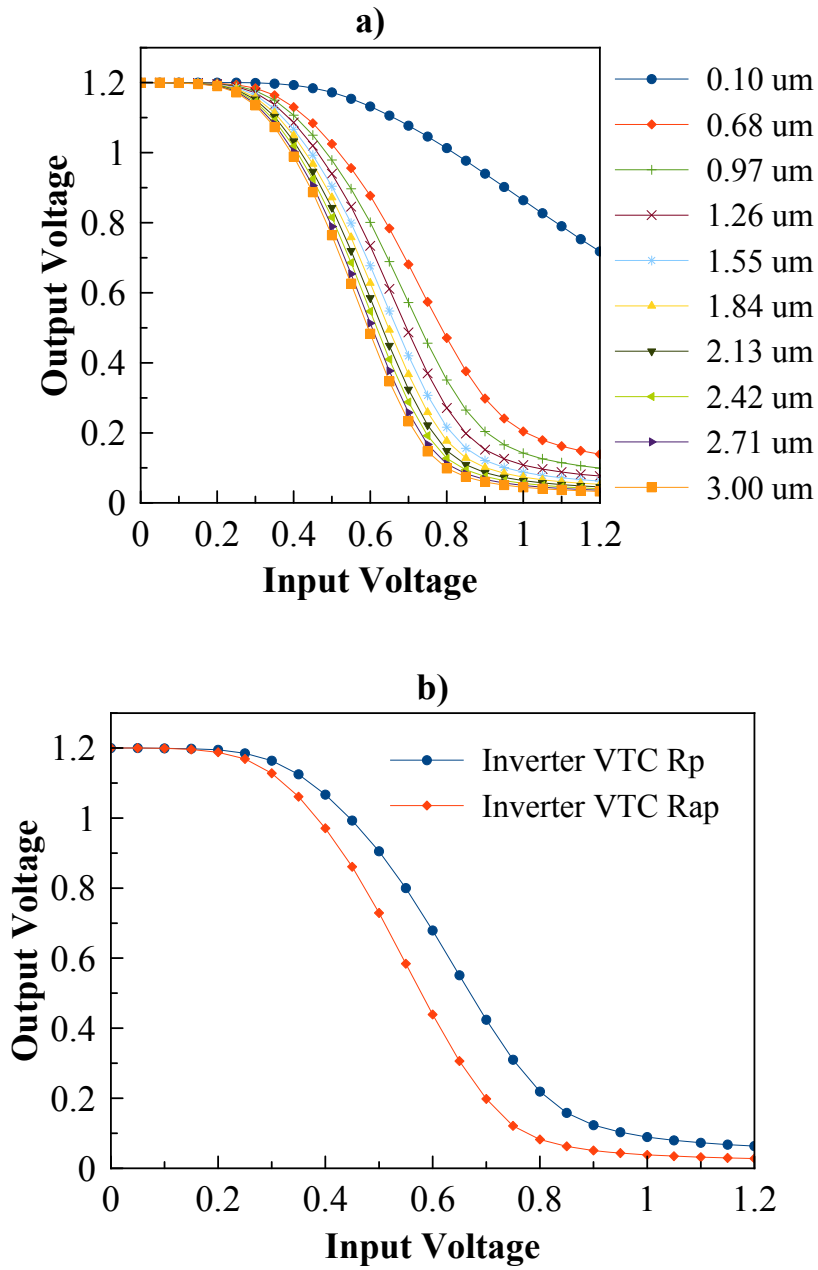

Figure 3.3 (a) VTC curves showing the input-output response of the MTJ-NMOS inverter with variable NMOS sizing. (b) Inverter VTC curve showing the difference in VTC with the MTJ in the P and AP configuration.

The devices presented in the rest of the chapter represent similar devices to those designed as described above. For future iteration of devices for study, additional design considerations should be undertaken. As of time of writing these devices will not be yet fabricated for measurement, however the design portion is described. The first improvement is a better control mechanism, we want to add a biasing circuit (Figure 3.4 (a)) and current starving elements (Figure 3.4 (b)) to act as a current mirror to set the current at each inverter stage using voltage.

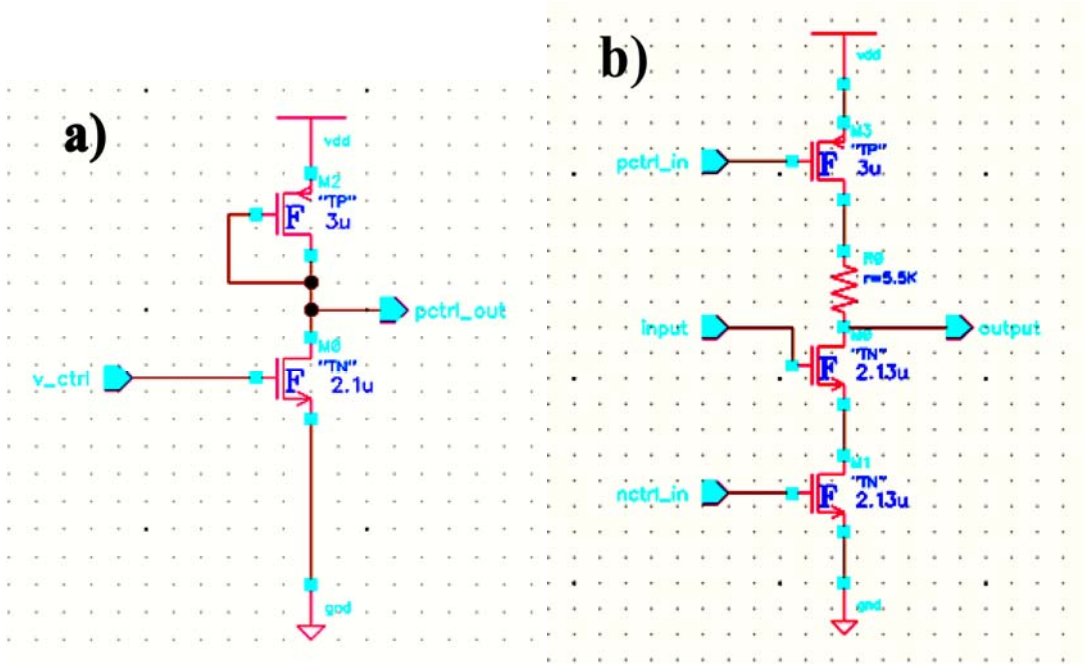

Figure 3.4 (a) The biasing circuit and the (b) inverter with current starving elements added. This will allow an input voltage to adjust the current in each inverter stage without modifying the V_{dd} source voltage.

A rudimentary simulation allows us to verify the tunability of the RO using the

biasing circuit and current starving elements. We simulate a 5-stage RO to verify proper operation Figure 3.5.

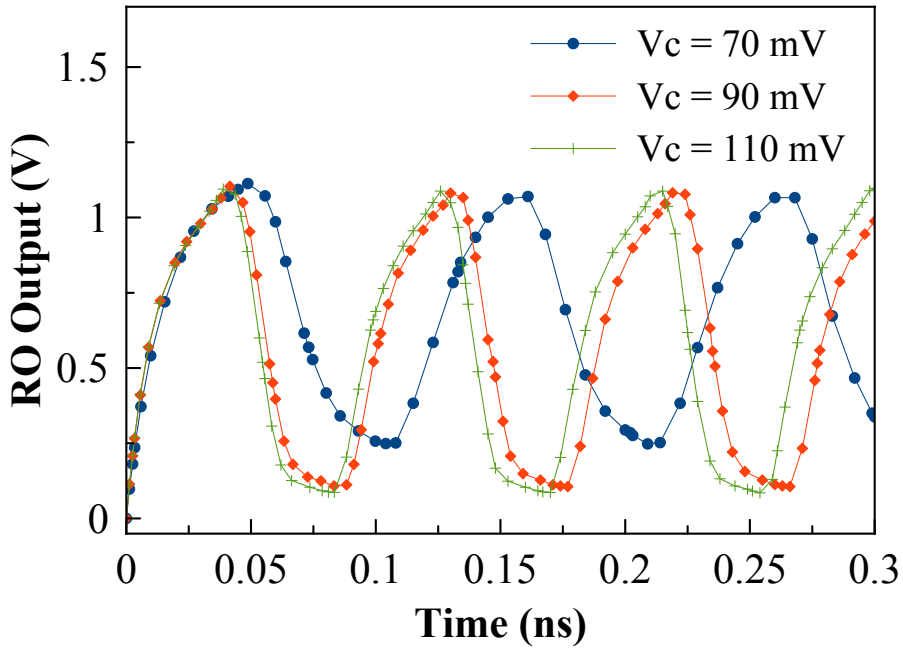

Figure 3.5 Basic demonstration of tunability in these MTJ-RO simulations.

Another critical feature of the overall RO circuit is an output buffer. In order to drive large loads, a multi-stage inverter series is used where each progressive stage is sized larger as shown in Figure 3.6. This minimizes input capacitance at the start of the buffer stage to reduce effect on the RO performance and increases the max load the RO can drive at the output of the buffer.

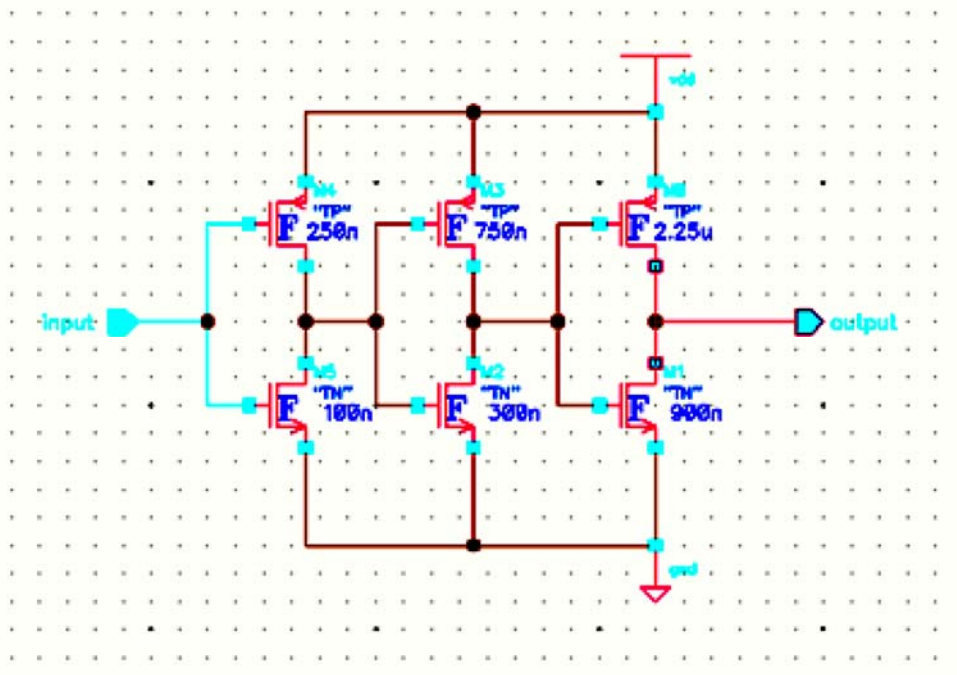

Figure 3.6 The output buffer stage design for an RO. From left to right, each progressive stage scales larger in size. This allows it to have lower input impedance and higher output impedance.

Using the Cadence or any other suite of circuit design and simulation tools, we can simulate various number of stage configurations of RO using these designs for fabrication. We can also use these simulations to also estimate stage delay from, which we find to be approximately 9 ps, using that we know that a 5 stage RO will oscillate at approximately 11 GHz and an 11 stage RO will oscillate at approximately 5 GHz. In the 21 stage RO in Figure 3.7 (a)-(b), we see operation at 2.6 GHz, which is within our expectations. However we also know that once physical devices are fabricated, the MTJ devices will likely contribute to the inverter stage capacitance, so these frequency

numbers are overestimations.

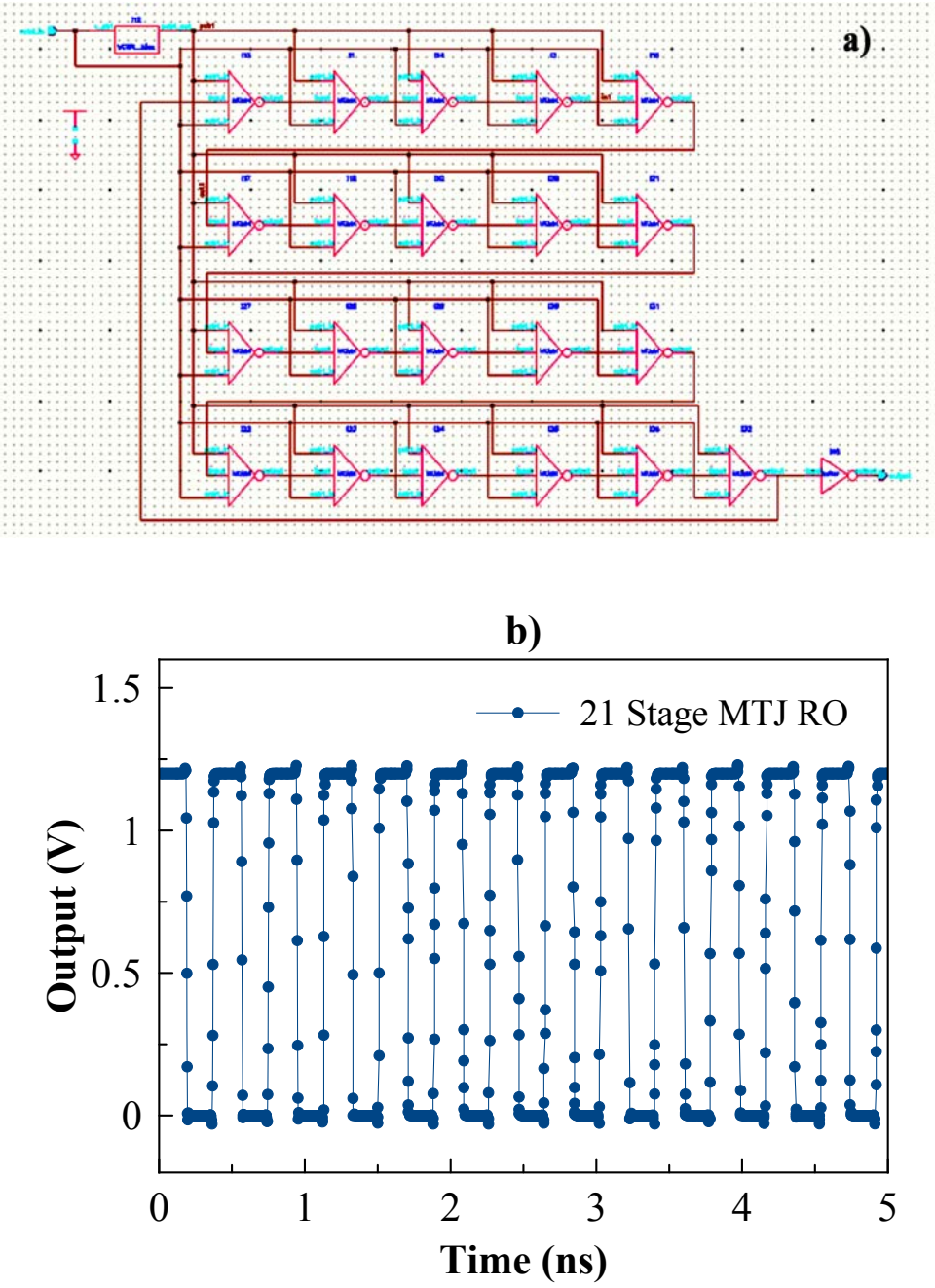

Figure 3.7 (a) SPICE schematic of a 21-stage MTJ-RO. (b) Simulation output showing a base output frequency of approximately 2.6 GHz.

3.3 Magnetic Tunnel Junctions

In typical MTJs, the free layer is engineered with a lower switching field than the reference layer in order to enable disturb free toggling of the resistance state by reversing the free layer where the reference layer remains fixed. The MTJs described in this work are similar to structures used for MRAM and consists of a reference layer, MgO barrier, and CoFeB free layer, patterned into 40x110 nm ellipses to induce a preferred direction for the in-plane magnetic anisotropy. The easy axis of magnetization is defined through the uniaxial shape anisotropy arising from the 2.75:1 aspect ratio of the magnetic elements. The reference layer is strengthened magnetically by being antiferromagnetically exchange coupled through a thin Ru layer to a pinned magnetic layer (to form a synthetic antiferromagnetic). The pinned layer is then coupled to an antiferromagnetic IrMn layer. [42].

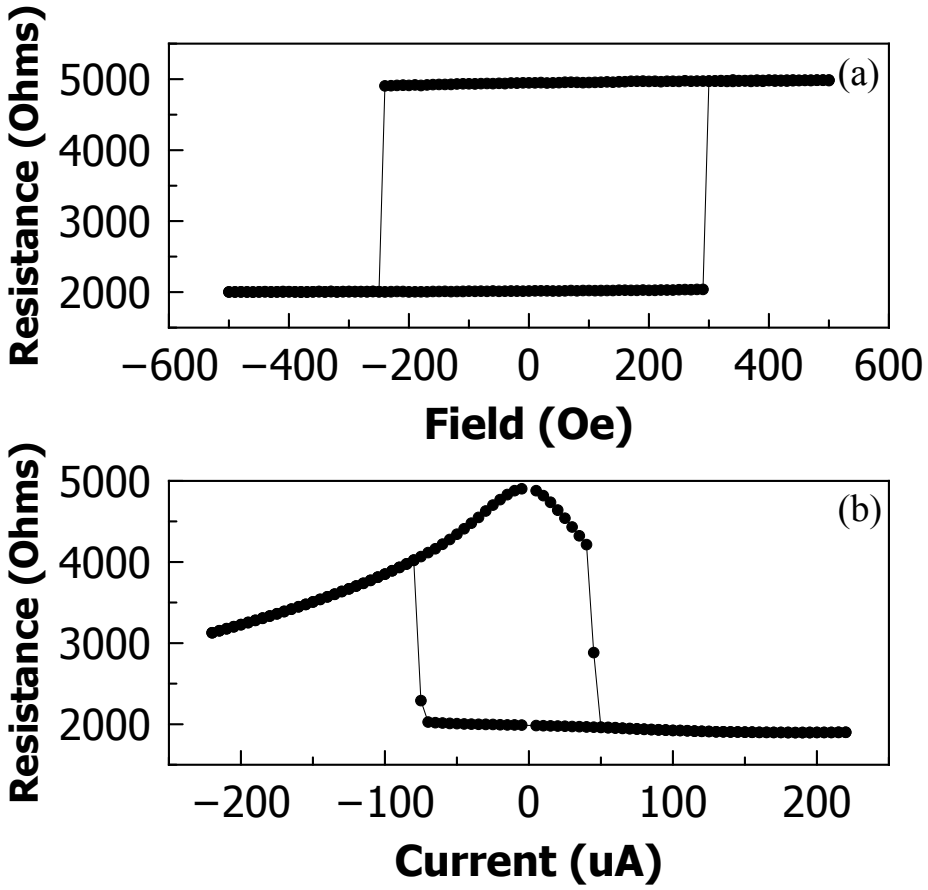

Figure 3.8 Magnetic hysteresis of the free layer of a single MTJ in response to either (a) an external magnetic field or (b) an injected current in zero applied magnetic field.

Characterization of individual MTJ devices was performed by traditional two-terminal magnetotransport techniques and MTJ-RO structures were contacted by GSG RF probes. The output signal was buffered from the input power, so no filtering of the microwave signal was implemented before measurement by a digital oscilloscope (for time domain analysis) and spectrum analyzer (frequency domain). Figure 3.8 (a) and (b) demonstrate the response of a typical MTJ device (that has not

been integrated into a RO) to magnetic fields and electrical currents, respectively. The TMR is ~145%, typical MTJ free layer coercivity is 250 Oe, and devices have a DC critical switching current of 50-70 uA.

Running an identical set of device characterization measurements over both a range of field and current, the effect of thermal stability is made clear when we measure these devices with different relaxation times and assemble this data into a switching state diagram (SSD) shown in Figure 3.9 and Figure 3.10. These SSD are assembled by subtracting the difference between the hysteresis loop like those pictured in Figure 3.8.

The result is mapped out to a plane with current and magnetic field axis. The central portion with high values (as indicated by the z-axis legend) indicate a delta in the hysteresis loop, or the bistable region of the hysteresis. The boundaries between this region and the edge region represent the switching values.

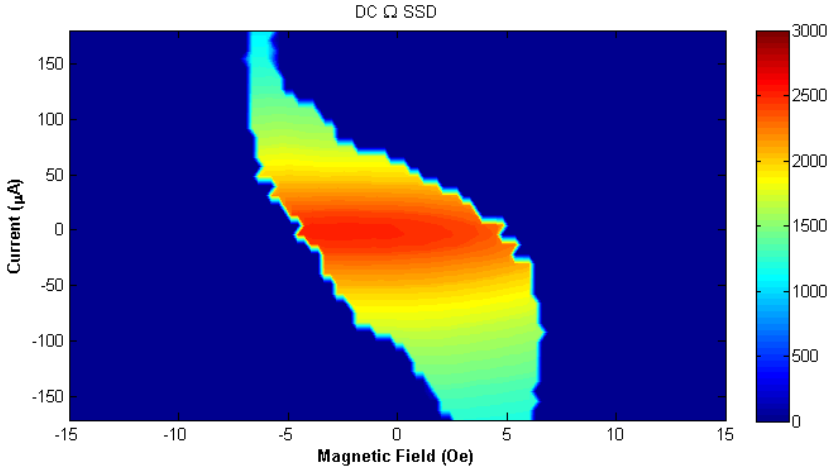

Figure 3.9 A switching state diagram for the MTJ with 100ms integration time.

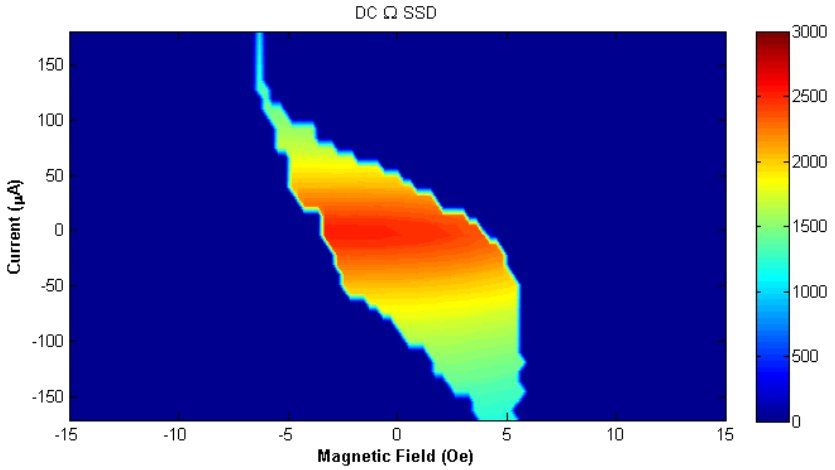

Figure 3.10 A switching state diagram for the MTJ with 10,000ms integration time.

The effects of thermal stability are clear when Figure 3.9 and Figure 3.10 are compared. The integration time indicates how long the device is exposed to stimuli (field and current) during a sweep. The longer integration time of 10 seconds in Figure 3.10 compared to 100 milliseconds in Figure 3.9 allow room temperature thermal

instability to cause switching in these devices at lower field and current values.

3.4 Hybrid Ring Oscillator

The large change in resistance makes the MTJ device an excellent candidate to replace the PMOS as a ballast resistor in the inverter structure. The response of two different MTJ-ROs with 21 and 31 stages is shown in Figure 3.11. The RF time domain signals from the 21- and 31-stage MTJ-ROs are shown in Figure 3.11 (a), the voltage dependence of the output frequency (kVCO) is shown in Figure 3.11 (b), where the 31 stage MTJ-RO has a distinctly lower kVCO due to the fact that as these MTJs switch, the overall contribution to the RO frequency is less due to the fact that it's averaged over more devices. Though oscillations could be observed over a wide range of input voltages (V_{DD}), the magnitude of the output voltage is optimized at approximately V_{DD} = 0.85 V. Table 3.1 compares the frequency, output voltage, quality factor, and other metrics of the 21 and 31 stage MTJ-ROs.

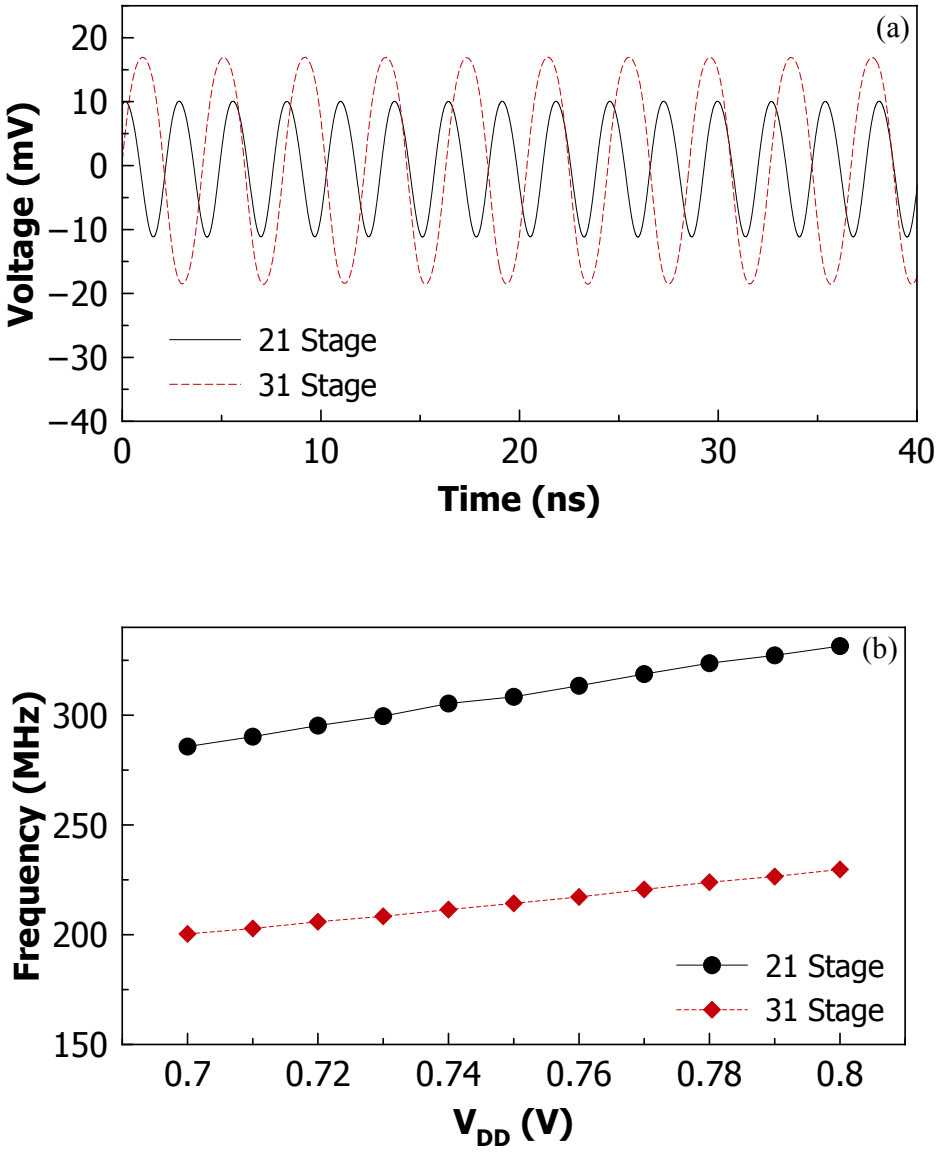

Figure 3.11 (a) Transient response of a 21-stage and 31-stage RO. (b) Demonstrated V_{DD} tunability of MTJ-RO devices to voltage.

Table 3.1 Performance of 21 and 31-stage MTJ-RO with VDD = 0.85 V

MTJ-RO Stages	Vout (mV)*	fo (MHz)	Q-factor	kVCO (MHz/V)	RMS Jitter (ps)	Phase Noise † (dBc/Hz)
21	21.4	369	2856	503.9	6.8	-83.24
31	35.6	245	2952	296.13	7.8	-87.01

*Peak to peak output voltage.

†Measured at alternate VDD = 1.1v

As expected from the additional delay stages, the frequency of the 31-stage RO is proportionally lower than the 21-stage RO, but spectral properties such as Q-factor, RMS Jitter, and phase noise are maintained. Figure 3.12 (a) shows the phase noise response of the 21-stage and 31-stage MTJ-RO with the frequency domain of both devices shown in Figure 3.12 (b). At a 1-MHz offset, the phase noise is -83.24 dBc/Hz for the 21-stage RO and -87.01 dBc/Hz for 31-stage RO. The noise figure is comparable with similar CMOS implementations of ROs [43-47]. A small drop in phase noise was observed with an increase in the number of stages due to an averaging effect of process variations over an increased number of MTJs.

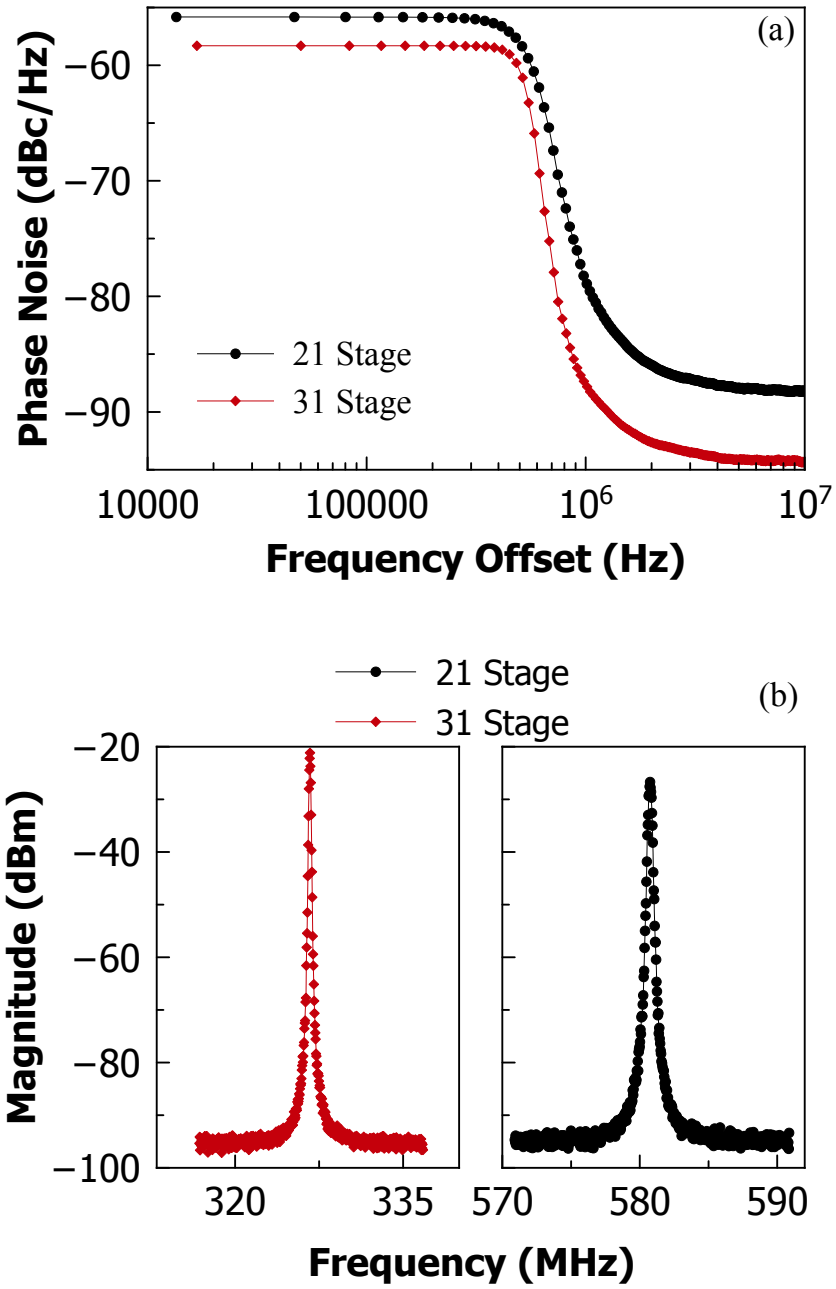

Figure 3.12 (a) Phase noise response as a function of frequency offset of a 21-stage and 31-stage MTJ RO. (b) Spectral response of the same 21-stage and 31-stage MTJ RO measured at VDD = 1.13 V in the absence of a magnetic field.

Using Equation 3.1 and

Equation 3.2, effective capacitance and stage delay were estimated to be 14.4 fF and 130 ps, respectively. By observing the supply current during operation, the power consumption per MTJ-RO stage was measured to be approximately 85 μW. Table 3.2 shows a comparison of several metrics of ROs, including our design indicating a positive direction in wafer size reduction.

Table 3.2 Performance of various CMOS-based ROs from the literature compared to the currently investigated MTJ-CMOS RO

	[11]	[12]	[13]	[14]*	[15] **	MTJ-RO
Process (nm)	180	130	90	45	600	40
fo (MHz)	1017.5	340	3150	341	850	320
Power (mW)	26	7	10	0.002	26	2.6
Wafer Area (mm2)	-	0.2	0.1	-	1.2	0.01†

* Simulation

** LC tank

†Core Circuit Only

As demonstrated in Figure 3.13 (a)-(c), we measured the spectral and noise performance of these oscillators with respect to temperature within the range of 25 - 85 °C and found no substantial change in performance.

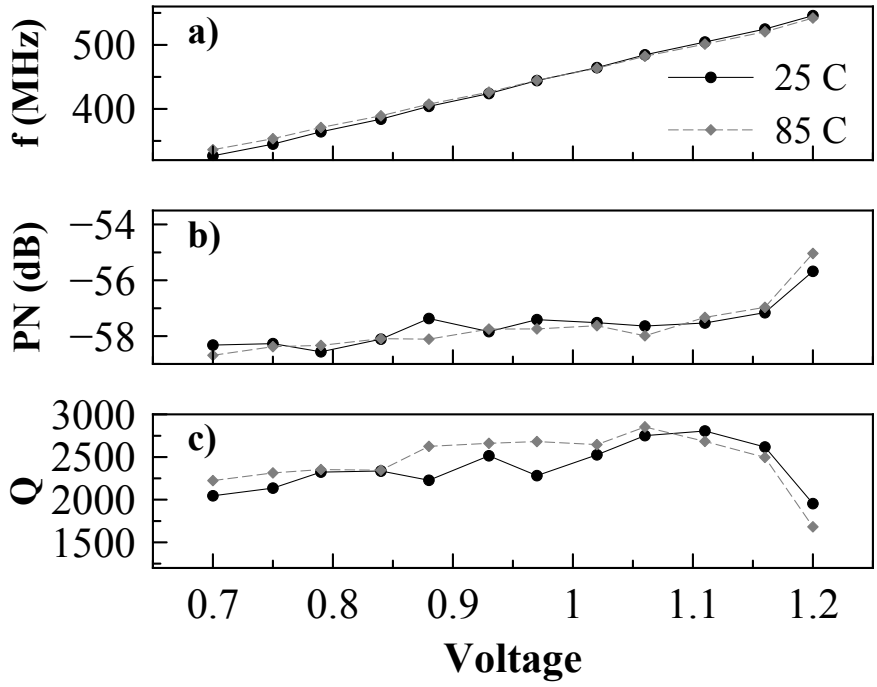

Figure 3.13 Tuning performance of the MTJ-RO showing (a) Output frequency of 31 stage MTJ-RO at 25C and 85C. (b) Phase noise at a 100 kHz offset of the same MTJ-RO at 25C and 85C. (c) Q-factor of the MTJ-RO at 25C and 85C.

As mentioned previously, the resistance of individual MTJ cell changes dramatically as magnetic field is applied to the device while in operation. When integrated with an NMOS transistor, this results in an adjustment of the drain current, and thereby modulates the time delay in the inverter stage. The output frequency *vs*. magnetic field response of a 31-stage MTJ-RO device is shown in Figure 3.14. The external magnetic field is applied parallel to the semi-major axis (magnetically easy axis) of the elliptically patterned MTJ devices. Three distinct regions in the frequency *vs*. field curve are observed, depending on the magnetic state of the MTJs in the RO

structure. Without any magnetic field applied, the MTJs are in an AP configuration (high resistance state) and the device operates at 233 MHz. With upwards of 400 Oe magnetic field, all 31 devices are in a saturated P configuration (lowest resistance state), and the MTJ-RO operates at 347 MHz. In between these two extremes, an intermediary, tunable region exists where a fraction of devices exist in the AP state, while the remainder are in the P state. Integrated magnetic field generation has been previously proposed via field generated by flux concentrating cladding layers [48], additionally there is the possibility of using micro electromagnets to generate fields [49].

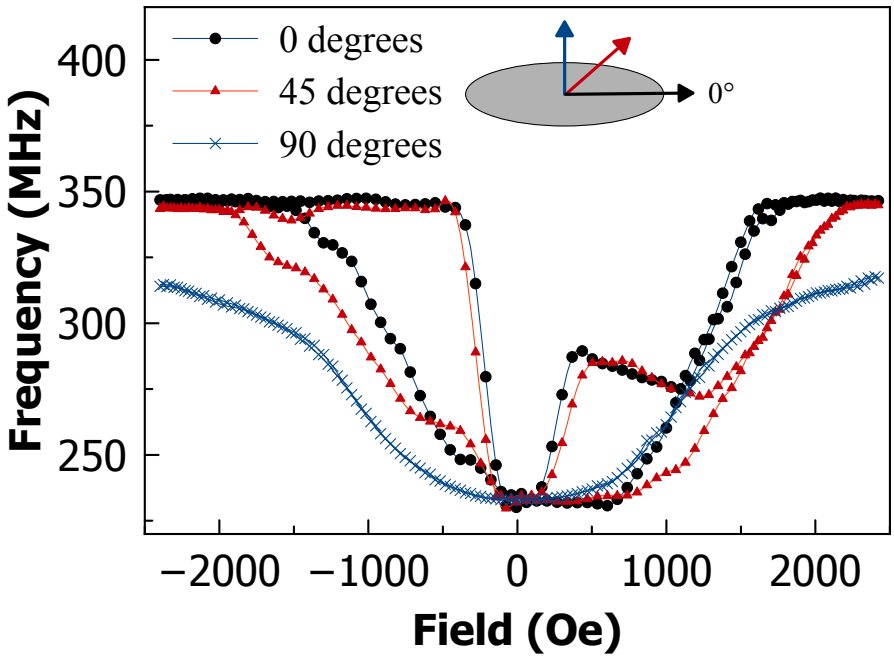

Figure 3.14 Frequency tunability of 31 stage RO with applied magnetic field in varying orientations to the device.

3.5 Switching Field Distribution

While the magnetic characterization of individual MTJ devices show a very abrupt change in resistance when the applied field increases past the coercive field, we observe a more gradual change in frequency in the integrated MTJ-RO devices (Figure 3.15). This is due to the switching field distribution (i.e. the device-to-device variation of the coercive field) [50] of the 31 different MTJs causing an overall continuous change in drain current *vs*. magnetic field.

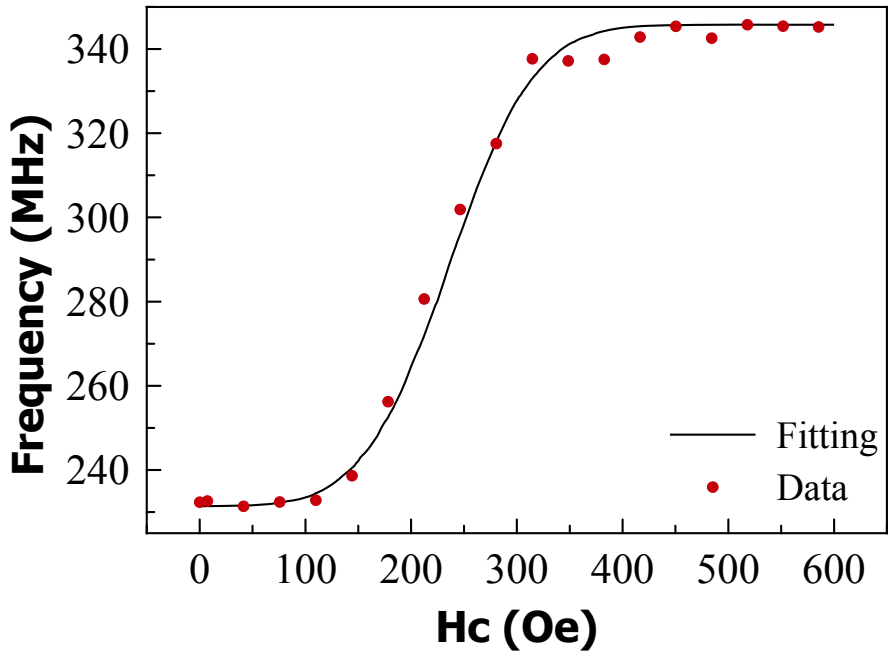

Figure 3.15 Distribution of frequency of MTJ RO for switching of the free layers with applied field. A fit of the curve to (4) and (5) is given by the solid line and gives the average coercive field (235 Oe) and coercive field distribution (65 Oe).

Due to the statistical nature of the switching field distribution, we can generate a simple model of the frequency *vs.* field behavior of this system by comparing to a standard Gaussian cumulative distribution function (CDF) and use this measurement to extract the standard deviation and mean switching parameters. We use the mean H_c to fit the measured data to the CDF:

$$CDF\,(x \mid \mu, \sigma) = \frac{1}{2}\left[1 + erf\left(\frac{x-\mu}{\sigma\sqrt{2}}\right)\right]$$

Equation 3.3

$$f \propto \sum \frac{1}{R_n}$$

Equation 3.4

where *f* is frequency and *R* is the resistance on each individual device in an #n chain MTJ-RO. RO frequency is inversely proportional to stage delay, which is in turn inversely proportional to drain current. Using this fitting method, we find a mean switching field of 235 Oe with a standard deviation of 65 Oe, which is consistent with magnetotransport characterization of a population of similar MTJ devices.

The behavior of the MTJ-RO is highly dependent on the relative angle of the applied magnetic field. As shown in Figure 3.14, when the angle between the applied field and the magnetic easy axis is increase from 0 to 90 degrees, a dramatic shift in the frequency *vs*. field response was observed. For the 90 degrees case, the magnetic field is oriented along the magnetically hard axis of the MTJ devices, and no hysteresis is observed. This is because the increasing application of magnetic field along this direction only results in a slow, gradual rotation of both the reference and free layer magnetic moments from the AP to P state. If larger magnetic fields could be applied, the eventual orientation of both layers would be collinear along the hard axis, and

frequency would approach the maximum value of ~347 MHz.

At 0 and 45 degrees, large, hysteretic changes in the frequency are possible as the free and reference layers of the MTJs are toggled between P and AP states as the field is swept. The relative magnetic orientations that correspond to switching events and plateaus in the 0 degrees plot are shown in Figure 3.16 (a) and (b), where the top layer represents the free layer, the middle layer represents the reference layer and the bottom layer represents the pinned layer. There is an asymmetry in the frequency *vs*. field, which is caused by structure of the exchange biased pinned layer which is antiferromagnetically coupled with the reference layer.

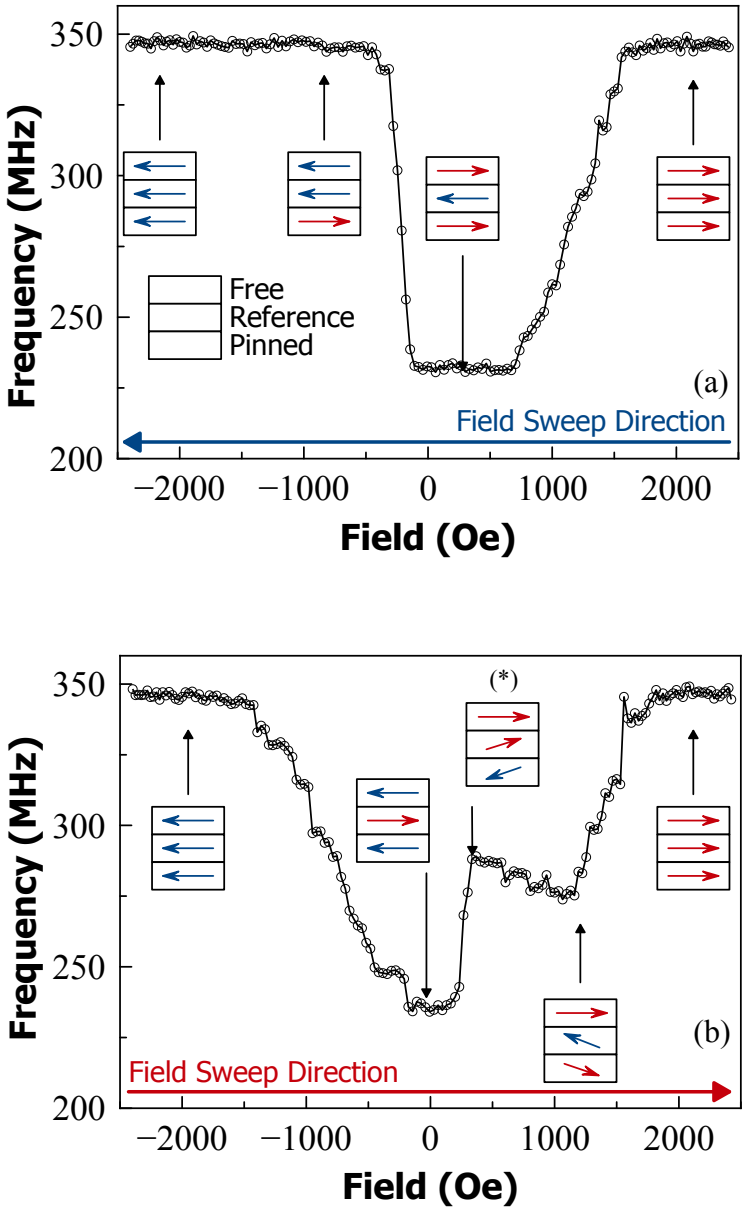

Figure 3.16 (a) Magnetic state diagram during field manipulation of the MTJ RO with field being swept in the positive direction (b) and in the negative direction. The stack diagram illustrates the orientation of the free, reference and AFM pinned layers, collectively the AF coupled reference layer and pinned layer form the SAF structure.

In both high-frequency states (at high field), the free and reference layer

magnetizations are oriented parallel to the applied field. As the field is reduced from +2500 Oe towards 0 Oe in Figure 3.16 (a), the antiferromagnetic exchange coupling between the reference and pinned layers causes a rotation in the reference layer to become antiparallel to the free layer. The device is then in the AP state at H = 0 Oe. When H > Hc, the free layer switches and the devices enters the P state again at saturation. This behavior is illustrated in the resistance vs. field characterization of a single MTJ devices in Figure 3.17.

At high field magnitudes, both reference layer and pinned layer becomes magnetized in the field direction, this process inverts itself in Figure 3.16 (b) when ramping field in the opposite direction from -2500 Oe to +2500 Oe with a single exception. Since the pinned layer is exchanged biased in one direction, there is an asymmetry of the reference layer reversal. In addition to this, spin-polarized current is actively flowing through the device, increasing the sensitivity to field.

This combination causes the reference and free-layer orientations to enter a metastable state at the (*) in Figure 3.16 (b) when the pinned layer begins to change magnetization, and before the device can enter a stable state. As the field is further increased, the free layer and pinned layer stabilizes. Once the pinned layer increases in stability and the field is increased to the point where it overcomes the exchange energy

between the reference layer and pinned layer, the reference layers is oriented parallel with respect to the free layer.

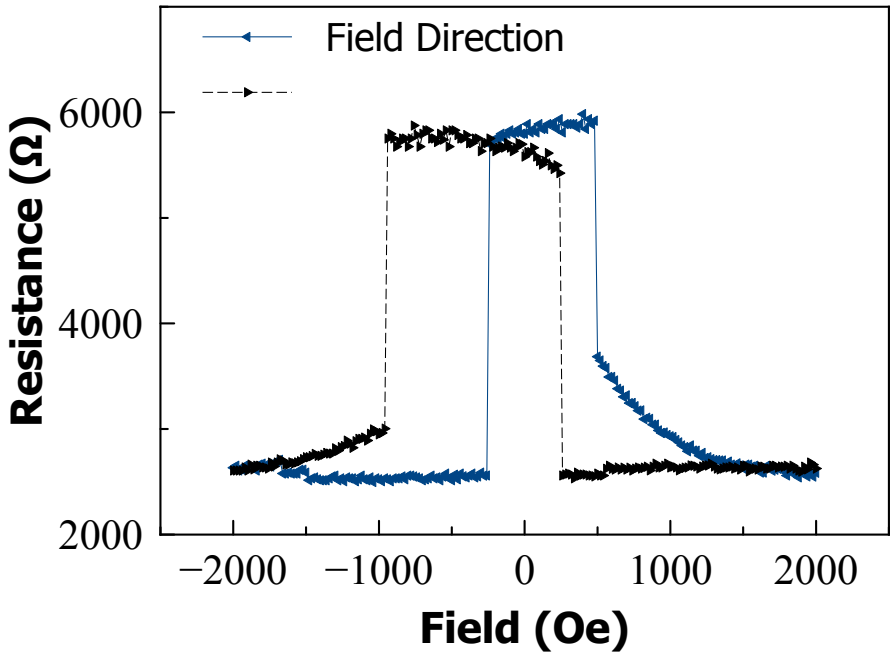

Figure 3.17 The resistance of an individual device versus field is shown as reference to have asymmetrical switching behavior.

3.6 Conclusion

Two variants of a hybrid magnetic-CMOS device known as MTJ-ROs have been studied in this Chapter. The measured RF performance parameters such as output power, frequency, noise, and oscillator gain suggest that this class of devices has the potential to serve as a robust oscillator in several RF applications. Specifically, MTJ-

ROs provide a platform for optimizing the RF performance of ring oscillators that is highly tunable via a combination of voltage and applied magnetic field.

Chapter 3, in part, is a reprint of the material as it appears in IEEE Transactions on Electron Devices, 2016. R. Choi, J.J. Kan, S.H. Kang, E.E. Fullerton. The dissertation author was the primary investigator and author of this paper. This research in this chapter was supported by Qualcomm Fellow-Mentor-Advisor (FMA) Program and the NSF Materials World Network Award #1312750.

Chapter 4: Spin Torque Nano Oscillator

4.1 Introduction

The basic operation of a spin torque nano-oscillator (STNO) is that of any GMR or TMR spin transfer device designed to operate in perpetual precessional oscillation using DC spin polarized current to generate a high frequency output signal. Typically most spin transfer devices, despite the intent of their original design, can be made to operate as an STNO by using spin torque to drive microwave oscillation[51, 52].

Surprisingly, the practicality of such a device is very high. With the proper device design, both a high speed oscillator [19] and an oscillation detection device through the spin torque diode effect [22, 53] can be made using the same principle, with the reference layer orientation on a parallel or perpendicular axis with respect to the free layer being the main distinguishing feature.

While there are also strong interest in these types of devices to create a class of low power, purely electronically controlled devices which exploit magnetic materials to create microwave nano oscillators and detectors, there is also the ability to probe material properties and underlying physics in STNOs through characterization studies.

4.2 Precessional Dynamics

The behavior of STNO can be explained by examining the Landau Lifshitz Gilbert (LLG) equation from Equation 1.2 with the Slonczewski term for spin torque.

The LLG equation can be broken into 3 components, the field torque component which is the effectively the moment of force perpendicular to the plane formed by the field and magnetization vectors and defines the precession of magnetization; the damping torque component defining the moment of force along the plane formed by the field and magnetization vectors and the spin torque which has a similar effect on magnetization dynamics as the damping torque but depends on the spin polarization of the current.

When you have run electrical current or magnetic field through a spin torque device at a level below switching conditions (or where the spin torque term is much greater than the damping term), the free layer (as it is typically lower in coercivity) can find an equilibrium point between damping and spin torque and will simply precess [54, 55].

Different types of spin transfer devices can be made to precess either through DC sources or from exposure to microwave signals using varying H and current biasing

techniques, creating classes of devices that can generate microwave signals or detect microwave signals.

4.3 High Speed Oscillation in MTJ devices (STNO)

One type of device capable by spin transfer devices is the spin torque nano oscillator (STNO). The theory behind the device is simple, in the event that both spin current and damping torque in a system is balanced such that the combined torques are at equilibrium, the magnetization will precess. This follows the basic model of an auto-oscillator which contains an intrinsic resonance, a damping element, and an active element [56]. In addition, STNO are tunable by current. An inspection of the diagram in Figure 1.5 will show that as spin torque increases, so does the angle between the magnetization and H_{eff}, typically reducing the precessional frequency. Conversely, STNO are tunable by magnetic field under the same principles.

The STNO presented in this section utilize an identical MTJ as presented in Chapter 3.3. In summary, this is a spin transfer device designed as an MTJ memory unit with an MgO tunnel barrier, CFB free and reference layers with an additional layer stack to pin the reference layer resulting in a TMR of approximately 120%. These devices have an in-plane easy axis anisotropy and are geometrically elliptical with a

dimension of 40nm by 110nm.

Measuring the STNO

However, while simply applying current and field will cause the magnetization to precess and therefore oscillate, since the device is configured with the free and reference layer in parallel orientations, as the magnetization precesses, there will be no observed changed in magneto resistance.

In order to electrically measure oscillation, a bias field is applied to tilt the magnetization out from the easy axis, after which current is applied to the device to drive it into oscillation, the output of the device represents a projection of the precession from the free layer onto the hard layer where the amount of change in MR, or the projection of change in the free layer, is a cosine of the angle between the applied bias field and the easy axis.

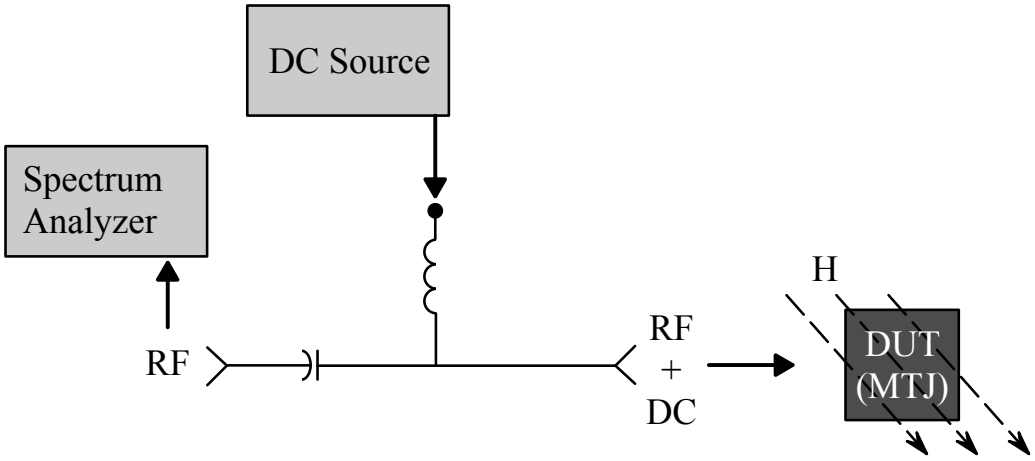

Figure 4.1 Diagram showing how the STNO was measured. The DC source used was a Keithley 2400 source meter, the Spectrum Analyzer was a Agilent E4405B Spectrum Analyzer.

The device is set inside a tilted magnetic field set at an angle of 45 degrees. RF probes are used to connect to the MTJ device pad outs. A bias tee is used to isolate the DC source from the RF measurement tool. The setup is configured as shown in Figure 4.1.

STNO Measurement Results

By applying a fixed current and sweeping field, we are able to verify the field tunability of this STNO as shown in Figure 4.2. While the magnitude of oscillation seems quite high, these STNO were measured with a +30dB amplifier. Because of the direction of field, as the field intensity is increased, it causes the damping response

described in the previous paragraphs cause the oscillations to decrease in frequency.

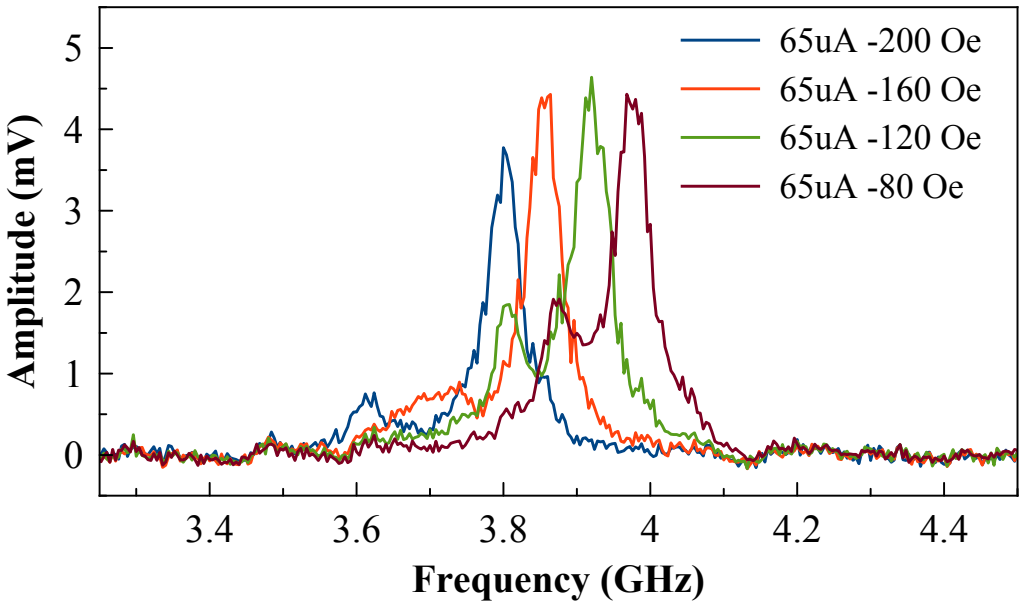

Figure 4.2 Spin torque oscillations measured from an MTJ device. Using a fixed current source, the peak frequency is shown to be tunable as a function of field.

In addition to field tunability, the STNO is also tunable by adjusting the amount of current flowing through the device. However, the main caveat is that while this adjusts the frequency, since the current is directly related to the amplitude of the output, this greatly affects the magnitude of the signal as seen in Figure 4.3.

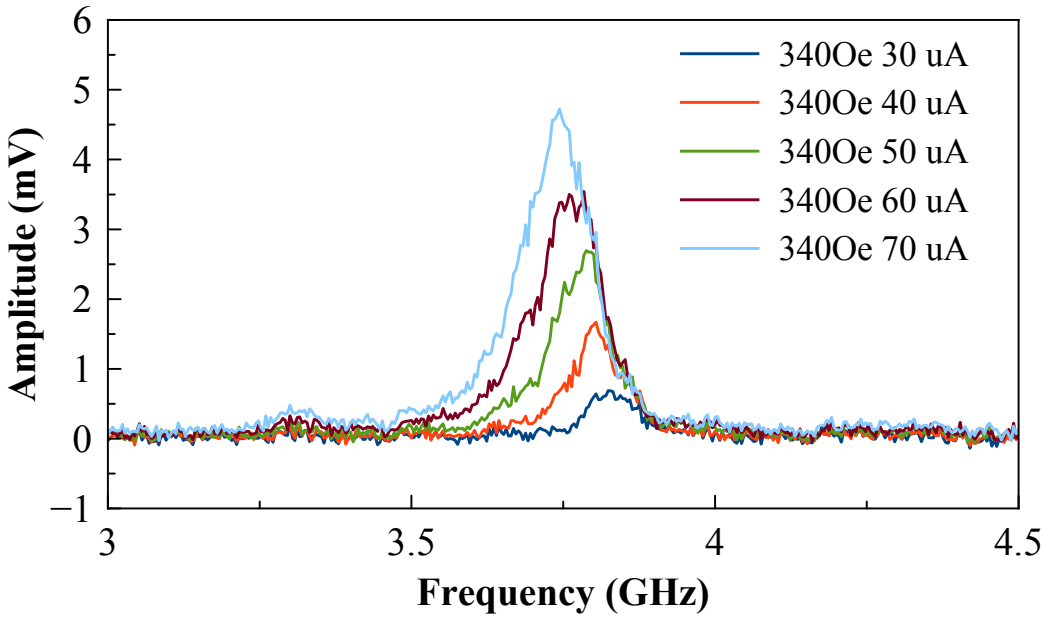

Figure 4.3 Current tunability demonstrated in MTJ STNO devices. Since the output is read using the bias current, the output scales as the input current does.

While the change in amplitude is problematic for a more practical oscillator, it is clear that the oscillator center frequency changes as a function of the applied current to the device. The tunability of the STNO is linear in relationship between both tuning controls (magnetic field or electric current) and the frequency as shown in Figure 4.4.

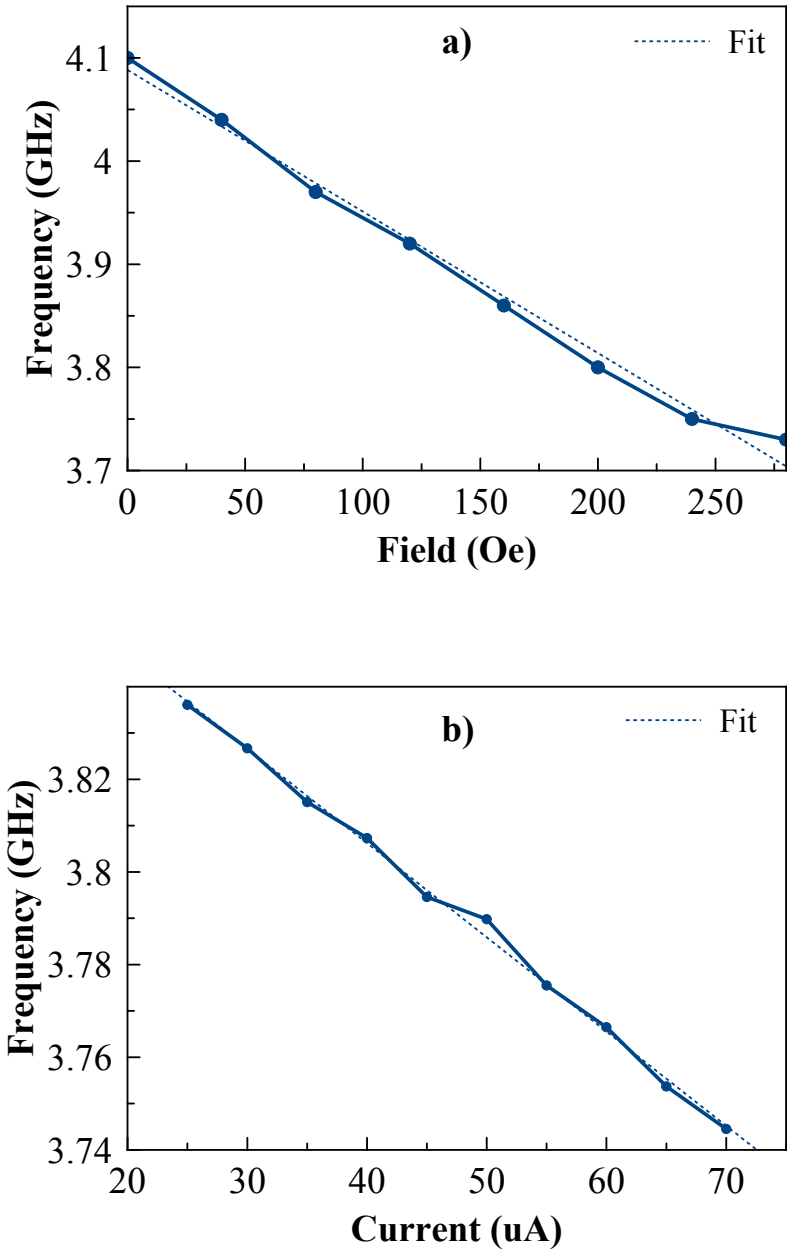

Figure 4.4 The frequency tunability of the STNO device for a) magnetic field control of the STNO. The device has approximately an effective kVCO of 1.37 MHz/Oe with 65uA bias current. b) The current tunability of the STNO device showing an effective kVCO of approximately 2.0347 MHz/uA.

One of the outstanding issues with STNO is that with high drive currents comes the introduction of incoherent spin wave modes [8] which can be somewhat stabilized with addition magnetic field but only to a certain extent. The destabilization is shown clearly in Figure 4.5 where as the magnitude of the current increases beyond a certain threshold, so does the incoherence of the STNO. This results in a widening of the linewidth of the oscillator.

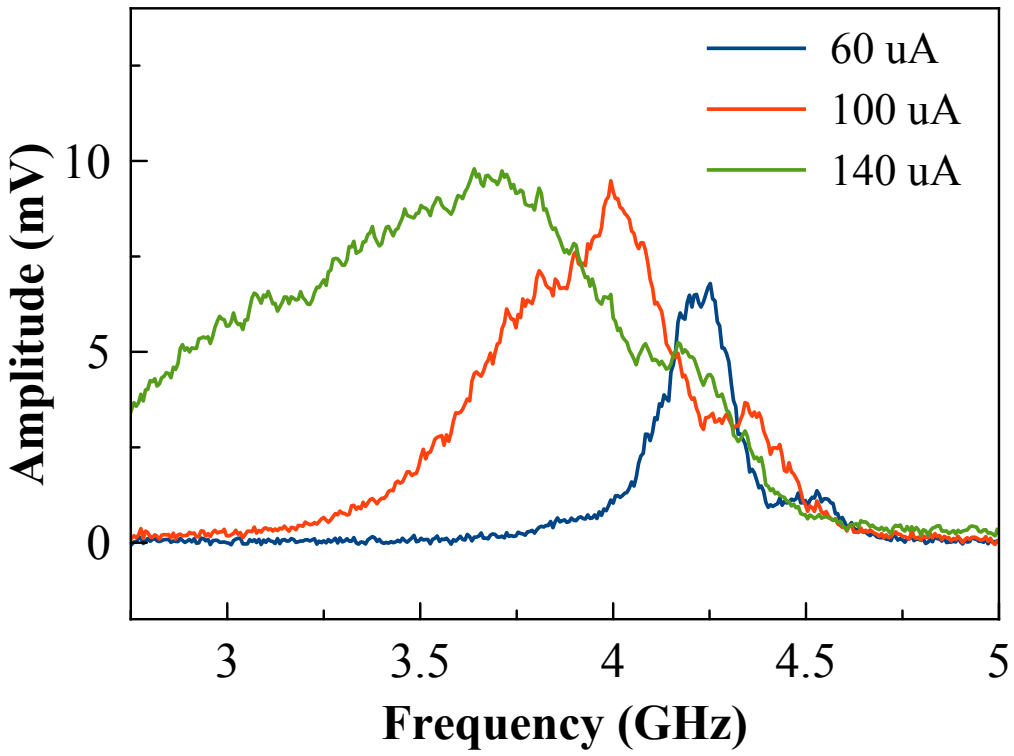

Figure 4.5 An illustration of the breakdown of spinwave modes in an STNO. As current increases, the damping effect causes the frequency to change, but after a certain threshold there is a loss in coherence.

Another issue of the STNO in this configuration is it's tendency to jump between several oscillating states.

A simple way of visualizing this is a car driving on a circular track. If the track is a single lane, there will be very little variation in path the car takes along the track. However if the track has 2 lanes, the car can at any time be on one of 2 tracks.

Because of thermal fluctuations the oscillations in magnetization can essentially follow a path similar to the multiple tracks scenario, and while there may exist a main track or primary oscillation mode, the magnetization can and will randomly jump to a adjacent oscillation mode in a phenomenon that's known as thermal hopping [57, 58] and shown in these STNO in Figure 4.6. In this case there is a primary oscillation mode in the 3.5-4.5 GHz frequency region and an auxiliary oscillation mode in the 5-6 GHz region.

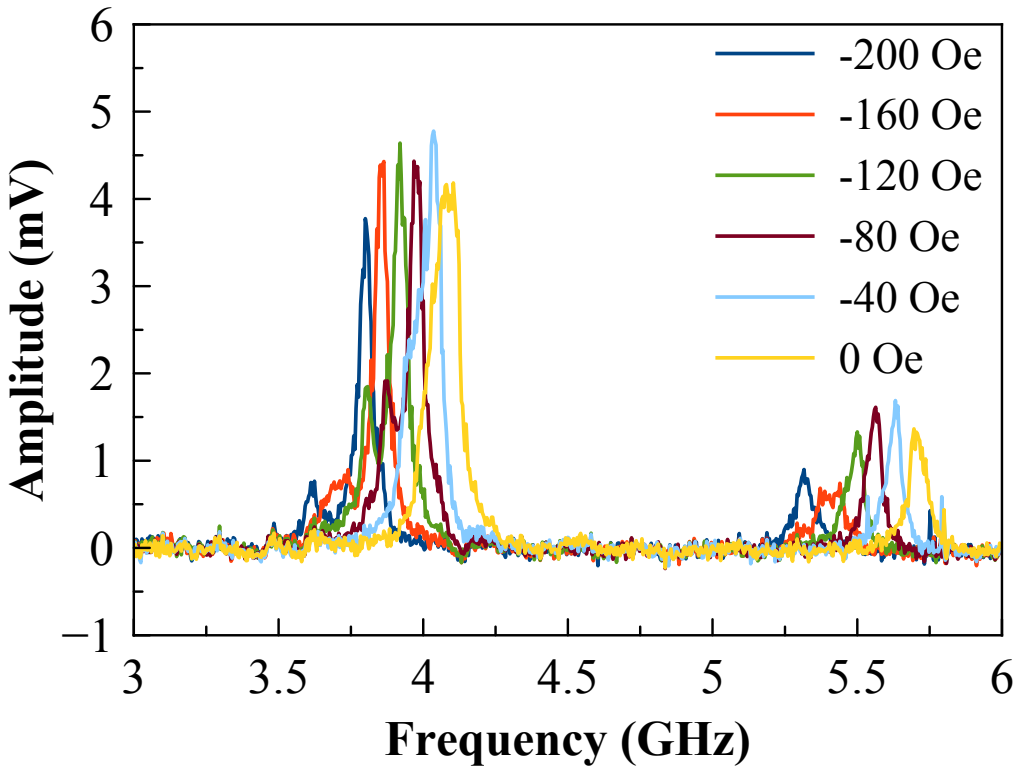

Figure 4.6 A figure illustrating the effect of thermal hopping on these STNO devices. The oscillations are hopping to a mode approximately 40% higher.

Thermal hopping itself is an interesting problem to study, however such an issue can be typically be solved using filters for a specific spectra in the event of spurious tones.

While there are some issues to this particular type of STNO, low output power typically requiring an RF power amplifier for measurement, poor Q-factor, the thermal hopping use, loss of output coherence at high current due to a breakdown in the spinwave modes and limited tunability range among other issues, it's relevant to

report that this is originally a device intended in memory application and only as an exercise in examining novel concepts was it studied as an oscillator. The fact is that this STNO is extremely small, occupying a footprint of only 110x40nm. It's a simple monolithic structure that can oscillate at microwave frequencies, an impressive feat for such a simple device.

4.4 Super Oscillator

With the disadvantages of the STNO presented in the previous section in mind. It's not difficult to think of a new type of device stack that can accommodate the type of oscillation behavior in STNO without the drawbacks of using a conventional device.

The device presented in this section is intended to be a high frequency current controlled oscillator which does not suffer from high current spectral breakdown. In order to achieve this, it will consist of an orthogonally coupled stack formed from an antiferromagnetically coupled magnetically soft oscillating layer with perpendicular magnetic anisotropy and a pinned reference layer with in plane magnetic anisotropy.

Contrary to the STNO presented in section 4.3, the design here exploits the fact that the initial state is known and magnetically pinned, such that the oscillation frequency will always increase with increasing magnitude of current.

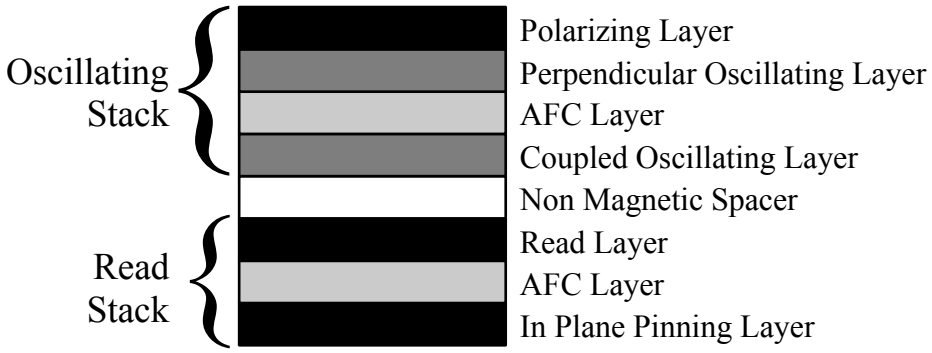

Figure 4.7 Diagram illustrating the layer stack for the STNO

The proposed STNO studied will consist of a magnetically pinned read stack separated from an oscillating stack by a non-magnetic interface layer as shown in Figure 4.7. The read stack will be magnetically pinned and have in-plane magnetic anisotropy. The magnetic layers in the oscillating stack all have perpendicular magnetic anisotropy and consists of 2 antiferromagnetically coupled oscillating layers and a current polarizing layer.

The polarizing layer is necessary to create spin polarized current in the structure, while the strong AF coupling is proposed to increases the precessional oscillation stability in the coupled oscillating layers. The read layer is pinned in the in-plane direction in order to read the output from the device without any bias field, as the projection of oscillation from the oscillating layers is in the in-plane direction.

Simulation

Using the FASTMAG micromagnetic simulation software [32], we are able to demonstrate a current tunable STNO device that capable of much higher DC current excitation than the STNO device in the section 4.3. The micromagnetic modeling, as depicted in Figure 4.8, will also confirm oscillation in the microwave regime with high output power due to a high TMR modeled in the device.

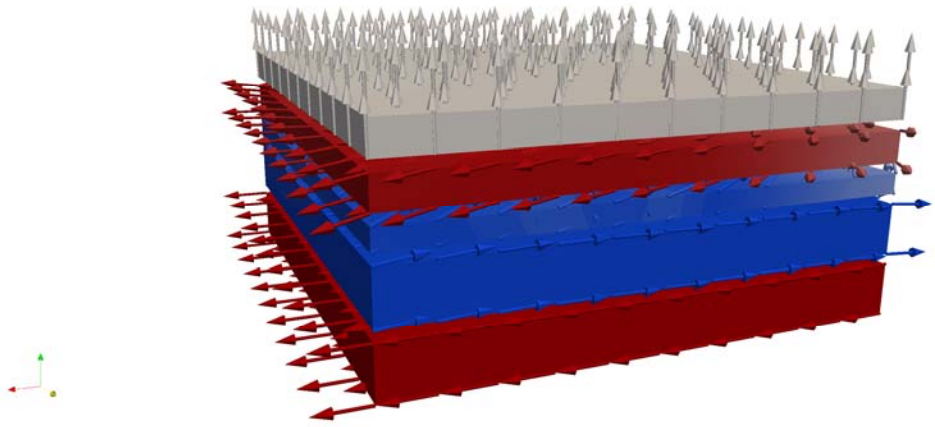

Figure 4.8 Simulation output from the FASTMAG software displaying the orientation of the magnetic layers. The arrows indicate local magnetic orientation, the red and blue color is indicative of X axis orientation while white is neutral. Current is active in this simulation frame, the perpendicular oscillating layers are in the process of precessing at high angles.

The advantage of using a highly complex micromagnetic simulator to examine the STNO devices is that there are a variety of parameters we can change as desired to affect the performance of the device, without complex fabrication development. For

the scope of this section, the work here is focused on using approximate values for known magnetic properties (Table 4.1) of common materials and alloys and to simulate with an emphasis on using different geometries to look at the dependence of RF characteristics versus change in physical shape and to identify the geometries that are ideal for oscillation. A rectangle and oval with various aspect ratios were chosen as candidate geometries they are common shapes to pattern. Several factors that we will be focusing on is the stability and linearity of the oscillator.

Table 4.1 Simulation Parameters for STNO

	Reference Layer	Oscillating Layer	Polarizing Layer
K_s (erg/cm^3)	4.0e5	4.0e6	5.0e6
M_s (emu/cm^3)	1000	800	600
Aex (erg/cm)	1.05e-6	1.05e-6	1.05e-6
α	0.02	0.02	0.02
Polarization	1.0	1.0	1.0
Exchange (erg/cm)	0.3	0.21	

A list of simulation parameters used for the FastMag micromagnetic simulation software. These parameters are derived from characterization of known materials, there is some estimation and rounding. Exchange refers to the exchange parameter of the coupled antiferromagnetic layer.

The geometries tested include a 1:1 aspect ratio square and 1:1 aspect ratio circle with one fixed dimension and one increasing dimension. The non-fixed dimension is increased in incremental amounts from a 1:1 ratio to the fixed dimension up to a 4:1

aspect ratio. The layer as are modeled as follows, starting from the bottom layer to the top polarizing layer: 5nm CoFe, 1nm Ru or Ir, 5nm CoFe, 1nm MgO, 2nm CoFeB, 1nm Ru, 3nm NiFe, 1nm Cu, 3nm CoPt. The entire stack is 22nm thick.

A multi-parametric sweep of simulation parameters is conducted to investigate the relationship between magnitude of current and oscillation behavior of the device.

An initial inspection of the simulated device shows a relationship between current and precessional frequency in circular STNO versus square STNO as shown in Figure 4.9, primarily as current is increased from 0 to 2mA, we see a general rise in the oscillation frequency of the device. An initial observation is that geometry has some effect on the fundamental frequencies that the STNO oscillates. At high current however, there is a clear divergent behavior between the circular STNO and the square STNO. In addition to this, a main issue for these devices is that an increase in current does not correspond to a linear increase in frequency, however, small sections do behave linearly in terms of the current control of oscillation. While the cause of this effect is to be determined, the effect itself is noted as variety of factors may come into play including the effects similar to the issues seen in the previous chapters (thermal hopping, breakdown of spinwave modes, spin reflected current disruption of oscillation layer similar to the nanopillar in section 2.4).

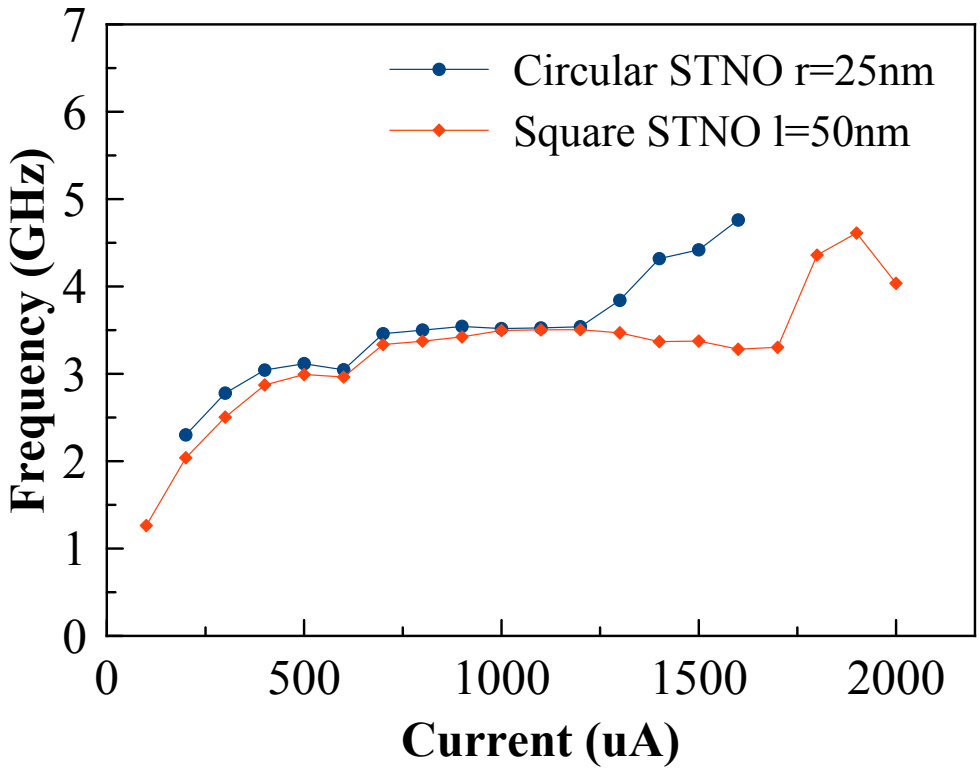

Figure 4.9 The relationship between output frequency and applied current to the STNO in a circular STNO with radius 25nm versus a square STNO with 50nm x 50nm geometry.

Figure 4.10 further illustrates the difference that shape geometry makes with STNO. Comparing the square STNO to the rectangular STNO, we see some change in oscillation behavior as a function of input current, but we also see a more stable response curve, especially with higher current, showing that the issue is not only a factor of current density.

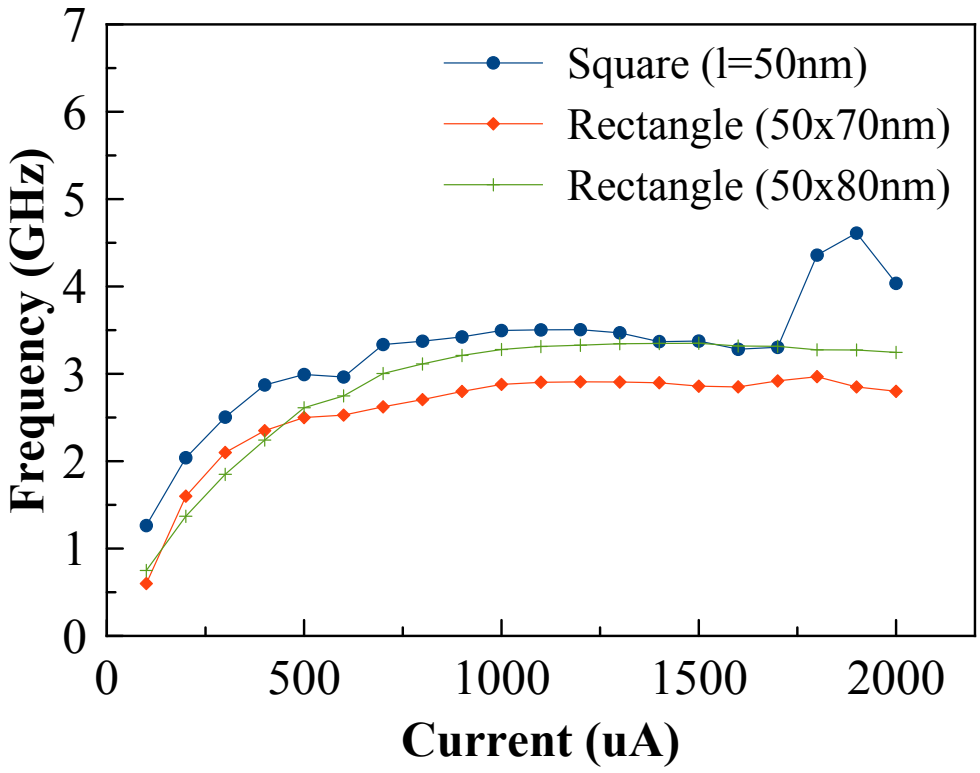

Figure 4.10 A comparison of the tunability of a square and rectangular STNO.

When we look at the oscillations in the time domain in Figure 4.11 (a)-(b) and Figure 4.12 (a)-(b), we can make some initial observations. First, is that there is approximately 10-20ns of startup before the device enters a stable precessional state as seen in Figure 4.11. Also, depending on the geometry, the quality of the oscillation can vary greatly.

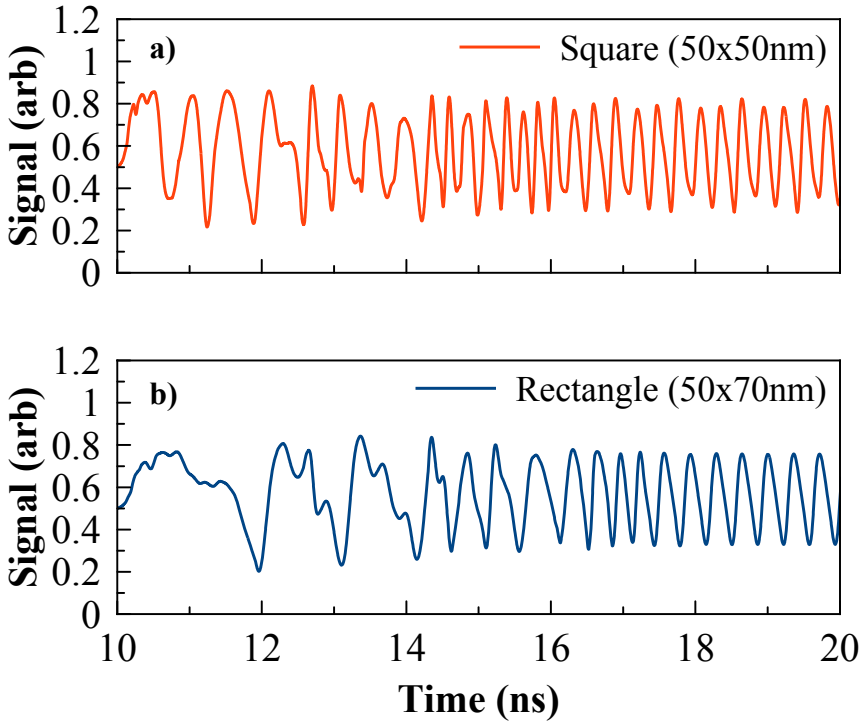

Figure 4.11 (a)-(b) Time domain output from the square and rectangular STNO, the STNO requires approximately 15 nanoseconds to stabilize for these cases.

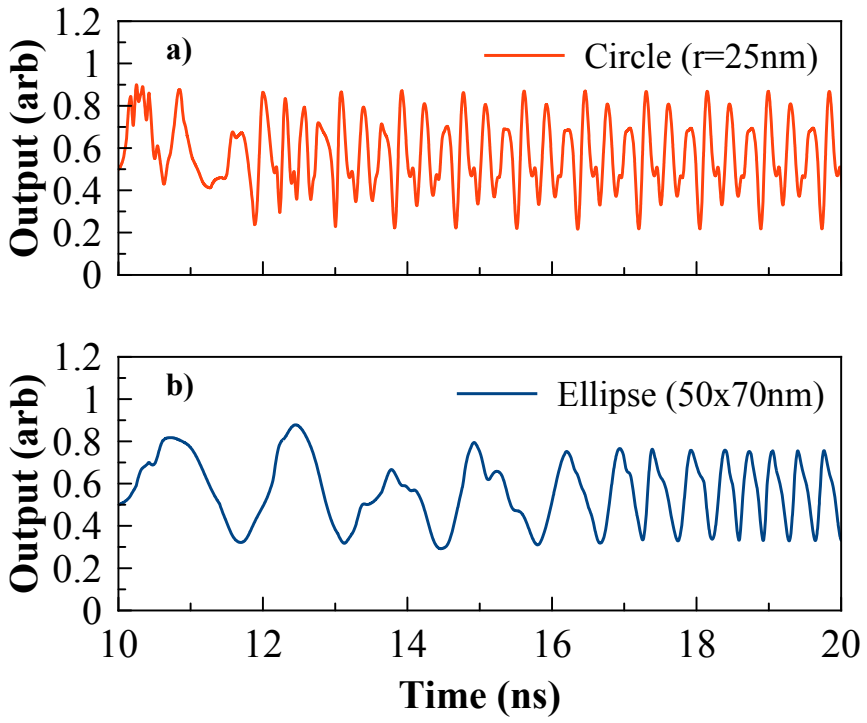

Figure 4.12 (a)-(b) Time domain output from the circular and elliptical STNO, the circular STNO requires approximately 12 ns to stabilize while the elliptical STNO requires over 18 ns.

Notably the rectangular geometries seem to have a more sine-like oscillation pattern than circular geometries. This is clear when you compare Figure 4.11 (b) and Figure 4.12 (b), the rectangle and elliptical STNO. The ellipse has a more saw tooth-like pattern with a very subtle judder whereas the rectangular geometry has a smoother curve. Ironically it is the geometrically squarer device that has a smoother curve. The square and circular STNO in Figure 4.11 (a) and Figure 4.12 (a) both have a multimode signal compared to the rectangular and elliptical STNO as shown by the

uneven output level.

Both geometries indicate that an elongated pattern has better performance using this STNO design scheme. The oscillation quality benefits greatly from a slightly elongated aspect ratio as demonstrated in Figure 4.11 and Figure 4.12, however once the geometry is set past a certain aspect ratio (approximately 2:1), there are dramatically different and poorer results, notably as the aspect ratio increases past this 2:1 ratio as shown in Figure 4.13, the output power decreases significantly, as much as only half the output power compared to nominal results. For the layer stack described above, an aspect ratio of greater than 1:1 and less than 2:1 was found to have the best performance over other sizes.

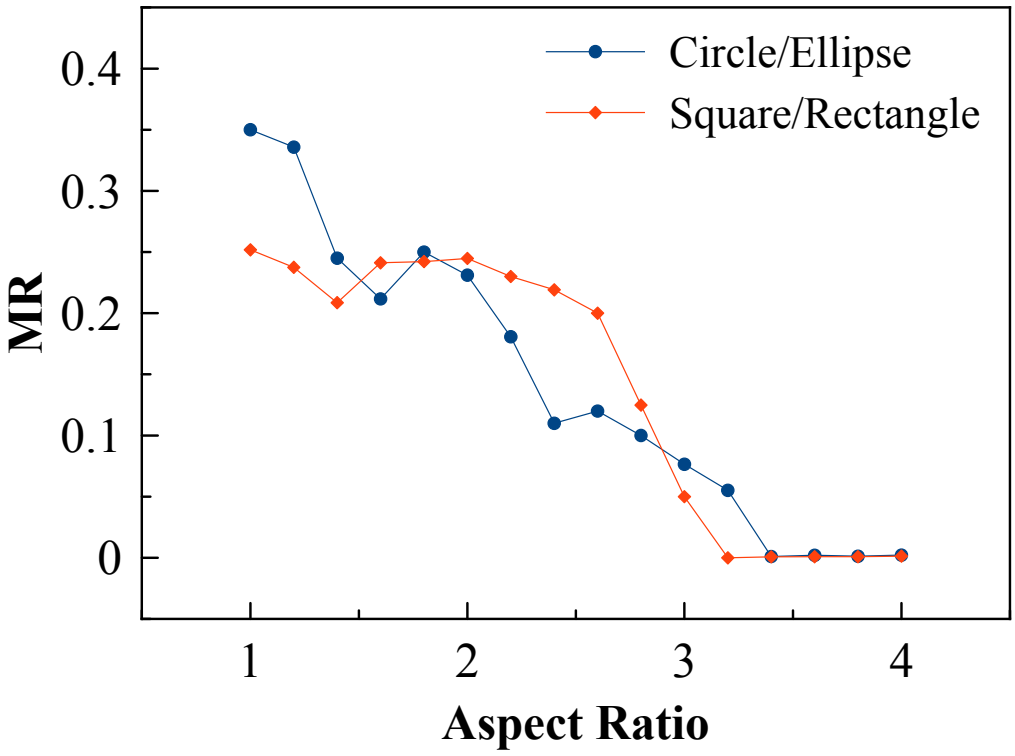

Figure 4.13 The MR output for the elliptical and rectangular STNO. As the aspect ratio is stretched out, the device requires higher current density to oscillate. A 1.0 aspect ratio represents a square or circle, higher aspect ratios represent more elongated rectangles and ellipses.

By examining the total harmonic distortion of the signal in the frequency spectrum (Figure 4.14 & Figure 4.15), we are able to quickly look at the linearity of the oscillator and identify how ideal the oscillations are.

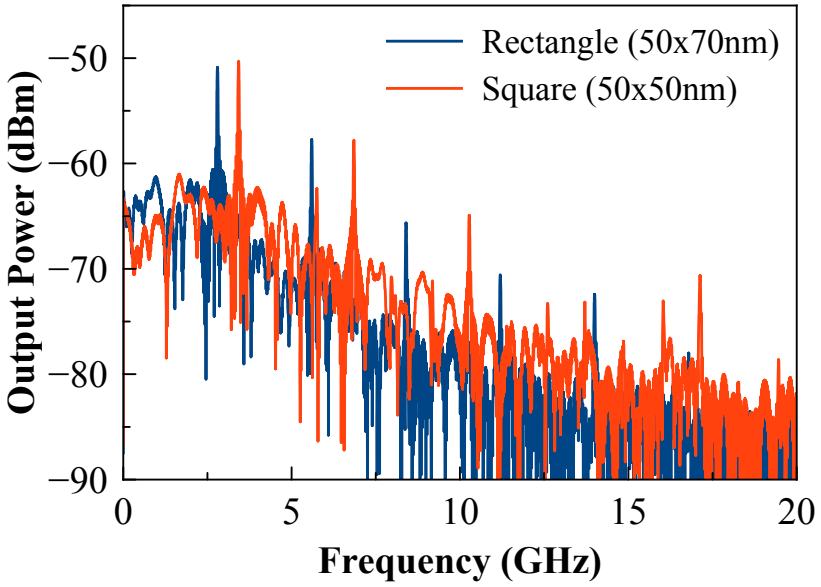

Figure 4.14 Spectral output from simulated rectangular and square STNO.

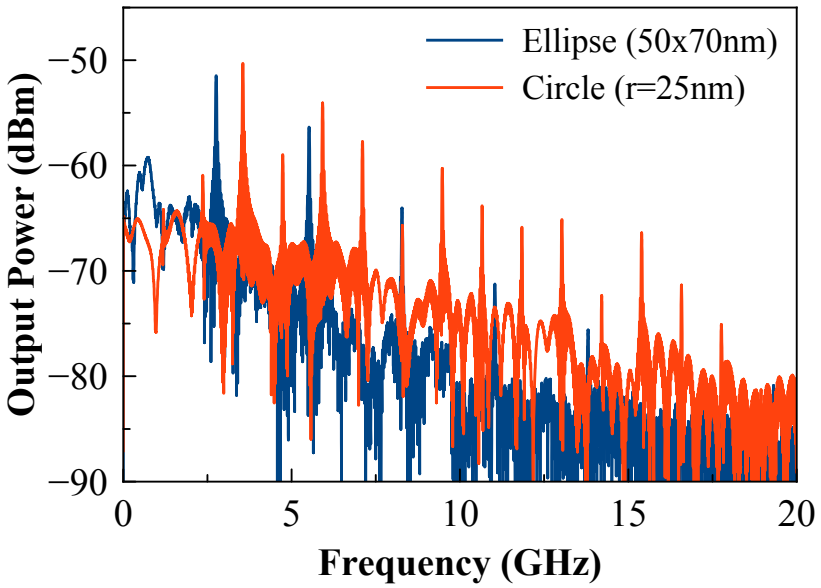

Figure 4.15 Spectral output from simulated elliptical and circular STNO.

Past the 2:1 aspect ratio for both the rectangular and elliptical aspect ratios, we

start to see poor performance dominating in this respect as shown in Figure 4.16, along with the previous results we can conclude that too skewed of an aspect ratio is detrimental for oscillation performance in STNO.

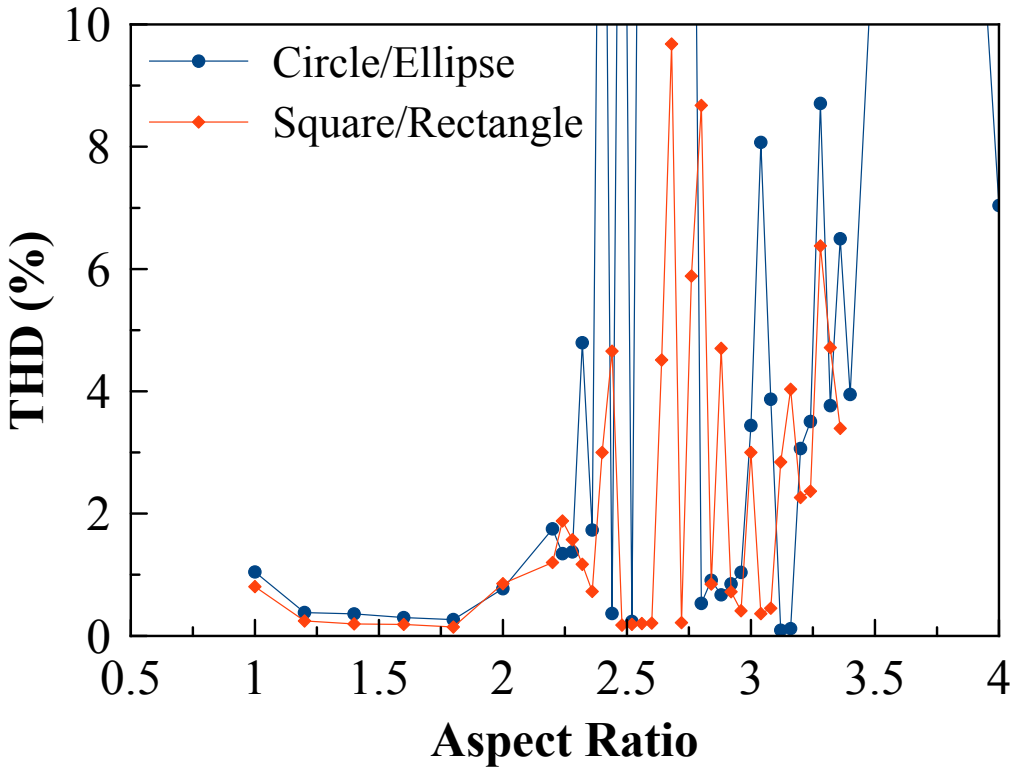

Figure 4.16 The THD for the STNO over several aspect ratios Notably past an aspect ratio of 2 there is a significant increase in the instability of the STNO with regards to the amount of noise.

There are a variety of factors that are candidate to influence the performance of the STNO as geometry changes. There is a change in the anisotropy, the magnetic volume increases, and there is an overall affect on the magnetic dynamics. Geometry

can also has a noticeable effect on output frequency behavior.

To summarize the preliminary findings from these simulations, first a very important difference between the rectangular and elliptical geometries is that the square is more sine-like in terms of time domain output. With small devices we see slightly higher frequencies, but with larger devices we see better stability and tunability. However, when we have too large a device, we see a definite decrease in performance for these STNO.

Chapter 5: Ferromagnetic Resonance

5.1 Introduction

Ferromagnetic resonance (FMR) is a phenomenon that occurs in ferromagnetic materials in the presence of an external magnetic field. Upon further review of the LLG equation (Equation 1.2), we understand that the external field will torque the magnetization of a ferromagnet causing it to precess. The discovery of the ferromagnetic effect was made by Griffiths [59] and further theorized by Kittel [60]. By utilizing modern measurement tools, we are able to characterize the gyromagnetic ratio [61], magnetic anisotropy [62] and damping [63] properties of both bulk and thin films by using spectroscopy.

When a magnetic field is applied on some ferromagnetic material the magnetization will tend to line up parallel to the field due to the torque applied to the moment. With the initial assumption that there is no damping torque and with an orthogonal RF field applied to our material as shown in Figure 5.1.

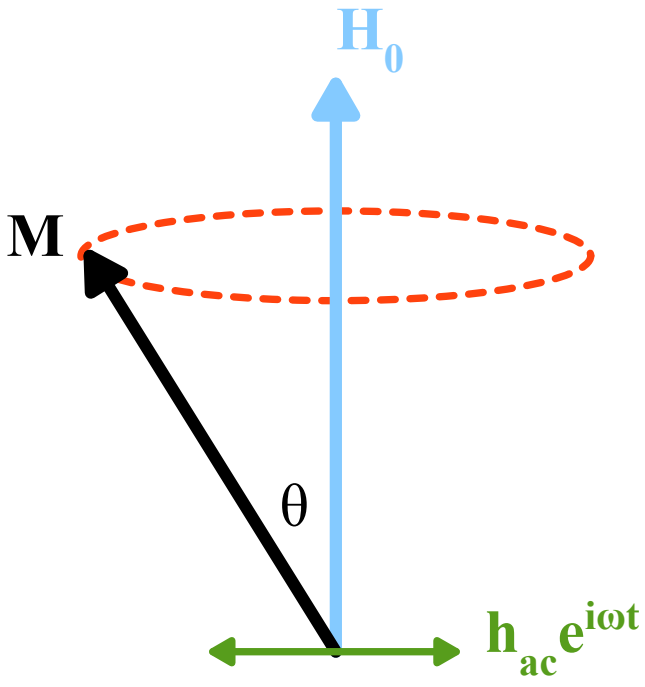

Figure 5.1 A simplified diagram of the fields on single magnetic moment during ferromagnetic resonance. The blue represents some form of unchanging magnetic field whereas the green vector represents an RF field.

The relationship is shown by the precessional term from the LLG equation in Equation 5.1. Where γ is the gyromagnetic ratio, M is the magnetization vector and H is the total magnetic field vector.

$$\frac{1}{\gamma}\frac{d\mathbf{M}}{dt} = -\mathbf{M} \times \mathbf{H}$$

Equation 5.1

After including both complex terms from the addition of the small signal field

$\mathbf{H} = \mathbf{H}_0 \hat{z} + h_{ac} e^{i\omega t} \hat{x}$ and $\mathbf{M} = \mathbf{M}_0 \hat{z} + \vec{m} e^{i\omega t}$ into the equation, and with the assumption of small angle precession, we linearize the LLG equation to obtain Equation 5.2 allowing us to solve for our resonant frequency in Equation 5.3 where ω is the angular frequency.

$$i\omega \vec{m} e^{i\omega t} = \gamma(\mathbf{M}_0 \hat{z} + \vec{m} e^{i\omega t}) \times (\mathbf{H}_0 \hat{z} + h_{ac} e^{i\omega t} \hat{x})$$

Equation 5.2

$$\omega_{res} = \gamma \mathbf{H}_0$$

Equation 5.3

To fully describe the behavior of this system, we must also consider the damping term, when the finite damping (α) is added (Equation 5.4), we can solve for the complex susceptibility and see that it will change as a function of damping, specifically that the peaks in these curves will widen as damping increases. We can also see how each term will directly affect the complex susceptibility [64] from Equation 5.5. Specifically we see that damping has no impact on the resonant frequency, but does has an impact on linewidth as visualized with the magnitude of the complex susceptibility in Figure 5.2

$$\left((\gamma \mathbf{H}_0 + i\alpha\omega)^2 - \omega^2\right) m_x = \gamma \mathbf{M}_0 (\gamma \mathbf{H}_0 + i\alpha\omega) h_x$$

Equation 5.4

$$\Re(\chi) = 1 + \frac{\gamma \mathbf{M}_0 \gamma \mathbf{H}_0 \left((\gamma \mathbf{H}_0)^2 - \omega^2 (1 - \alpha^2) \right)}{\left((\gamma \mathbf{H}_0)^2 - \omega^2 (1 - \alpha^2) \right)^2 + (2\alpha\omega\gamma \mathbf{H}_0)^2}$$

$$\Im(\chi) = \frac{\alpha\omega\gamma \mathbf{M}_0 \left((\gamma \mathbf{H}_0)^2 + \omega^2 (1 - \alpha^2) \right)}{\left((\gamma \mathbf{H}_0)^2 - \omega^2 (1 - \alpha^2) \right)^2 + (2\alpha\omega\gamma \mathbf{H}_0)^2}$$

Equation 5.5

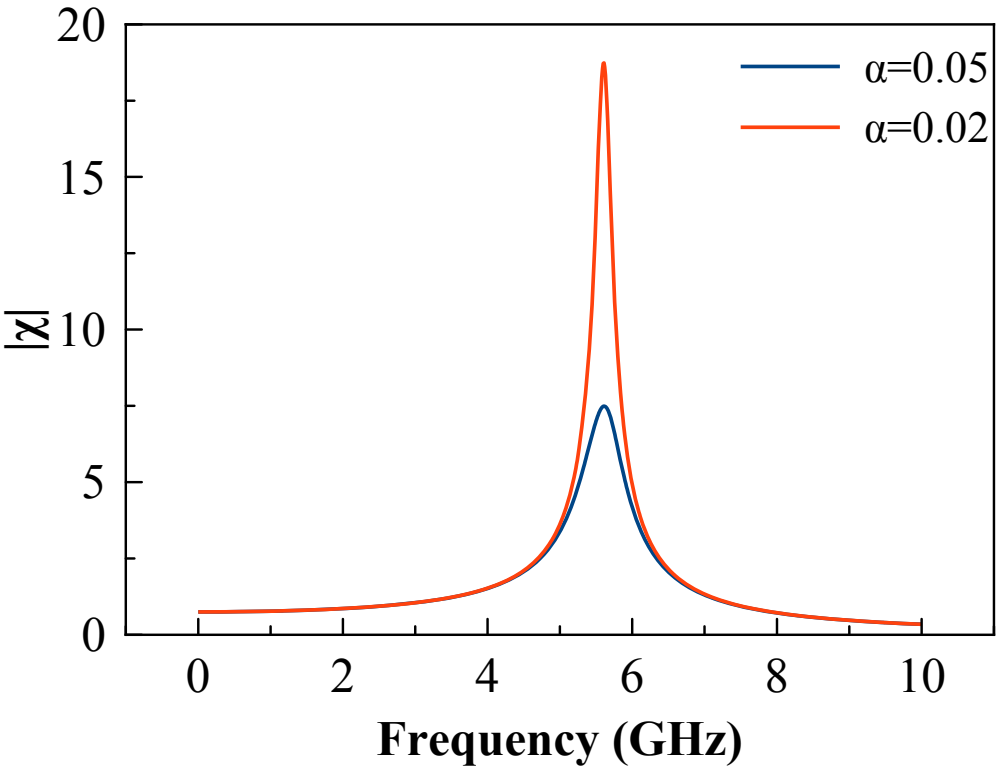

Figure 5.2 A comparison of complex susceptibility with two different damping values. The position of the peak does not move, however, the linewidth of the peak changes. M = 150mT and H = 200mT resulting in a resonant frequency of approximately 5.6 GHz.

For the samples we will be studying, ferromagnetic thin films, the resonance frequency, as a function when we expand H_{eff} will be given by Equation 5.6 for

perpendicular to plane anisotropy films.

$$f_{res} = \frac{\gamma}{2\pi}\left(H_0 + H_k - H_D\right)$$

Equation 5.6

All FMR measurements presented in this chapter will be from perpendicular magnetic anisotropy devices. Using a method similar to Bilzer [65], we will use a 2 port vector network analyzer (VNA) and place the device on top of a coplanar waveguide (CPW). The waveguide will both be a source of RF magnetic field and detector to measure sample susceptibility. Specifically we measure a discreet series of RF frequencies supplied by the VNA and sweep magnetic field using an external electromagnet to find the resonant peaks. Using Equation 5.6 for a series of resonant peaks, we can determine both H_{k_eff} and extract the damping parameter using Equation 5.7 using the relationship between damping and peak linewidth [66], where ΔH are the linewidths of the resonant peaks.

$$\Delta H = \Delta H_0 + \frac{4\pi\alpha}{\gamma} f_{res}$$

Equation 5.7

5.2 Coplanar Waveguide Design and FMR Considerations

The CPW plays a critical role in the FMR detection system as it's the sensing element to measure device susceptibility and to also provide the RF magnetic field. We initially fabricated and measured a variety of CPW using various gap sizes, impedances, and configurations. While the basic conclusion is that we can theoretically obtain FMR measurements from any reasonable CPW, as a matter of optimization we looked for a CPW configuration that could provide an optimal FMR signal that can support a broad band of frequencies from the VNA with minimum noise, low attenuation, and maximum S-parameter transmission.

The system level consideration is that we need to match high frequency components, cables and connectors, and an appropriate vector network analyzer to realize a fully capable FMR measurement system. As frequency requirements increase, component cost increases as well, and prohibitively so. With that in mind our system is designed for 0-20 GHz, limited by the cables and VNA, whereas the CPW and connectors are capable of up to 65 GHz to allow room for future upgrades.

Two types of CPW were chosen for testing, short and transmission. A DOE was developed to determine an optimal CPW configuration, using variables of gap width, trace width, CPW impedance and CPW length, the DOE is summarized in Table 5.1.

The waveguides are 1oz copper patterned on FR-4 boards.

Table 5.1 A summary of CPW tested for FMR measurements

Name	Gap (μm)	Trace Width (μm)	Impedance	Length (cm)	Type
W1	32	50	70	1	Transmission
W2	32	100	60	1	Transmission
W3	32	200	50	1	Transmission
W4	32	200	50	0.5	Short
W5	32	100	60	0.5	Short
W6	32	50	70	0.5	Short
W7	32	32	79	1	Transmission
W8	50	32	92	1	Transmission
W9	100	32	115	1	Transmission
W10	32	50	70	1	Short
W11	32	100	60	1	Short
W12	32	200	50	1	Short

In the case of a 0.5cm short CPW and a 1cm transmission CPW, we see the general trend of maximum signal with thinner trace widths and wider gaps as shown by the results in Figure 5.3 and Figure 5.4. These measurements were conducted all with a single 3nm sample of CoFeB.

Additionally as evidenced by the resonant peak results in Figure 5.5 and the resonant peak linewidths in Figure 5.6, despite the amount of variation in the waveguides tested, there is no effect on detection itself, however an optimal waveguide will provide a much better signal to noise ratio. Using the parameter extraction

method from the previous section we can estimate an H_{k_eff} of 8300 Oe and damping of 0.008.

Another study was performed comparing the performance of GaAs substrate CPW and FR-4 substrate CPW, while the GaAs substrate performed better (Figure 5.7), returning a stronger signal, the material is quite fragile and deemed unsuitable for the type of characterization work for the remainder of the study.

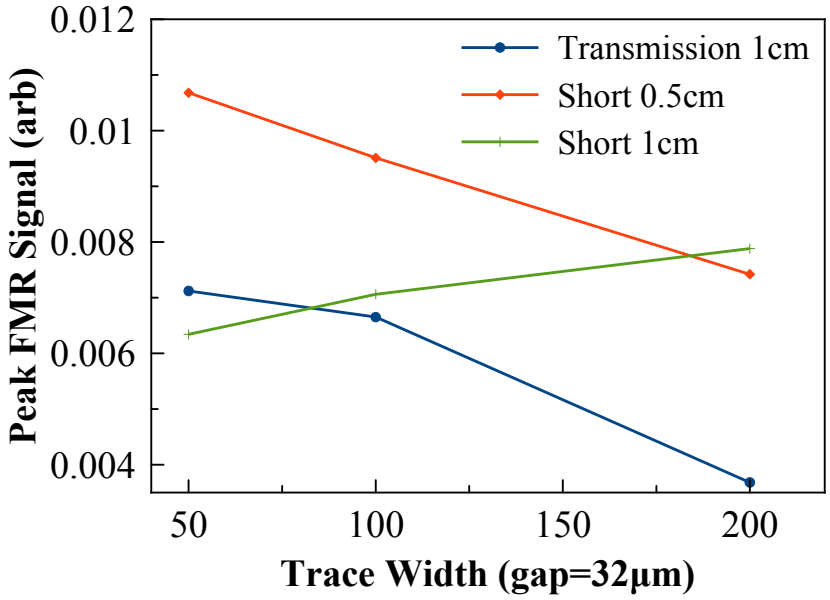

Figure 5.3 Peak FMR signal as a function of trace width and a fixed gap of 32 μm.

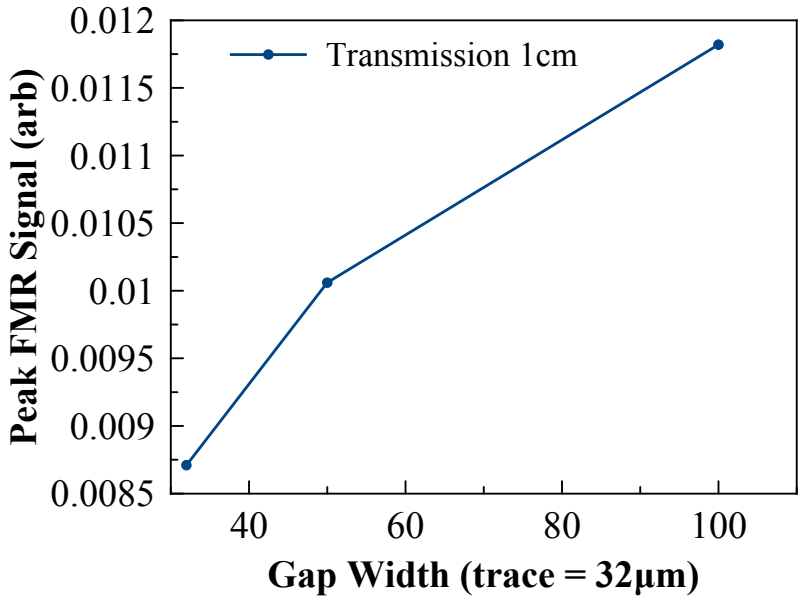

Figure 5.4 Peak FMR signal as a function of gap width and a fix trace width of 32 μm.

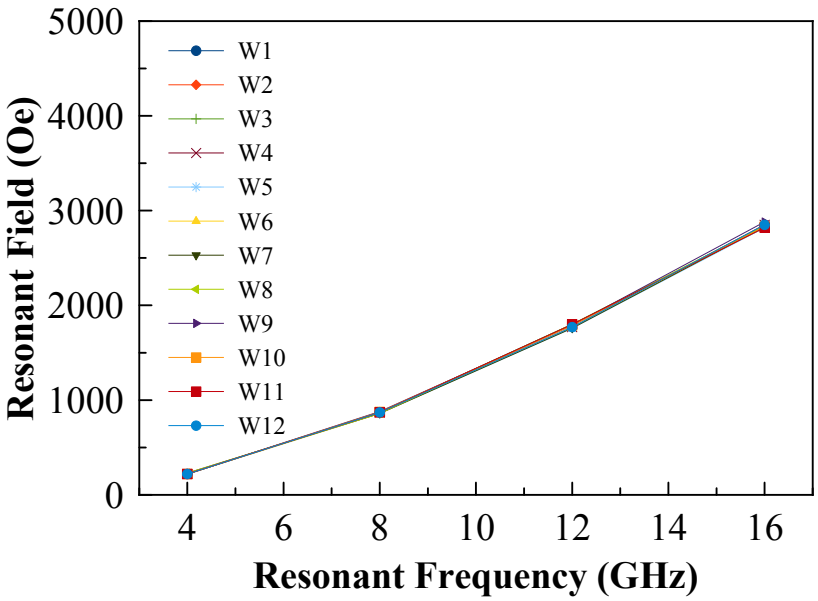

Figure 5.5 The resonant frequency of all 12 waveguides with very little variation in resonant frequency.

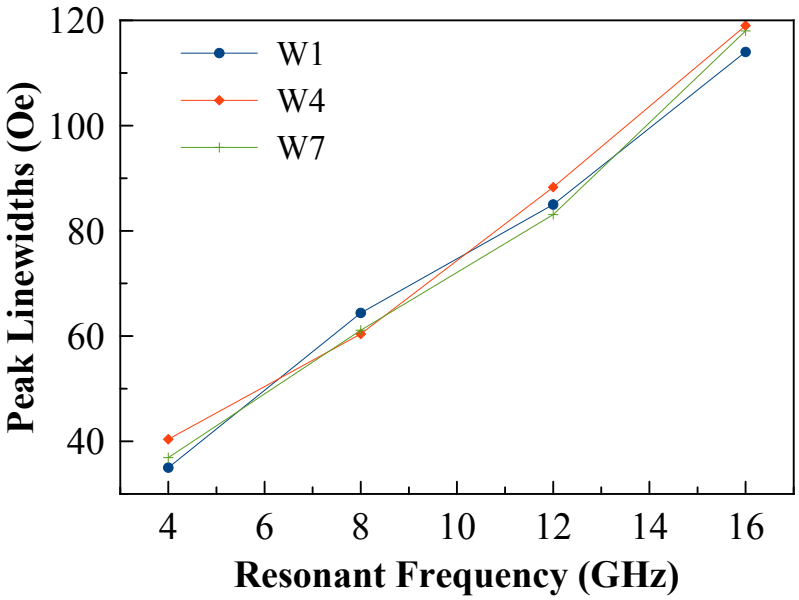

Figure 5.6 The resonant peak linewidths as a function of resonant frequency.

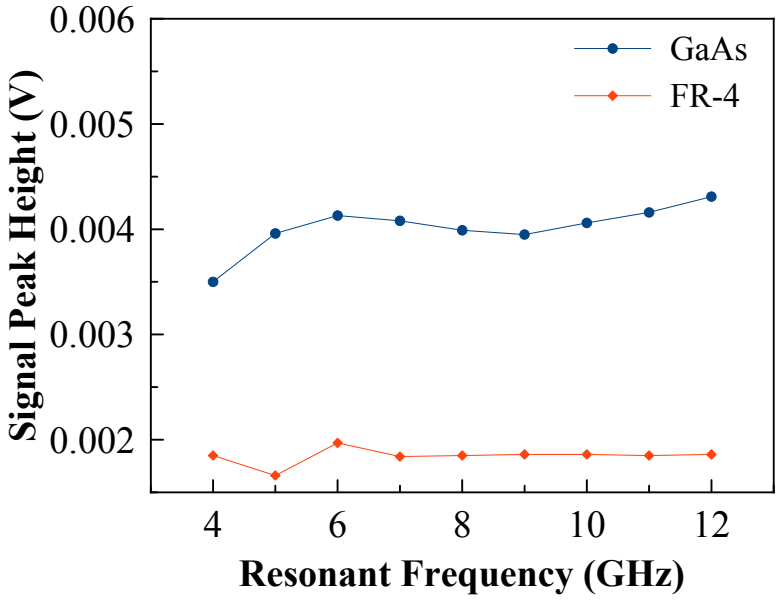

Figure 5.7 A comparison of resonant signal peak height between a GaAs substrate and FR-4 substrate.

We can the characterization study from these results to select an ideal CPW most suited to our measurements. By balancing parameter extraction and durability, we have chosen FR-4 with a thin trace width and large gap despite the lower signal peaks compared to GaAs and the impedance mismatch, we have a strong durable CPW which still allows us to perform sensitive characterization measurements.

5.3 Ferromagnetic Parameter Extraction

FMR can be used to extract parameters such as H_{k_eff}, damping (α), and the gyromagnetic ratio simply by solving **Error! Reference source not found.** or Equation 5.6 for H_{k_eff} and damping and Equation 5.7. What's needed is a list of resonant frequencies and corresponding resonant magnetic fields. In practice, whether you fix field and sweep frequency for S-parameter measurements or set a frequency and sweep field while measuring S-parameters, doesn't make a difference. However in practice, for perpendicular magnetic anisotropy samples, it's easiest to set your VNA to your intended resonant frequency and sweep field. All proceeding measurements presented in this chapter are studies of perpendicular magnetic anisotropy samples and measured in this fashion.

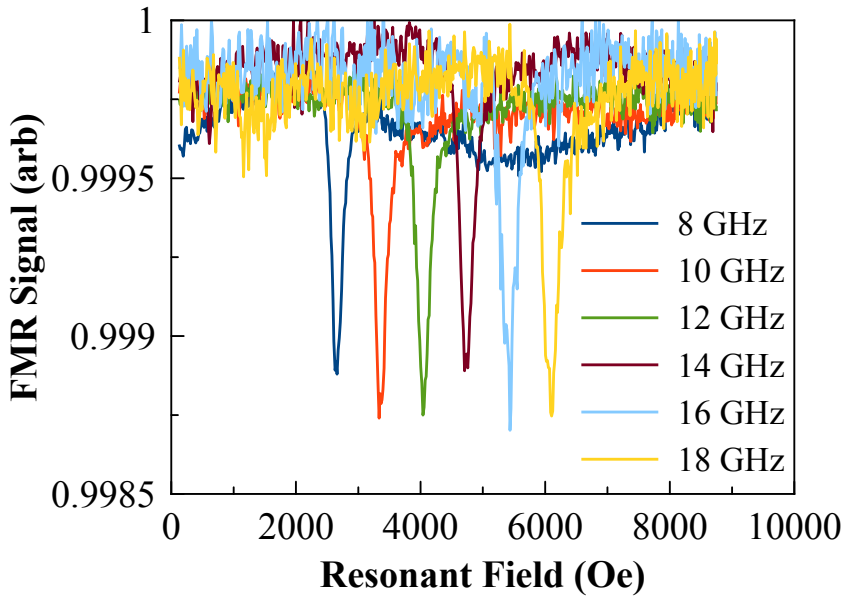

Figure 5.8 A sample of some FMR resonant peaks from 1.2nm CoFeAl film.

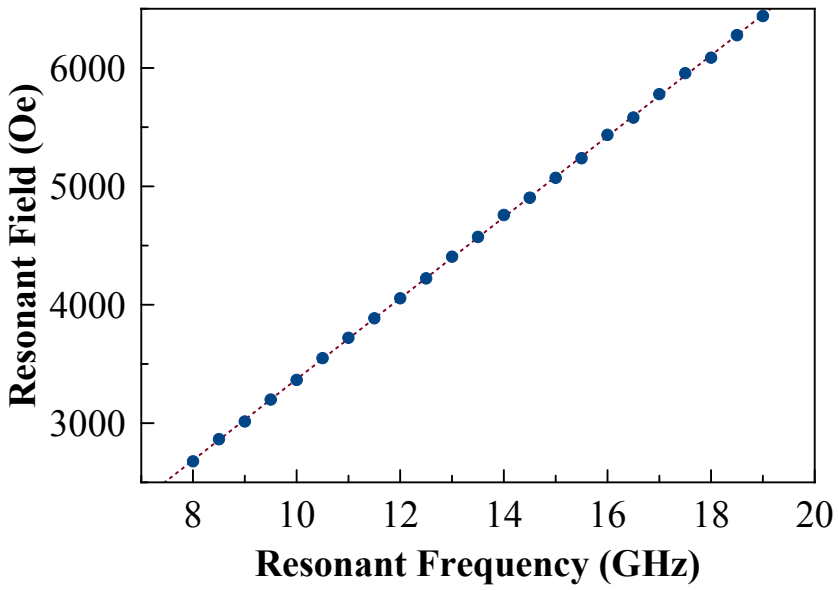

Figure 5.9 Results of an FMR study on 1.2nm CoFeAl film showing the resonant field as a function of frequency.

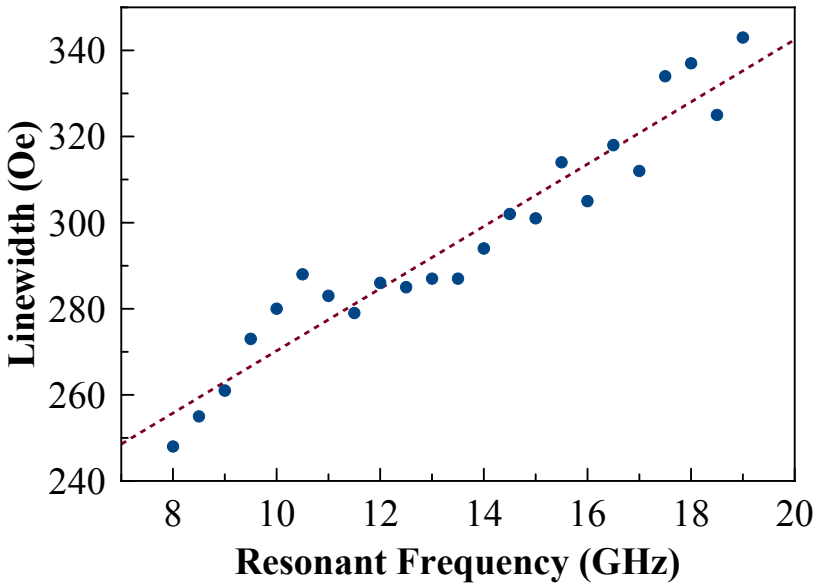

Figure 5.10 The linewidths as a function of frequency. These are the direct measured linewidths.

By measuring the FMR response of a 1.2 nm thick sample of CoFeAl with perpendicular magnetic anisotropy (Figure 5.8), we can assemble the resonant data as shown in Figure 5.9 and Figure 5.10. By extracting the parameters we find that we have an Hk_eff of approximately 50 Oe, a $\gamma/2\pi$ of 0.0029 GHz/G and damping of 0.0093.

5.4 Temperature Dependent Ferromagnetic Resonance

With the initial goal of using FMR to characterize films, it was our intention to build a tool to perform FMR characterization as a function of temperature, specifically to extract H_{k_eff} and damping parameters. A characterization study over temperature

will allow us to understand how device physics such as switching dynamics and energy barrier evolve under changing temperatures, allowing us to predict critical switching behavior and thermal stability.

We designed a Temperature-Dependent Ferromagnetic Resonance (T-FMR) probe using a 2-port transmission waveguide shown in Figure 5.11. The mini-SMP connectors and waveguide are capable of up to 65-GHz. The cables shown are rated for operation up to 18 GHz.

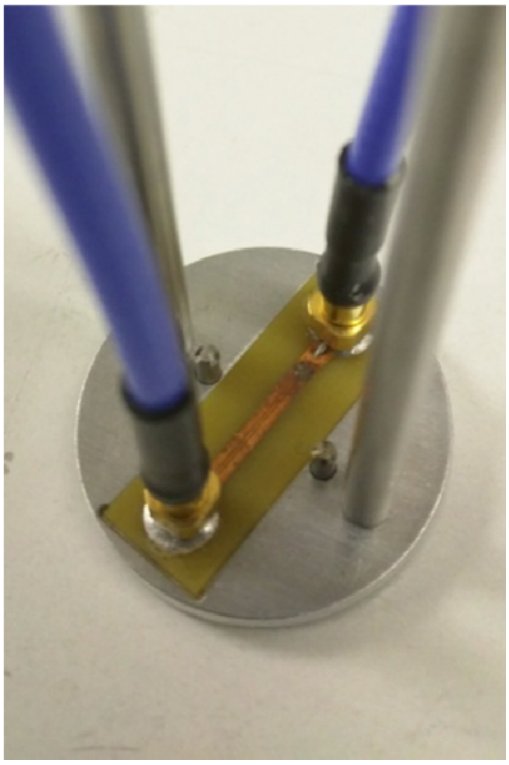

Figure 5.11 The T-FMR waveguide assembly, a copper CPW on FR-4 substrate with mini-SMP connectors.

The T-FMR probe is inserted into a cryostat magnet (PPMS, Figure 5.12), with the waveguide located at the base of the probe. As a system, the PPMS can output a magnetic field of +/0-9 Tesla and temperatures of 2-400 Kelvin. The sample is placed film-side down on top of the CPW while situated inside the PPMS.

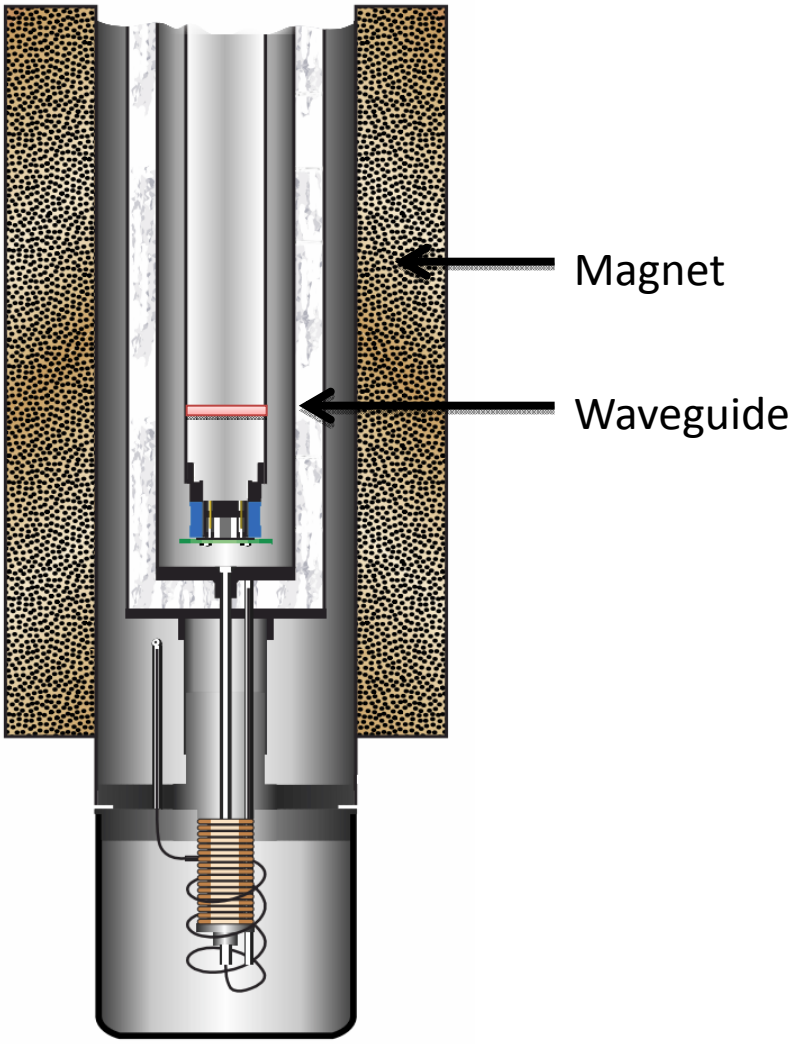

Figure 5.12 A diagram of the waveguide in relation to the cryostat magnet when inserted into the system.

In order to perform the temperature characterization, we need to run full characterization studies identical to those in section 5.3 at multiple temperature intervals with some expectation that we can develop some level of prediction for films for high temperature and as a function of film thickness. For our characterization study, we've chosen a stack with 2 CoFeB layers separated by a 2nm Ta layer and sandwiched by 2 layers of MgO, the free layer of an MTJ sample.

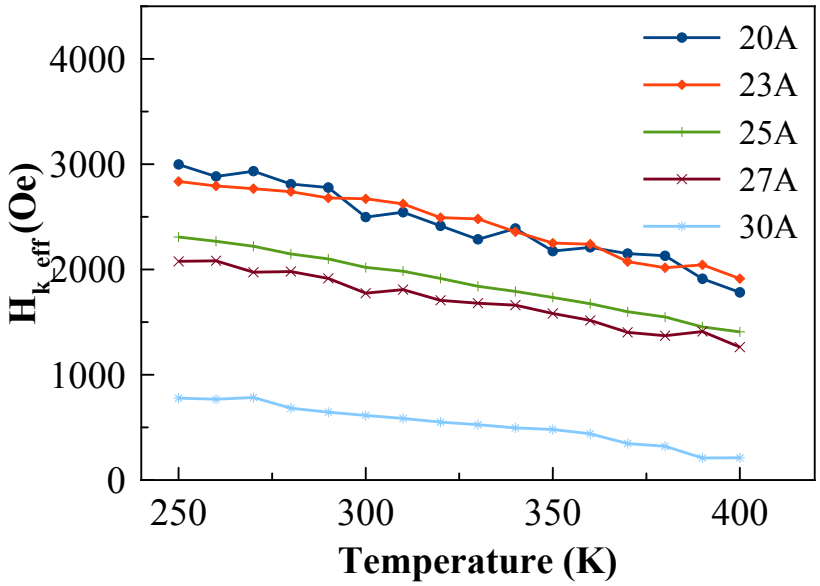

Figure 5.13 H_{k_eff} as a function of temperature as measured by T-FMR for various thicknesses of MTJ free layer.

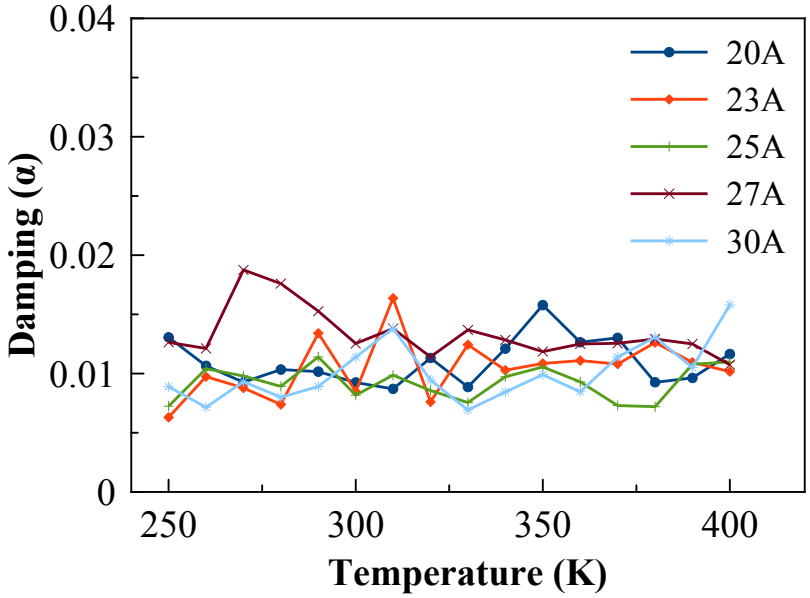

Figure 5.14 Damping as a function of temperature as measured by T-FMR for various thicknesses of MTJ free layer. In this temperature range damping is not expected to change much.

The measurements reveal a linear trend in Hk_eff versus temperature (Figure 5.13) and a relative unchanging damping parameter (Figure 5.14) under the expected operating range of temperatures. While the 20-27 angstrom thick free layer samples have relatively strong perpendicular magnetic anisotropy, the 30 angstrom thick sample has fairly weak PMA. However the thinner layers have a larger variance on H_{k_eff} as temperature changes, the thinnest layer (20Å) has twice the rate of change in H_{k_eff} per change in temperature as the thickest layer (30Å) . However, since H^{k_eff} at T=0K is lowest for the thick films (Figure 5.16), the thinner films have only ~65% change in H_{k_eff} between 250K and 400K, but the 30Å film has a ~270% change.

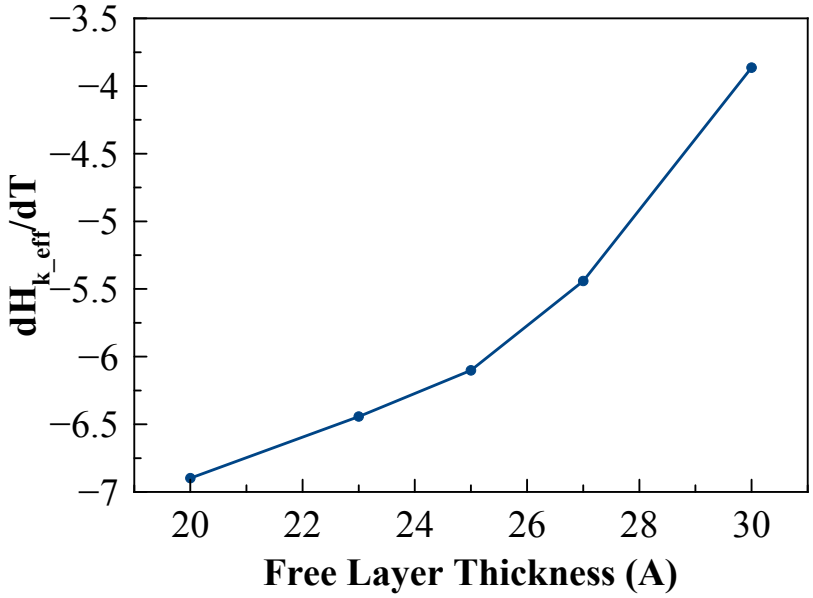

Figure 5.15 The rate of change of H_{k_eff} versus Temperature for various free layer thicknesses.

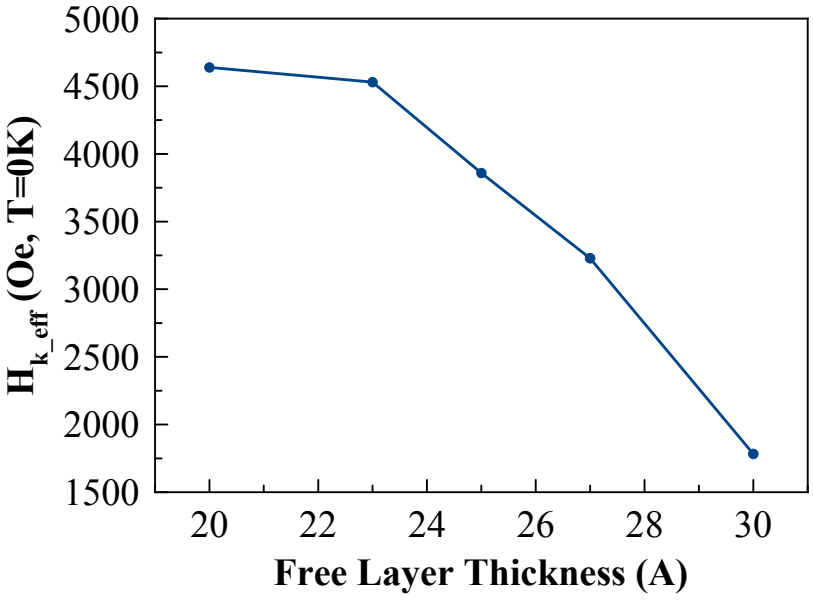

Figure 5.16 The change in H_{k_eff} estimated at 0 temperature for various thicknesses of MTJ free layer.

As a tool the TFMR probe can successfully extract meaningful characterization parameters such as effective anisotropy and damping parameters. The probe itself is compatible with a wide range of magnetic field and temperature and is upgradeable for future improvement.

References

[1] M. N. Baibich, J. M. Broto, A. Fert, F. N. Van Dau, F. Petroff, P. Etienne, G. Creuzet, A. Friederich, and J. Chazelas, "Giant magnetoresistance of (001) Fe/(001) Cr magnetic superlattices," *Physical review letters,* vol. 61, p. 2472, 1988.

[2] G. Binasch, P. Grünberg, F. Saurenbach, and W. Zinn, "Enhanced magnetoresistance in layered magnetic structures with antiferromagnetic interlayer exchange," *Physical review B,* vol. 39, p. 4828, 1989.

[3] D. A. Thompson and J. S. Best, "The future of magnetic data storage techology," *IBM Journal of Research and Development,* vol. 44, pp. 311-322, 2000.

[4] S. Mao, Y. Chen, F. Liu, X. Chen, B. Xu, P. Lu, M. Patwari, H. Xi, C. Chang, and B. Miller, "Commercial TMR heads for hard disk drives: characterization and extendibility at 300 gbit/in 2," *IEEE transactions on magnetics,* vol. 42, pp. 97-102, 2006.

[5] E. E. Fullerton and J. R. Childress, "Spintronics, Magnetoresistive Heads, and the Emergence of the Digital World," *Proceedings of the IEEE,* vol. 104, pp. 1787-1795, 2016.

[6] S. S. Parkin, C. Kaiser, A. Panchula, P. M. Rice, B. Hughes, M. Samant, and S.-H. Yang, "Giant tunnelling magnetoresistance at room temperature with MgO (100) tunnel barriers," *Nature materials,* vol. 3, pp. 862-867, 2004.

[7] Y. Zhou, J. Xiao, G. E. Bauer, and F. Zhang, "Field-free synthetic-ferromagnet spin torque oscillator," *Physical Review B,* vol. 87, p. 020409, 2013.

[8] W. Rippard, M. Pufall, S. Kaka, S. Russek, and T. Silva, "Direct-Current Induced Dynamics in C o 90 F e 10/N i 80 F e 20 Point Contacts," *Physical Review Letters,* vol. 92, p. 027201, 2004.

[9] C. Chappert, A. Fert, and F. N. Van Dau, "The emergence of spin electronics in data storage," *Nature materials,* vol. 6, pp. 813-823, 2007.

[10] J. Katine and E. E. Fullerton, "Device implications of spin-transfer torques," *Journal of Magnetism and Magnetic Materials,* vol. 320, pp. 1217-1226, 2008.

[11] J. C. Slonczewski, "Current-driven excitation of magnetic multilayers," *Journal of Magnetism and Magnetic Materials,* vol. 159, pp. L1-L7, 1996.

[12] M. Johnson, P. Bloemen, F. Den Broeder, and J. De Vries, "Magnetic anisotropy in metallic multilayers," *Reports on Progress in Physics,* vol. 59, p. 1409, 1996.

[13] B. Voigtländer, G. Meyer, and N. M. Amer, "Epitaxial growth of thin magnetic cobalt films on Au (111) studied by scanning tunneling microscopy," *Physical Review B,* vol. 44, p. 10354, 1991.

[14] J. A. Katine and E. E. Fullerton, "Device implications of spin-transfer torques," *Journal of Magnetism and Magnetic Materials,* vol. 320, pp. 1217-1226, Apr 2008.

[15] T. Miyazaki and N. Tezuka, "Giant Magnetic Tunneling Effect in Fe/Al2o3/Fe Junction," *Journal of Magnetism and Magnetic Materials,* vol. 139, pp. L231-L234, Jan 1995.

[16] P. M. Levy, S. F. Zhang, and A. Fert, "Electrical-Conductivity of Magnetic Multilayered Structures," *Physical Review Letters,* vol. 65, pp. 1643-1646, Sep 24 1990.

[17] S. Parkin, K. Roche, M. Samant, P. Rice, R. Beyers, R. Scheuerlein, E. O'sullivan, S. Brown, J. Bucchigano, and D. Abraham, "Exchange-biased magnetic tunnel junctions and application to nonvolatile magnetic random access memory," *Journal of Applied Physics,* vol. 85, pp. 5828-5833, 1999.

[18] R. Choi, J. Katine, S. Mangin, and E. Fullerton, "Current-induced Pinwheel Oscillations in Perpendicular Magnetic Anisotropy Spin Valve Nanopillars," *IEEE Transactions on Magnetics,* vol. 52, pp. 1-5, October 2016.

[19] V. E. Demidov, S. Urazhdin, H. Ulrichs, V. Tiberkevich, A. Slavin, D. Baither, G. Schmitz, and S. O. Demokritov, "Magnetic nano-oscillator driven by pure spin current," *Nature materials,* vol. 11, pp. 1028-1031, 2012.

[20] R. Choi, J. J. Kan, S. H. Kang, and E. E. Fullerton, "Demonstration of a Highly Tunable Hybrid nMOS-Magnetic-Tunnel-Junction Ring Oscillator," *IEEE Transactions on Electron Devices,* vol. 63, pp. 1768-1773, 2016.

[21] J. Almeida, P. Wisniowski, and P. Freitas, "Field detection in single and double barrier MgO magnetic tunnel junction sensors," *Journal of Applied Physics,* vol. 103, 2008.

[22] A. Tulapurkar, Y. Suzuki, A. Fukushima, H. Kubota, H. Maehara, K. Tsunekawa, D. Djayaprawira, N. Watanabe, and S. Yuasa, "Spin-torque diode effect in magnetic tunnel junctions," *Nature,* vol. 438, pp. 339-342, 2005.

[23] M. Stiles and A. Zangwill, "Anatomy of spin-transfer torque," *Physical Review B,* vol. 66, p. 014407, 2002.

[24] I. Tudosa, J. Katine, S. Mangin, and E. E. Fullerton, "Current Induced Switching of the Hard Layer in Perpendicular Magnetic Nanopillars," *Magnetics, IEEE Transactions on,* vol. 46, pp. 2328-2330, 2010.

[25] X. Waintal, E. B. Myers, P. W. Brouwer, and D. Ralph, "Role of spin-dependent interface scattering in generating current-induced torques in magnetic multilayers," *Physical Review B,* vol. 62, p. 12317, 2000.

[26] S. Mangin, D. Ravelosona, J. Katine, M. Carey, B. Terris, and E. E. Fullerton, "Current-induced magnetization reversal in nanopillars with perpendicular anisotropy," *Nature Materials,* vol. 5, pp. 210-215, 2006.

[27] D. Pinna, D. L. Stein, and A. D. Kent, "Spin-torque oscillators with thermal noise: A constant energy orbit approach," *Physical Review B,* vol. 90, p. 174405, 2014.

[28] D. Bedau, H. Liu, J. Sun, J. Katine, E. Fullerton, S. Mangin, and A. Kent, "Spin-transfer pulse switching: From the dynamic to the thermally activated regime," *Applied Physics Letters,* vol. 97, p. 262502, 2010.

[29] J. Xiao, A. Zangwill, and M. Stiles, "Macrospin models of spin transfer dynamics," *Physical Review B,* vol. 72, p. 014446, 2005.

[30] J. Sun, "Spin-current interaction with a monodomain magnetic body: A model study," *Physical Review B,* vol. 62, p. 570, 2000.

[31] D. Bedau, H. Liu, J.-J. Bouzaglou, A. Kent, J. Sun, J. Katine, E. E. Fullerton, and S. Mangin, "Ultrafast spin-transfer switching in spin valve nanopillars with perpendicular anisotropy," *Applied Physics Letters,* vol. 96, p. 022514, 2010.

[32] R. Chang, S. Li, M. Lubarda, B. Livshitz, and V. Lomakin, "FastMag: Fast micromagnetic simulator for complex magnetic structures," *Journal of Applied Physics,* vol. 109, p. 07D358, 2011.

[33] D. Ravelosona, S. Mangin, Y. Lemaho, J. Katine, B. Terris, and E. E. Fullerton, "Domain wall creation in nanostructures driven by a spin-polarized current," *Physical review letters,* vol. 96, p. 186604, 2006.

[34] J. Cucchiara, Y. Henry, D. Ravelosona, D. Lacour, E. Fullerton, J. Katine, and S. Mangin, "Telegraph noise due to domain wall motion driven by spin current in perpendicular magnetized nanopillars," *Applied Physics Letters,* vol. 94, p. 102503, 2009.

[35] D. P. Bernstein, B. Bräuer, R. Kukreja, J. Stöhr, T. Hauet, J. Cucchiara, S. Mangin, J. A. Katine, T. Tyliszczak, and K. W. Chou, "Nonuniform switching of the perpendicular magnetization in a spin-torque-driven magnetic nanopillar," *Physical Review B,* vol. 83, p. 180410, 2011.

[36] M. Bhushan, A. Gattiker, M. B. Ketchen, and K. K. Das, "Ring oscillators for CMOS process tuning and variability control," *Ieee Transactions on Semiconductor Manufacturing,* vol. 19, pp. 10-18, Feb 2006.

[37] B. Razavi, *Design of integrated circuits for optical communications*: John Wiley & Sons, 2012.

[38] W. Kang, Y. Zhang, Z. Wang, J.-O. Klein, C. Chappert, D. Ravelosona, G. Wang, Y. Zhang, and W. Zhao, "Spintronics: Emerging Ultra-Low-Power Circuits and Systems beyond MOS Technology," *ACM Journal on Emerging Technologies in Computing Systems (JETC),* vol. 12, p. 16, 2015.

[39] A. Hajimiri, S. Limotyrakis, and T. H. Lee, "Jitter and phase noise in ring oscillators," *Ieee Journal of Solid-State Circuits,* vol. 34, pp. 790-804, Jun 1999.

[40] M. Hsieh and G. E. Sobelman, "Comparison of LC and Ring VCOs for PLLs in a 90 nm Digital CMOS Process," in *Proceedings, international SoC design conference*, 2006, pp. 19-22.

[41] A. D. Evans, *Designing with field-effect transistors*: McGraw-Hill Companies, 1981.

[42] J. L. Leal and M. H. Kryder, "Spin valves exchange biased by Co/Ru/Co synthetic antiferromagnets," *Journal of Applied Physics,* vol. 83, pp. 3720-3723, Apr 1 1998.

[43] Y.-H. Chuang, S.-L. Jang, J.-F. Lee, and S.-H. Lee, "A low voltage 900 MHz voltage controlled ring oscillator with wide tuning range," in *Circuits and Systems, 2004. Proceedings. The 2004 IEEE Asia-Pacific Conference on*, 2004, pp. 301-304.

[44] J. G. Maneatis, J. Kim, L. McClatchie, J. Maxey, and M. Shankaradas, "Self-biased high-bandwidth low-jitter 1-to-4096 multiplier clock generator PLL," *Ieee Journal of Solid-State Circuits,* vol. 38, pp. 1795-1803, Nov 2003.

[45] P. Raha, "A 0.6-4.2 V low-power configurable PLL architecture for 6 GHz-300 MHz applications in a 90 nm CMOS process," in *VLSI Circuits, 2004. Digest of Technical Papers. 2004 Symposium on*, 2004, pp. 232-235.

[46] V. Sikarwar, N. Yadav, and S. Akashe, "Design and analysis of CMOS ring oscillator using 45 nm technology," *Proceedings of the 2013 3rd Ieee International Advance Computing Conference (Iacc),* pp. 1491-1495, 2013.

[47] J. J. Kim and B. Kim, "A low-phase-noise CMOS LC oscillator with a ring structure," in *Solid-State Circuits Conference, 2000. Digest of Technical Papers. ISSCC. 2000 IEEE International*, 2000, pp. 430-431.

[48] M. Durlam, P. Naji, A. Omair, M. DeHerrera, J. Calder, J. Slaughter, B. Engel, N. Rizzo, G. Grynkewich, and B. Butcher, "A low power 1 Mbit MRAM based on 1T1MTJ bit cell integrated with copper interconnects," in *VLSI Circuits Digest of Technical Papers, 2002. Symposium on*, 2002, pp. 158-161.

[49] A. L. Geiler, J. Wang, J. S. Gao, S. D. Yoon, Y. Chen, V. G. Harris, and C. Vittoria, "Low Bias Field Hexagonal Y-Type Ferrite Phase Shifters at-Band," *Magnetics, IEEE Transactions on,* vol. 45, pp. 4179-4182, 2009.

[50] S. Tehrani, B. Engel, J. M. Slaughter, E. Chen, M. DeHerrera, M. Durlam, P. Naji, R. Whig, J. Janesky, and J. Calder, "Recent developments in Magnetic Tunnel Junction MRAM," *Ieee Transactions on Magnetics,* vol. 36, pp. 2752-2757, Sep 2000.

[51] J. Katine, F. Albert, R. Buhrman, E. Myers, and D. Ralph, "Current-driven magnetization reversal and spin-wave excitations in Co/Cu/Co pillars," *Physical Review Letters,* vol. 84, p. 3149, 2000.

[52] S. I. Kiselev, J. Sankey, I. Krivorotov, N. Emley, R. Schoelkopf, R. Buhrman, and D. Ralph, "Microwave oscillations of a nanomagnet driven by a spin-polarized current," *Nature,* vol. 425, pp. 380-383, 2003.

[53] Y. Suzuki and H. Kubota, "Spin-torque diode effect and its application," *Journal of the Physical Society of Japan,* vol. 77, p. 031002, 2008.

[54] J. Z. Sun, "Spin angular momentum transfer in current-perpendicular nanomagnetic junctions," *IBM journal of research and development,* vol. 50, pp. 81-100, 2006.

[55] A. Slavin and V. Tiberkevich, "Nonlinear auto-oscillator theory of microwave generation by spin-polarized current," *IEEE Transactions on Magnetics,* vol. 45, pp. 1875-1918, 2009.

[56] J.-V. Kim, V. Tiberkevich, and A. N. Slavin, "Generation linewidth of an auto-oscillator with a nonlinear frequency shift: Spin-torque nano-oscillator," *Physical review letters,* vol. 100, p. 017207, 2008.

[57] P. Muduli, O. Heinonen, and J. Åkerman, "Decoherence and mode hopping in a magnetic tunnel junction based spin torque oscillator," *Physical review letters,* vol. 108, p. 207203, 2012.

[58] E. Iacocca, O. Heinonen, P. Muduli, and J. Åkerman, "Generation linewidth of mode-hopping spin torque oscillators," *Physical Review B,* vol. 89, p. 054402, 2014.

[59] J. Griffiths, "Anomalous high-frequency resistance of ferromagnetic metals," *Nature,* vol. 158, p. 670, 1946.

[60] C. Kittel, "On the theory of ferromagnetic resonance absorption," *Physical Review,* vol. 73, p. 155, 1948.

[61] C. Kittel, "On the gyromagnetic ratio and spectroscopic splitting factor of ferromagnetic substances," *Physical Review,* vol. 76, p. 743, 1949.

[62] B. Heinrich and J. Cochran, "Ultrathin metallic magnetic films: magnetic anisotropies and exchange interactions," *Advances in Physics,* vol. 42, pp. 523-639, 1993.

[63] V. Kamberský, "On ferromagnetic resonance damping in metals," *Czechoslovak Journal of Physics B,* vol. 26, pp. 1366-1383, 1976.

[64] C. Neo, Y. Yang, and J. Ding, "Calculation of complex permeability of magnetic composite materials using ferromagnetic resonance model," *Journal of Applied Physics,* vol. 107, p. 083906, 2010.

[65] C. Bilzer, T. Devolder, P. Crozat, C. Chappert, S. Cardoso, and P. Freitas, "Vector network analyzer ferromagnetic resonance of thin films on coplanar waveguides: Comparison of different evaluation methods," *Journal of applied physics,* vol. 101, p. 074505, 2007.

[66] A. A. Kovalev, G. E. Bauer, and A. Brataas, "Current-driven ferromagnetic resonance, mechanical torques, and rotary motion in magnetic nanostructures," *Physical Review B,* vol. 75, p. 014430, 2007.